AUTOMATIC MICROASSEMBLY OF TISSUE ENGINEERING SCAFFOLD

ZHAO GUOYONG
(B. Eng)

A THESIS SUBMITTED
FOR THE DEGREE OF DOCTOR OF PHILOSOPHY

DEPARTMENT OF MECHANICAL ENGINEERING
NATIONAL UNIVERSITY OF SINGAPORE
2010

Acknowledgments

First and foremost, I want to express my most sincere gratitude to my supervisors, Dr. TEO Chee Leong, Dr. Etienne BURDET, and Dr. Dietmar W. HUTMACHER for their valuable supervision, constructive guidance, incisive insight and enthusiastic encouragement throughout my project.

I wish to specifically thank Dr. Franck Alexis CHOLLET and his group in the Micro Machine Centre (MMC) at Nayang Technology University (NTU) for his kind guidance on the design and fabrication of the micro parts. I wish to thank Mr. MOHAMMED Ashraf for his help in the cleanroom work and his friendship.

My gratitude is also extended to the colleagues and friends in our lab and NUS, Mr. ZHU Kunpeng, Mr. Du Tiehua, Mr. WANG Chen, Mr. WAN Jie, Mr. LU Zhe, Mr. ZHOU Longjiang, Ms. SUI Dan and many others, for their enlightening discussion, suggestions and friendship.

Finally, I owe my deepest thanks to my parents, my family, and my wife, Yubi, for their unconditional and selfless encouragement, love and support.

Table of contents

Summary

In this work, an assembly workstation system for automatically fabricating customized tissue engineering (TE) scaffold was developed. This included the design and fabrication of microparts and a novel microgripper with integrated force sensor, building a desktop workstation, implementation of closed-loop force control and visual servoing, and the development and implementation of an intelligent control strategy.

The microparts (of dimension $0.5 \times 0.5 \times 0.2mm$ and $60\mu m$ wall thickness) were fabricated by using photolithography techniques. The mating dimensions of the microparts were carefully controlled to achieve desired friction between microgripper and microparts and between microparts. Factors that affect the qualities of the microparts were also investigated.

A microgripper was specially designed and fabricated to interface with the microparts. The main body of the microgripper was a tungsten rod of $200\mu m$ in diameter. At one end of the tungsten rod, a cylinder tip with a diameter of $100\mu m$ was fabricated by electrolyte etching. The accuracy of the diameter was less than $3\mu m$ thanks to the specially designed circuits for controlling the etching charges. The tip was mounted with a girdle to provide pushing force during picking up and assembly processes.

The integrated force sensor was designed, fabricated and calibrated to measure the force involved in the assembly. Its main body was an elastic element that will deform under load. Semiconductor strain gauges were glued to the top and bottom surface of the elastic element. The full range of the force sensor was about 500mN with a resolution of 3mN.

Closed-loop force control was implemented in the pick-up and assembly process. An admittance control scheme and an intelligent strategy enabled smooth insertion and prevented the micropart from damages. The control strategy combined position and force information to infer the status of the insertion process and re-aligned if necessary. Visual servoing was used in a look-and-move fashion. A modified Hough transform was used as the basis in the image processing algorithms.

The automatic assembly workstation composed of four translation precision stages was built for the assembly task. Three sets of microscopes with CCD cameras were used to provide front, side and top views of the working area.

A visual C++ program coordinated all the hardware and provided a friendly GUI for the operator to perform the calibration process easily. After calibration, automatic assembly can be started by activating the “Auto Assembly” button on the GUI. The automated assembly task was conducted under the control of the supervisory unit of the software.

The system has successfully demonstrated fully automated construction of a tissue engineering scaffold composing of 50 microparts whose dimensional error can be as large as 9%.

Publications

Journal papers:

Guoyong Zhao, Chee Leong Teo, Dietmar Werner Hutmacher and Etienne Burdet "Force controlled, automatic microassembly of tissue engineering scaffolds" *Journal of Micromechanics and Microengineering* , v 20, n 3, p 035001 (11 pp.), March 2010

Lu, Zhe; Chen, Peter C.Y.; Ganapathy, Anand; ***Zhao, Guoyong***; Nam, Joohoo; Yang, Guilin; Burdet, Etienne; Teo, Cheeleong; Meng, Qingnian; Lin, Wei "A force-feedback control system for micro-assembly" *Journal of Micromechanics and Microengineering*, v 16, n 9, Sep 1, 2006, p 1861-1868

Conference:

Guoyong Zhao, Chee Leong Teo, Dietmar Werner Hutmacher and Etienne Burdet "Automated microassembly of tissue engineering scaffold" *IEEE International Conference on Robotics and Automation, (ICRA 2010)*, p 1082-3, 2010 (video)

List of Tables

List of Figures

Chapter 1

Introduction

1.1 Background

Tissue engineering (TE), as stated by Langer and Vacanti, is "an interdisciplinary field that applies the principles of engineering and life sciences toward the development of biological substitutes that restore, maintain, or improve tissue function or a whole organ" [1]. This new field has drawn a lot of attentions since its advent in the 1980s.

Most tissue engineering strategies for creating functional replacement tissues of organs rely on the application of an engineered extracellular matrix or scaffold, to guide the proliferation and spread of the seeded cells. A TE scaffold usually should serve the following purposes: 1. Allow cell attachment and migration; 2. Deliver and retain cells and biochemical factors; 3. Enable diffusion of vital cell nutrients and expressed products; 4. Exert certain mechanical and biological influences to modify the behavior of the cell phase [2].

To achieve the goal of tissue reconstruction, scaffolds must meet some specific requirements: (1) a high porosity and pore interconnectivity are necessary to

facilitate cell seeding and diffusion throughout the whole structure of both cells and nutrients [3, 4]. Also the pore size must be specifically designed for the certain purpose and the size usually varies from ten to hundred of microns [5-7]. (2) The material used for TE scaffold has to be biodegradable since the scaffold should be absorbed by the surrounding tissues i.e. should not require surgical removal after neotissues formed [8]. (3) The scaffold should have some desired mechanical properties, for example, it should be strong enough to support the cells, and guide the tissue regeneration, especially during the degrading period of the scaffold [4].

Methods for the fabrication of tissue engineering scaffolds include nanofiber self-assembly, textile technologies, solvent casting and particulate leaching (SCPL), gas foaming, emulsification (also may referred to as freeze-drying), thermally induced phase separation (TIPS) etc. Each of these techniques has its own advantages, but none fulfills all the above requirements [2].

In her Ph.D thesis, Zhang [133] developed a system for fabrication of TE scaffold by robotic assembly of microscopic parts. A salient feature of this fabrication method is that it enabled the spatial control of the cell, agents and pore size, etc which was highly desirable to cater for different structures and patients. She demonstrated manual assembly of such a scaffold by using a master-slave robotic system [9], but the long serial fabrication time required meant that automating the assembly process is necessary in order to narrow the gap between laboratory experiments and clinical applications.

1.2 Problem Definition

In the manual assembly process, the operator manipulated a robotic workstation in a tele-operation fashion. The assembly process was observed through two microscopes. To assemble each micropart onto the scaffold, the operator needed to first move the gripper to the part, picked up the part, moved the gripper to the assembly area, find the position to put the part and then assembled it. The two major disadvantages of this method are:

1. Operator dependant. A skillful operator was needed to operate the system. The micropart, made of polymer with the dimension of hundreds of microns, was very fragile and this will induce stress and fatigue to the operator.
2. Low throughput. Assembling a micropart took about 1 minute. Normally a small piece of scaffold consisting of tens of microparts will take a day or more. For clinical applications, a scaffold may need hundreds or thousands of parts.

1.3 Objectives

The whole assembly process needs to be automated in order to increase the assembly speed and reduce the necessity of human intervention. A literature review on microassembly shows that there are two major difficulties in microassembly tasks: the high positional accuracy needed and the lack of force control. To circumvent these difficulties, I propose an automated microassembly system using both closed-loop position control and closed-loop force control. The objectives of this thesis are:

1. To systematically review and analyze the existing techniques in micromanipulation and microassembly tasks.
2. To design a microgripper for handling microparts.
3. To investigate the force sensing methods and control issues in microassembly and to develop a suitable force sensor and force control strategy.
4. To implement closed-loop position control based on visual information.
5. To design and develop a workstation to realize the automated assembly process.
6. To implement and evaluate the performance of the automatic microassembly system.

1.4 Scope

TE scaffold assembled by microscopic building blocks is highly desirable for tissue regeneration because it could produce various structures, control the nutrients inside the scaffold exactly as required to optimize regeneration, and cater to different patients with different designs of the scaffold. Each micro building block can be coated and processed to have specific morphology and chemical properties, and then assembled to the required place in the scaffold in a biocompatible environment. The whole process does not involve any chemical, electrical or thermal reaction. While the feasibility of such TE scaffolds has been demonstrated through manual assembly, the whole process is extremely time-consuming and tedious, which hindered clinical applications. Automating the assembly is the best way to solve this problem. This thesis presents an automatic

microassembly system dedicated to fabrication of customized TE scaffolds. Among the work that has been accomplished are the following:

1. A literature review was first carried out to study the state-of-the-art techniques in microassembly, which indicated that vision and force feedback are the most effective ways to realize automatic assembly in the micro domain. The configuration of the whole automated microassembly system was developed which includes both closed-loop position control based on vision feedback and closed-loop force control (Figure 1.1).

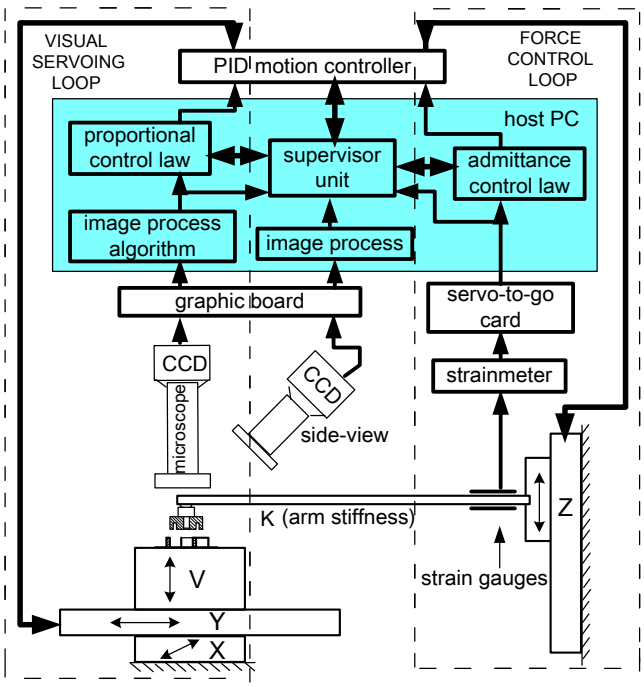

Figure 1.1: Schematic of automated microassembly system with visual servoing and force control loops.

2. A microgripper dedicated to handling microparts was designed and fabricated. To enable the use of the top-view microscope for closed-loop position control, the gripper must have a very compact size so as to not occlude the microscope top-view. In order to implement closed-loop force

control during insertion, the gripper should also integrate a suitable force sensor and distribute the force evenly on the micropart (Figure 1.2).

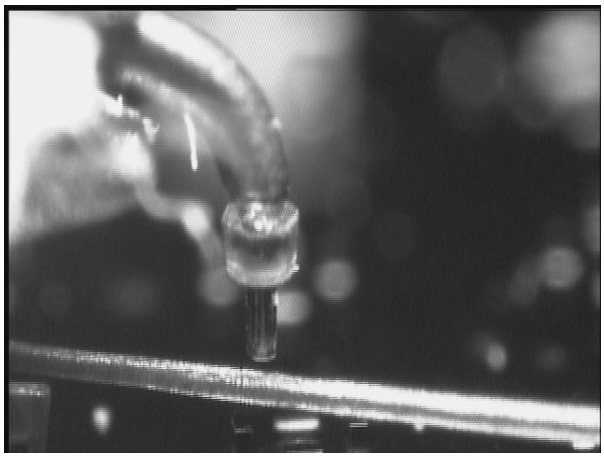

Figure 1.2: Micro gripper compared with a human hair.

3. A force sensor was designed, fabricated and calibrated. The measuring range of the force sensor is 0-500*mN* with a resolution of 3*mN*, which is suitable for the targeted microassembly (Figure 1.3).

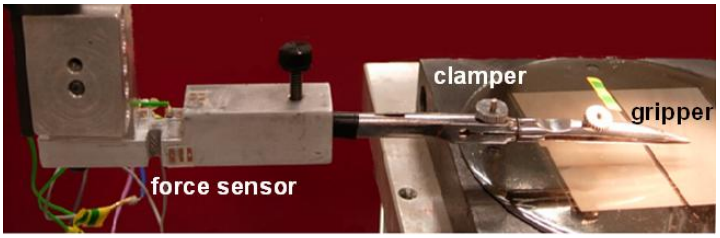

Figure 1.3: Force sensor with gripper.

4. Admittance force control law was implemented to control the pick-up and assembly of the microparts. The working principle of the force control system is illustrated in Figure 1.1. A gripper fixed on the arm was carried by the *Z* stage to move up and down to realize insertion and retraction. Based on the force reading from the strain gauges, position and velocity

commands are sent to the *Z* stage. It is through adjusting the motion of the *Z* stage that force control is realized.

5. Vision-based position control was implemented. Different image processing algorithms were studied, and selected algorithms were used in the control loops. In the visual servoing loop, only the top-view microscope was used. Error was computed from image processing and then corrected through proportional control using the *XY* stage.
6. A workstation consisting of four precision stages and three microscope systems was built and implemented (Figure 1.4). A friendly graphic user interface was also developed for the operator to help him to calibrate the system.

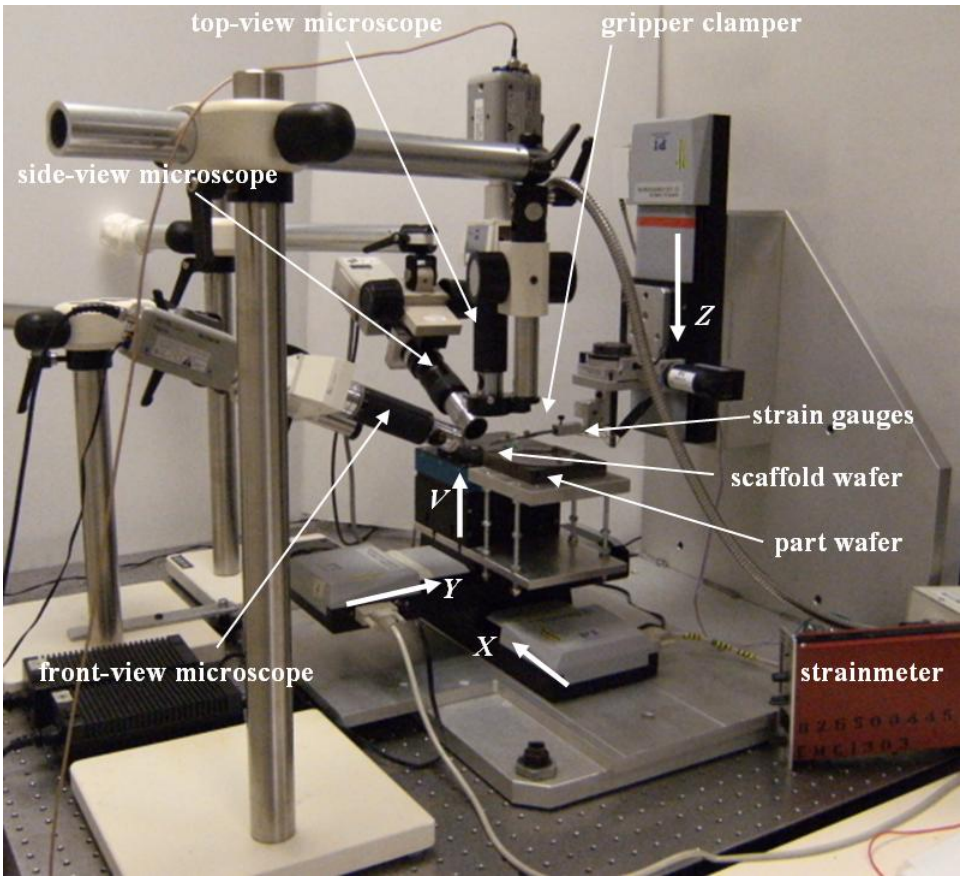

Figure 1.4: Precision workstation.

7. An automated assembled process was carried out to evaluate the performance of the system. Small scaffolds with 50 microparts and seven layers (Figure 1.5) were successfully fabricated.

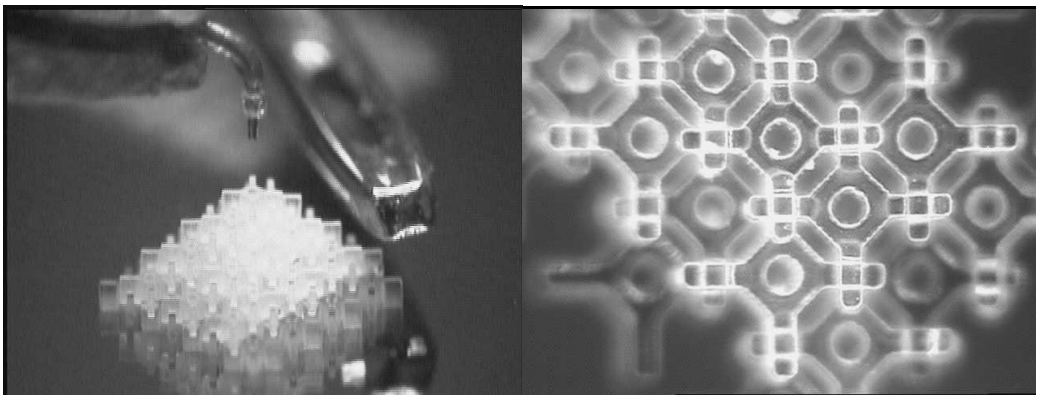

A B

Figure 1.5: (A) a small piece of automatically assembled scaffold with the gripper above compared with a regular needle. (B) top view of the scaffold

1.5 Thesis Organization

This thesis is organized as follows. Chapter 2 provides a literature review of current microassembly systems. The fabrication of microscopic building blocks used in the assembly process is described in Chapter 3. Chapter 4 investigates the design and fabrication of the microgripper. Chapter 5 describes the design and fabrication of the force sensor and its calibration. In this chapter, the admittance force control law and the implementation of closed-loop force control in the pick-up and assembly process are also presented. Chapter 6 describes the visual servoing for closed-loop position control, including the control strategies, control law, hardware and the image processing algorithms used. Chapter 7 focuses on the design, calibration and control of the specially designed workstation and the program used to coordinate all the hardware components. The results of the

microassembly experiments are also presented in this chapter. Finally, Chapter 8 proposes research directions to further develop the technique developed in this thesis.

Chapter 2

Literature Review on Microassembly

2.1 Introduction

Although my project concerns the life sciences, the essential techniques involved are similar to those used in micro electro mechanical systems (MEMS) in terms of feature dimension, accuracy, scaling effects etc., and the results of this thesis can be applied to general microassembly in fields including MEMSs.

Microassembly, the assembly of objects with microscale and/or mesoscale features under microscale tolerances, has been widely and extensively studied in the last two decades, due in particular to the increasing demand for more complex MEMSs. While considerable advances have been made in the fabrication of microparts, the assembly and packaging of heterogeneous microsystems still accounts for a very substantial fraction of the cost of commercial products: about 60% to 90% of manufacturing costs [10].

Microassembly tasks can be classified into two major groups: parallel microassembly and serial microassembly [11].

In *parallel microassembly*, multiple parts are assembled simultaneously to reduce the assembling time and the cost of the final product. Parallel microassembly tasks can be further divided into deterministic parallel assembly and stochastic parallel assembly.

- Deterministic parallel assembly normally requires complex grasping, conveying, aligning and assembly strategy. For instance, [12] proposes using a microgripper array to pick up and assemble an array of microparts simultaneously. Similarly, [13] develops a technique that deposits many Si chips in size of hundred microns on an organic substrate at the same time to produce large liquid crystal display. To avoid using complex grasping mechanics, [14] manufactures micro gear system in a large bath by ejecting the micro gears from the magazine onto the defined mounting position of the micro devices directly after precise alignment. The capacity of this method has been demonstrated experimentally.
- In stochastic parallel assembly, structures are aggregated through fluidic agitation, vibration, electrostatic force field or part shape mating [15]. For instance, [16] uses shape mating to produce photonic crystals assembled by silica micro-spheres on a large scale.

Although parallel assembly techniques can deal with a large number of microparts and efficiently form larger structures, it cannot be used to fabricate complex structures such as the TE scaffold proposed in this project. In contrast, serial assembly is more capable in producing complex micro 3D structures.

In *serial microassembly*, parts are put together one-by-one according to a traditional pick-and-place paradigm. Not long ago, almost all the serial micro-assembly tasks were conducted in a tele-operation fashion: an operator controls a precision workstation or a microrobot through a machine-human interface or joystick and images of the working process were provided to the operator by microscopes. Recently, automatic or semi-automatic microassembly experiments have been developed by several research groups [23, 87, 102-110, 159]. We will focus on serial microassembly and related issues in the following paragraphs.

Besides these two mainstream microassembly technique discussed above, there are some other microassembly techniques used for particular applications. Simple planar structures were assembled by manipulating stress-engineered MEMS microdots [17]. The size of the robots is in the range of hundreds of microns, which is unique in the MEMS Industry. Out-of-plane microstructures can be fabricated by deformation of the micro component itself which is referred to as self-assembly. [18] proposes a simple self-assembly strategy to fabricate three-dimensional micro structures involving the thermal shrinkage of polyimide; [19] develops a self-assembly method by using magnetic forces. In [19] certain part of the microstructure deposited with magnetic material will be plastically deformed by the magnetic force exerted by an external magnetic field.

2.2 Differences between Micro and Macro Assembly

A major difference between assembly in the micro- and macro domains is the interaction forces involved. In the macroworld, the mechanics of manipulation are

predictable, e.g. when a gripper opens, gravity causes the part to drop. In the microworld, forces other than gravity dominate due to scaling effects. Surface-related forces, such as electrostatic, van der Waals and surface tension forces become dominant over gravitational forces. Mass decreases with L^3 while stiffness for bending and tensile strength are proportional to L and L^2, respectively. Due to this uneven scaling behavior, manipulation in the microworld is completely different from manipulation in the macro world [20, 21] .

Another major difference between macro- and micro-assembly is the required positional accuracy. In the macro domain, accuracy in the range of a few hundred microns can be achieved using sensorless manipulators. In the micro domain, submicron precision is often required [22]. Also precision of micro assembly systems is often deteriorated by many factors, such as tolerance stack up due to thermal effects, errors and approximations in the modeling of sensors and manipulators, internal and external vibrations, and parts machining errors [23]. Conventional open-loop precision assembly devices used in industry can not achieve this degree of precision and microassembly must rely on vision information to implement high-precision motion control.

2.3 Design of Microassembly Systems

Due to all the above factors, complex microstructures cannot be assembled in the traditional way. The major design factors involved in building a microassembly system include the following aspects:

1. Design of microgripper

2. Design of precision positioning unit
3. Implementation of vision system

Beside these aspects, closed-loop position control or force control may also be necessary for automated microassembly system. To implement closed-loop position control, the system design may include image processing algorithms, controller design and the use of closed-loop force control, the design or selection of an appropriate force sensor, the development of the control loop and appropriate control law.

2.3.1 Design of Microgripper

The role of a microgripper is to provide enough constraints to the micro component being assembled. Because of the micro-level forces involved and the small size of the components, the design and fabrication of microgripper is always a challenge. Reliability and efficiency of the microgripper is critical to the performance of the entire assembly system. Because the objects being manipulated are very small, the microgripper normally has to have a very compact dimension or at least small handling tips. The small size of the gripper is also desirable for the implementation within the crowded setup with microscopes etc. In design of a microgripper, the releasing strategies are as important as the picking up strategies as the release of the parts is often problematic due to the presence of adhesion forces [24].

Many microgrippers based on different working principles have been developed for a variety of microassembly tasks. [25] proposes a classification scheme for quantified analysis of a list of gripping principles. This scheme also defines criteria

that are essential in the evaluation and selection of gripping principles for grasping a given micro object.

Lead zirconate titanate (PZT) ceramics is one of the most commonly used materials for actuating microgrippers due to its superior piezoelectric properties [26-31]. A salient feature of piezoelectric actuators is that they allow precise control of the motion of the gripper fingers. Because of this, closed-loop control of grasping force can be easily realized on PZT actuated grippers by the integration of micro force sensors [32-36].

Electrostatic comb-drive actuators have a more compact size and shorter response time than piezoelectric actuators, and have been widely used in MEMSs [37, 38]. Microgrippers actuated by electrostatic comb were fabricated for handling small objects such as single cell living creatures [39, 40].

Another commonly used actuating technique in the use of shape memory alloy (SMA) [41-45]. SMA has a work output per volume larger than that of electrostatic and piezoelectric actuators and its cycling frequencies can achieve the order of $100Hz$ [46].

The operating of thermal bimorphs is based on differential thermal expansion induced by Joule heating [47], which is capable of producing large motion by thermal expansion [48]. Thermally driven microgrippers can operate in the atmosphere, vacuum or dust environments [49].

Design and fabrication of vacuum grippers is much simpler compared with other microgrippers. The main body of a vacuum gripper is just a pipette connected to a

vacuum supply [50-53]. This kind of gripper is more likely to be used for micromanipulation than microassembly due to the limited constraints provided by the gripper.

Passive structure compliance of a microgripper is important for protection of fragile components and accommodation of alignment errors [54]. A generalized methodology for designing compliant micro mechanisms was given by [55]. [56] and [57] present a compliant gripper actuated by thermal bimorph actuator and piezoelectric ceramic stacks respectively. A complaint passive gripper was developed by [58]. Passive grippers employ no actuator and the microparts are picked up by friction or compliance of the gripper tips. In this case, the microparts being handled were also specially designed to interface with the gripper.

Besides all the techniques discussed above, there are some other actuating techniques used in micro gripper design, such as pneumatically-actuated microgripper [59], voice coil motor actuated gripper [60], magnetic actuated gripper [61], orthotweezers power by servo motor [62], ice gripper [63] etc.

2.3.2 Precision Positioning Unit

In serial microassembly tasks, micro components need to be picked up, conveyed to the assembly area, aligned and then assembled. The conveying and alignment were accomplished through a precision position unit. Normally a microassembly task demands a positioning unit with 4 to 6 degrees of freedom. Translation precision stages actuated by DC motors normally have submicron resolution, which is sufficient for most microassembly tasks. Piezoelectrically actuated

precision stages can provide a motion resolution in range of nanometer, but the travel range is comparatively small [24]. In the past, most of the precision workstations were built based on off-the shelf precision stages [64-68, 106]. One example of them is [106] which presents a 6-DoF workstation to assemble out-of-plane micro-structures and permits assembly of microparts on the surface of the MEMS chip at an arbitrary spatial angle.

For master-slave systems, another factor that influences the positioning accuracy is the master system. Addressing this issue, [69] and [70] investigate the joystick sensitivity and time delay issue involved in tele-operated microassembly tasks.

Besides these precision stages-based microassembly systems, micro robots can also be used to perform complex microassembly tasks. [71] develops a novel 3-DoF parallel robot for microassembly whose accuracy is about $1\mu m$ and workspace volume is a cube of $30mm$ side. MINIMAN® is a series of microrobots which have at least 5 DoF and dimension of some cm^3. MINIMAN® are piezoelectrically actuated to achieve a resolution in the range of nanometers and also capable of traveling a relatively long distance. Many microassembly workstations have been built based on MINIMAN® families, such as [72-77].

2.3.3 Vision System

Visual feedback is crucial for microassembly process, as it can provide a noncontact sensing modality for fine alignment, observation and task planning. However, the inclusion of microscopes in microassembly systems also faces many challenges, which we will examine now.

The first challenge is the very limited depth of field of microscopes. The need for high resolution demands the use of high numerical aperture lens systems, which consequently have a very small depth of field, typically ranging from $120\mu m$ to $0.2\mu m$. As a result depth perception is quite difficult. 3D microassembly may require two or more microscopes in a stereo configuration, but due to the limited workspace, addition of more microscopes is often problematic. To address this issue, [78] increases the depth of field of the microscope over 60 times by the use of a volume rendering technique which greatly assists the operator in microassembly process; [79] replaced the lateral view microscope with a virtual one that is synthesized from two top-view microscopes.

A second challenge is the very small field of view also caused by the use of high magnification microscopes. Although the parts being assembled are small, they generally need to be transported relatively large distances prior to assembly. To help the operator see the gross spatial relations, a global view can be used to monitor the status of the entire assembly scene [87]. For multi-view systems [68, 80], due to the large different magnifications of different cameras, illumination must be controlled separately; the limited working distance of the microscope may cause a limited working space and thus occlusions to the global view. Hence, the design of the visual system must be coupled with the design of precision unit and microgripper. [81] systematically analyzes the implementation of microscopes optics in microassembly system and also gives a general architecture of microassembly systems.

2.4 Microassembly Systems

In this section, a review of the development of microassembly systems is presented. In the earlier days, most of the microassembly tasks were performed manually in a tele-operated fashion through master-slave systems. Manual microassembly needs a human operator to perform all the actions and the whole process is tedious, stressful and time-consuming. To reduce the intervention of humans in the assembly loop and increase the throughput, efforts have increasingly been made towards automated microassembly in recent years. These efforts involve the use of virtual reality (VR) to facilitate the assembly process, and/or the use of vision and force feedback to automatically perform part of the assembly steps, etc.

2.4.1 Manual Microassembly

In manual microassembly, a highly skilled operator is needed to pick and place microparts by using a master-slave system. The master-slave system makes the target's scale to be similar to our scale virtually, and the human operator manipulates the slave systems through the master manipulators [82]. The slave system which interfaces with the micro component, can be a desktop workstation composed of precision stages [58, 53, 87, 83, 84], or a micro robot with micro handling tools [73, 85, 86, 50]. Because of the superior flexibility and discrimination capability of humans, this kind of master-slave technique is widely used in the biomedical field, prototype fabrication or small batch microdevices production.

Examples of manually microassembly are as follows: [53] and [87] present a supervisory microassembly work cell developed for assembling micro machined metal parts into etched holes on silicon wafers. In these papers, the major components of the microassembly system (the micromanipulator, the illumination devices, and the gripper) were presented. Later, visual servoing was also implemented in this system [88]. [89] developed a 5 degree-of-freedom workstation for assembly of biomedical devices which can also be modified and applied to assembly photonics, miniature wireless system, micro actuators, etc.

In the systems mentioned above, the only sensory modules the operator can depend on are microscopes. The operator needs to look at the microscope screens all the time in order to determine contact, collision or other events. To handle micro objects under such conditions continuously will introduce stress and fatigue, especially when the object is fragile such as living cells or photonics. To further improve the performance of the microassembly system, haptic devices were employed in master-slave microassembly systems. In these cases, a force sensor was mounted on the gripper or the manipulator, force signals were transferred to the haptic devices to provide the operator with extra information about contact or collisions [90-92]. This technique is also helpful for protecting the micro component from damages with improperly applied forces.

2.4.2 Virtual Reality Aided Microassembly

In a tele-operated microassembly process, the user interface should provide sufficient information of the working area for the operator to perform the assembly task. However, hiding or abstracting unnecessary information could facilitate the

assembly process. This additional layer of abstraction between the operator and the real work area was realized through virtual reality (VR) approaches [93]. VR technique had been explored at varying levels of applications by many research groups to facilitate microassembly [94]. In these applications, machine vision was used for identification of the objects in a scene and VR based frameworks enabled the user to propose and visualize assembly solution prior to physical assembly.

[95, 96] presented a workstation that used both visual servoing and virtual reality techniques. Visual servoing was applied for efficient and reliable position and force feedback and the virtual microworld, reconstructed from the CAD-CAM database of the real environment, provided the operator a friendly manipulating system. In a similar way, [97-99] developed a workstation interface with a virtual environment to support assembly of micron-size components; a genetic algorithm-based assembly sequence generator that coordinated with a 3D path planning approach was also discussed.

2.4.3 Visual Servoing Aided Microassembly

VR techniques provided the operator with more desirable information, but the manipulation still had to be performed by the operator. To further reduce the human intervention in the assembly process, visual servoing and force control were used to automate part of the assembly steps. Visual servoing would normally be used for closed-loop position control. By visual servoing, automated alignment was realized. And closed-loop force control was often added for automated grasping [100] or insertion [101] steps.

[102-110] presented an automated microassembly workstation employing visual servoing in alignment steps of picking up and assembling a micropart (20μm wide and 2μm thick) into the slot on the substrate. In this project, vision information was also used to measure the grasping force by measuring the deformation of the passive gripper fingers. A fuzzy logic controller was developed to fuse the force and position information to achieve successful automated grasping and insertion. The depth-from-focus technique used for position estimation along the optical axis of the microscope was similar to that used in [23].

Automated alignment through visual servoing was also widely used in photonics assembly. [111] developed a closed-loop scheme for aligning the optical fiber with the V-groove chip. The scheme used a look-and-move mode and each fiber was able to be aligned within 1 minute. In [112], the alignment of the optical fiber with the ferrules was accomplished by visual servoing of two orthogonally placed microscopes (providing top and side views); the insertions were performed manually by the help of force feedback. In a similar way, [52] also used visual servoing for fine alignment and force control for handling micro component in microassembly process.

[87] built a flexible 4D workstation for assembly of metal microparts with a size of half a millimeter. To automate the alignment process, a CAD model-based visual tracking system was developed [113, 88]. The visual system involved two microscopes and was capable of 6-DoF tracking MEMS component in real-time (30Hz). For the same application, [114] developed another workcell, which utilized a transparent electrostatic gripper for handling metal parts. Computer vision was

used for aligning the gripper with the part, and a fiber-couple laser and position detector were used for aligning the part with the slot on the wafer before assembly, while the insertion step was still performed manually.

More recently, various visual serving methods were developed and applied in microassembly tasks. [115] describes both 2D and 3D image processing methods for application in micro production environments. In this article, 2D image processing was used for controlling of assembly micro mixer and 3D data were acquired by the combination of fringe projection methods with fiber-optic device, which produced a highly flexible system for automated assembly of hybrid micro devices.

Neural networks were applied in a peg-into-hole microassembly task [116, 117]. In these articles, 3D position of an object was obtained by using only one camera. Position was estimated by images of the single camera under different light sources (four light sources from four directions). In another peg-into-hole application, a Kalman filtering-based algorithm was developed and used in the visual servoing loop to estimate the composite image Jacobian on-line so as to reduce the influence of noise and to avoid calibration work [118].

2.4.4 Closed-loop Force Control Aided Microassembly

The first issue involved in implementation of closed-loop force control in microassembly is the fabrication or selection of a force sensor with proper measuring range and resolution. In [119], a survey on force sensing techniques in micromanipulation categorized force sensors into four groups based on their

working principles: strain gauge, piezoelectric force sensor, capacitive force sensor, optical sensor. Other related issues, such as force sensor calibration and force controller design were also covered in the article.

In microassembly processes, closed-loop force control was normally used for reliably grasping a component. In these cases, the force sensors were mounted onto the gripper fingers and the contact force control was normally achieved by controlling the motion of the gripper fingers [28, 36, 34]. [121] developed a micro force sensor with a resolution of $0.5nN$. The sensors were mounted onto a two-finger micro gripper and automatic micro manipulation experiment was carried out successfully. [120, 34] presented a PZT actuated gripper fabricated by LIGA technique and instrumented with semiconductor strain gauge force sensors for assembling biomedical microdevices. The grasping forces were controlled by a proportional integral (PI) controller. In a similar way, [36] developed a multi-degree-of-freedom microgripper mounted with strain gauge force sensors for handling photonics devices.

Besides grasping force control, micro force sensing and control techniques had also been applied in many other aspects of microassembly processes. [122] developed an "ortho-tweezers" for automated pick-and-place process. The "Ortho-tweezers" was a microgripper composing of two fingers orthogonally placed. Strain gauges were used in the force sensing module to achieve more accurate, faster motion. In [123], micro particles (the diameter of the particle is below $10\mu m$) were assembled semi-automatically into a desired pattern on the glass substrate by using an atomic force microscope (AFM) nanoprobe. [124] presented a closed-loop

optimal control enabled by force sensing technology, which was ready to be used in micromanipulation and microassembly tasks. This force sensor body was covered with polyvinylide fluoride (PVDF), and was able to apply a desired force on the object without compromising motion accuracy. [125] developed a micro force sensor that is suitable for high acceleration and high velocity conditions, and applied in wire bonding. The resolution of the force sensor was $1mN$. A salient feature of this force sensor was that it helped to solve the problem of the contradiction of high sensitivity and high position accuracy, by using a double-beam cantilever to replace the single-beam one. [126, 127] both applied force sensing methods in injection of bio-objects. [126] investigated the force behavior of living drosophila embryos by using a 2D PVDF-based micro-force sensor whose resolution was in the range of sub-μN. This experiment was a critical and major step towards automated bio-manipulation for batch injection of living embryos in genetics. [127] reported a micromanipulation system used for automatic batch microinjection of zebrafish embryos. The system employs both vision feedback for locating the object and force feedback for the injection process.

2.5 Conclusion

This chapter provided a review on researches in the emerging areas of microassembly. Microassembly tasks were categorized into parallel and serial microassembly. Although parallel assembly techniques can assemble mass micro components efficiently, it is unable to produce complex 3D micro structures composed of heterogeneous parts. In contrast, serial microassembly taking the

traditional way of assembling parts one by one, is more capable of producing complex micro devices.

Compared to the macroworld assembly tasks, microassembly differs greatly in two aspects: (1) Gravity gives way to adhesive forces to be the dominant force in microworld; these micro level forces include van der Waals, surface tension and electrostatic forces. (2) The high positional accuracy demanded in microassembly cannot be achieved by the traditional open-loop robots.

These differences require a fundamentally new approach to address each step of microassembly sequence: picking up, conveying, alignment, assembling and releasing. Consequently, a completely different assembly system technology is needed. A microassembly system consists of at least three functional units: the microgripper, the precision positioning units and the microscope system, which were discussed respectively.

As manual assembly of micro-sized parts is difficult and time consuming, there is a need to automate the assembly process. To this end, many techniques were developed and experimentally tested to facilitate the manually assembly or realize automated or semi-automated microassembly process. These techniques include the use of virtual reality (VR), visual servoing, closed-loop force control or combinations of them. VR based frameworks enable the operator to propose and visualize the assembly solution prior to physical assembly and provide the operator with more concise and clear information of the working area. Visual servoing was widely used for automating the alignment in microassembly processes and closed-loop force control for safely and reliably handling micro components.

Chapter 3

Micropart Design and Fabrication

3.1 Micropart and Scaffold Design

Many factors have to be considered in designing the shape of the microparts and the architecture of the tissue engineering (TE) scaffold [9]. As mentioned in Section 1.1, the desired scaffold architecture design should have the flexibility to enable changes in material, pore shapes, dimensions and interconnections. Because the microparts will be coated will cells and biological agents prior to the assembly process, it is preferable that in the whole assembly process, there are no thermal, electrical or chemical reactions involved.

In this project we chose a cross shape for the microparts for the following reasons. First, such a micropart can stand by itself, which makes it easy to pick up without adjusting the spatial orientation. Second, the microparts can also be so assembled by insertion from above. A 3DoF (*X*-*Y*-*Z*) robotic mechanism is capable of accomplishing such an assembly process.

The microparts will be hold together after assembly by friction and other adhesion forces. Both the picking up and assembly processes are more like a peg-into-hole

problem than just picking and placing in terms of the force applied. The pushing force both in the picking up action and assembly action will be controlled so as not to damage the micropart while providing sufficient force to accomplish the tasks.

The CAD drawing of the micropart can be seen in Figure 3.1. A hole is placed at the centre of the micropart to interface with the microgripper. The microgripper has a needle-like tip to be inserted into this hole on the micropart so as to pick it up. The picking up process is also a kind of peg-into-hole problem.

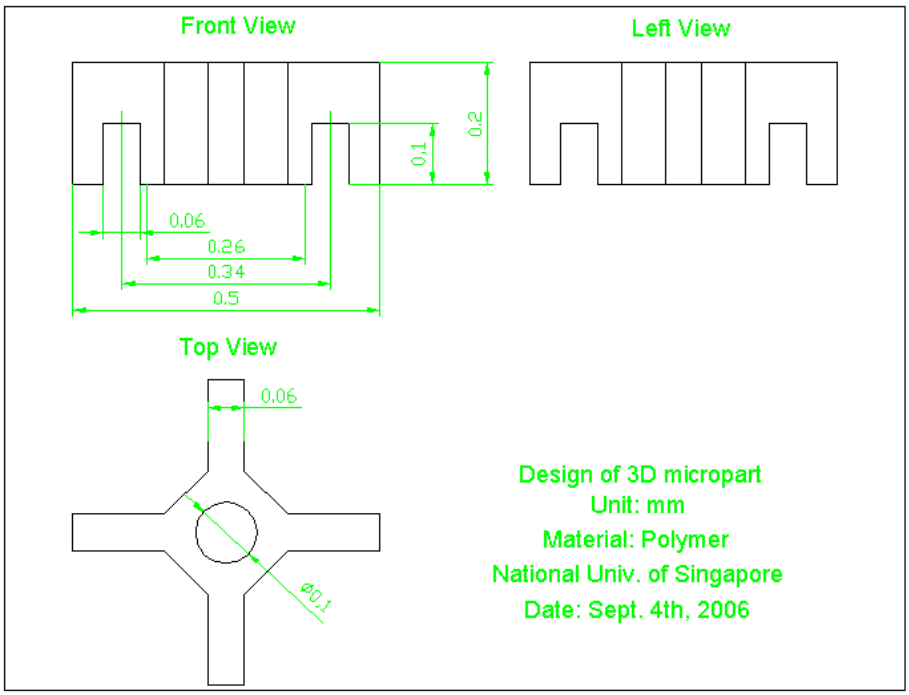

Figure 3.1: Micropart CAD drawing

There are two schemes to assemble the microparts together to form a scaffold. The first one can be used to assemble a pyramid as illustrated in Figure 3.2. The first layer connects points into lines. And the second layer connects lines into area. After the second layer, all microparts are connected together. This process

continues until there is only one micropart for the current layer; that is the last layer also the top layer.

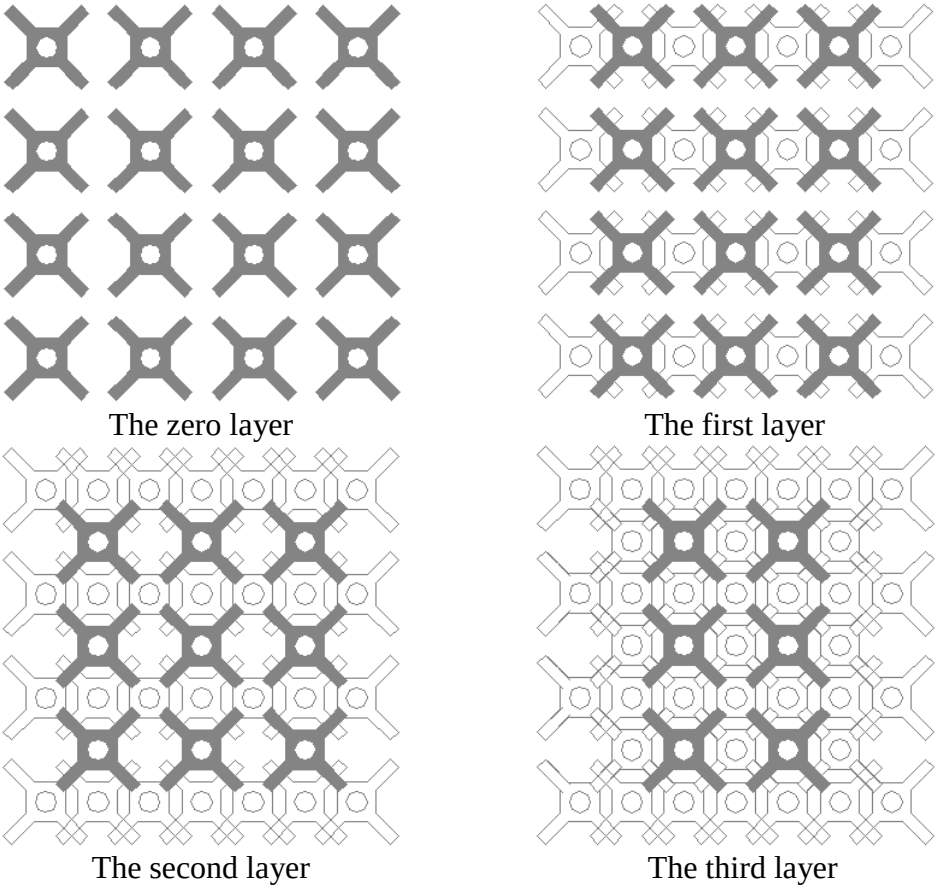

Figure 3.2: Pyramid scaffold architecture design (the grey microparts are the indicated layers).

The second scheme is for assembling a rectangular structure as illustrated in Figure 3.3. The first layer connects point into lines. And the second layer will repeat the array of the zero layer. The third layer makes connections between lines to form an area. After this layer, all microparts are connected. And then the fourth layer will repeat the shape of the zero layer again, which is the beginning of a new cycle. This process can be repeated as many times as wished. In fact, the base layer can be any shape other than a rectangle, and the second design can be combined with the first one to produce scaffolds of arbitrary shapes.

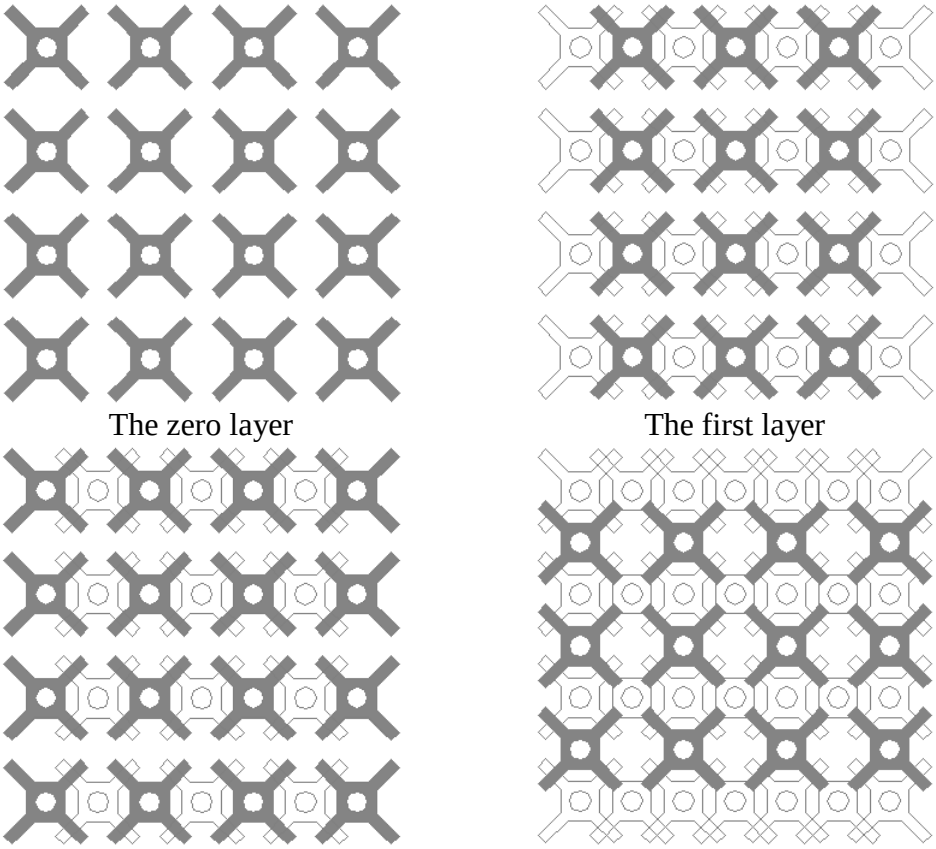

Figure 3.3: Cubic scaffold architecture design (the grey microparts are the indicated layers)

3.2 Microparts Fabrication Process

Many techniques used in MEMS industry may be used to fabricate microparts for this project, including optical lithography or stereolithography for photo-sensitive materials, and micromolding for none-photosensitive materials. Among them, photolithography can be used to produce a large number of microparts in one batch. And the microparts will be regularly placed on the wafer. These properties are critical for the automated microassembly task. A technique that involved both photolithography and plasma etching was developed to fabricate microparts [128].

From a pure mechanical point of view, the microparts should be compliant enough to accept the required deformation in the assembly process. Although the ultimate material will be both bioabsorbable and biodegradable (PCL [129]), at this stage of the experiment we used the biocompatible SU8 (commonly used photoresist in the field MEMS) for fabrication of microparts. The modulus of elasticity of SU8 is 4*GPa*, friction coefficient 0.19 and bond strength (pull test) about 20*MPa*, i.e. close to the mechanical properties of bones.

The fabrication process, which has been described in detail in [128], can be divided into two main steps. The first step is to create plateaus on the silicon wafer, which are used to form the notches of the microparts in a subsequent step. The second step is to fabricate cross-shape SU8 microparts. The patterned wafer will be covered with a 0.2*mm* thick layer of SU-8 100 and photo-patterned to create the "cross" shapes. A brief outline of the steps is described in the following paragraphs.

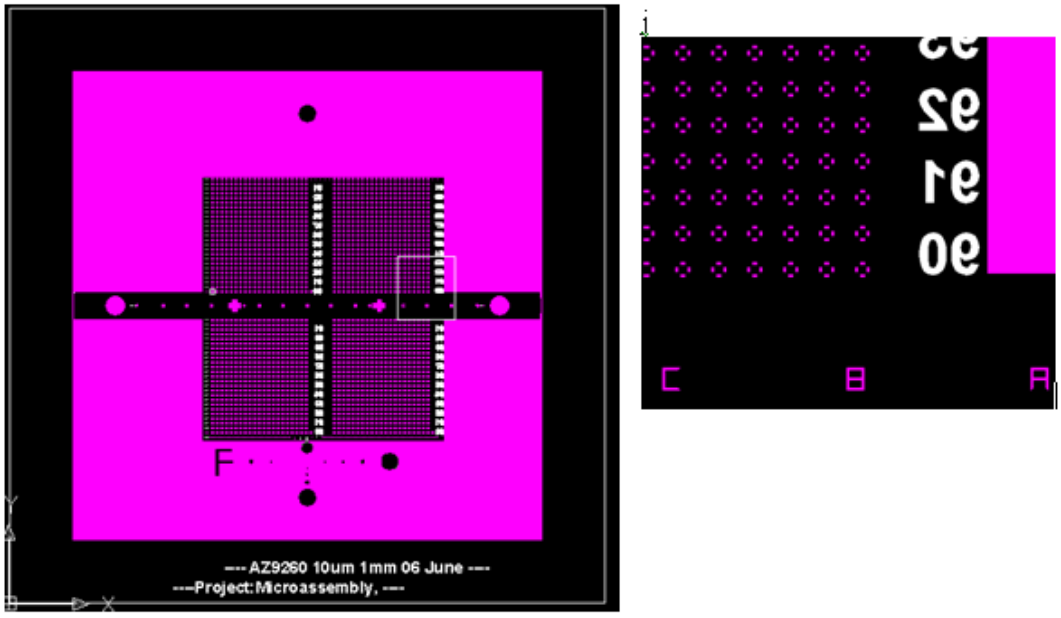

Figure 3.4: CAD drawing of mask used for creating plateaus (the number indicated of the diameter of the holes) the pink area will be covered with black emulsion on the printed transparency, and black area will be clear on the transparency.

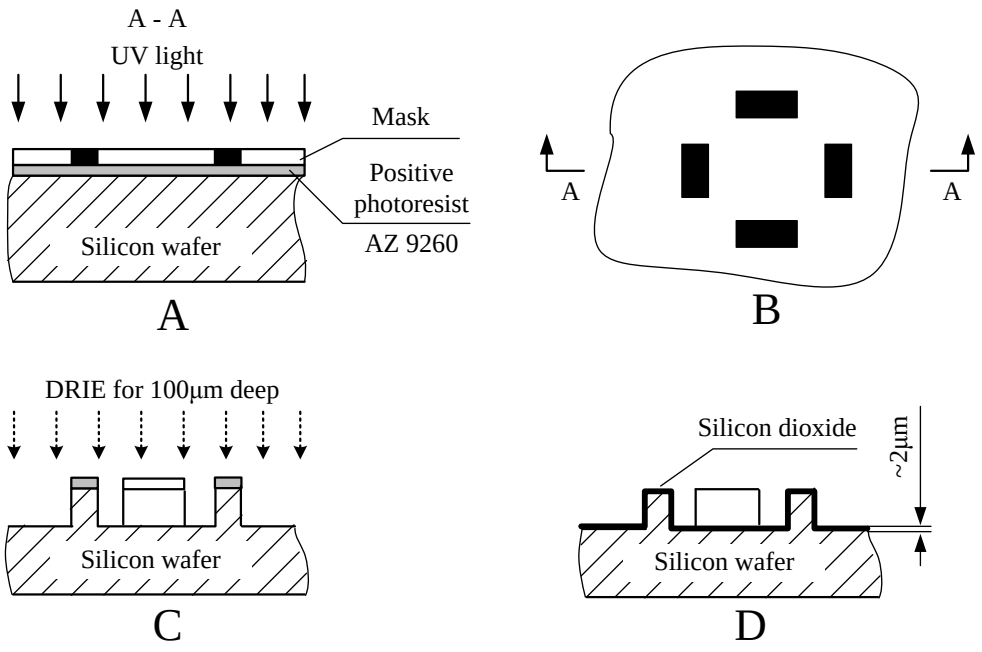

Figure 3.5: Process to create plateaus on a silicon wafer [128]. (A) Exposure and development to create plateau pattern with positive photoresist. (B) Silicon wafer covered with transparency mask (top view). (C) DRIE on the wafer to form 100μm-high plateau. (D) Remove photoresist and thermally oxidize the wafer to form a SiO_2 layer.

Figure 3.5 illustrates the process to create plateaus on the silicon wafer. First, the wafer is coated with a 10μm thick layer of positive photoresist, AZ 9260, followed by UV exposure and development. For the positive photoresist, the area that was covered by the black mask will remain on the wafer, while areas that were exposed under UV will be washed away by the developer. Second, the wafer is placed in a DRIE (deep reactive ion etching) etcher to create 110μm high plateaus. The areas that are covered with AZ 9260 will not be etched. Excluding the AZ 9260 layer, 100μm high plateaus are fabricated, which are used to form the notches on the parts. Third, the AZ 9260 layer is removed by acetone and a thermal oxide layer about 2μm in thickness is grown. This layer of silicon oxide is a sacrificial layer that will be used to detach the microparts from the wafer in the later process.

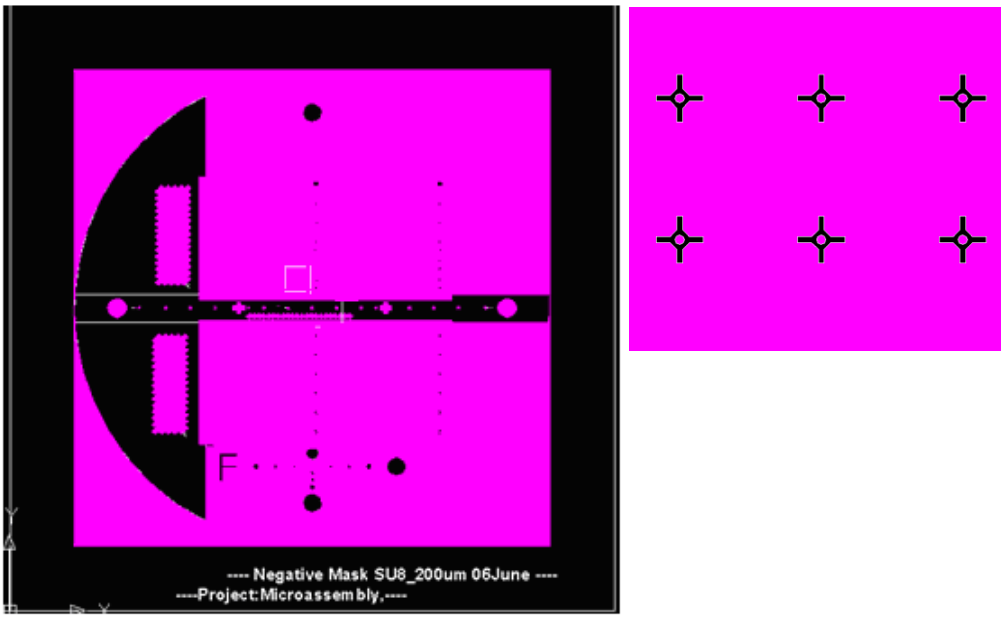

Figure 3.6: CAD drawing of mask used for fabricating cross shape SU8 with a through hole at the center; the diameter of the hole ranges from 90μm to 101μm.

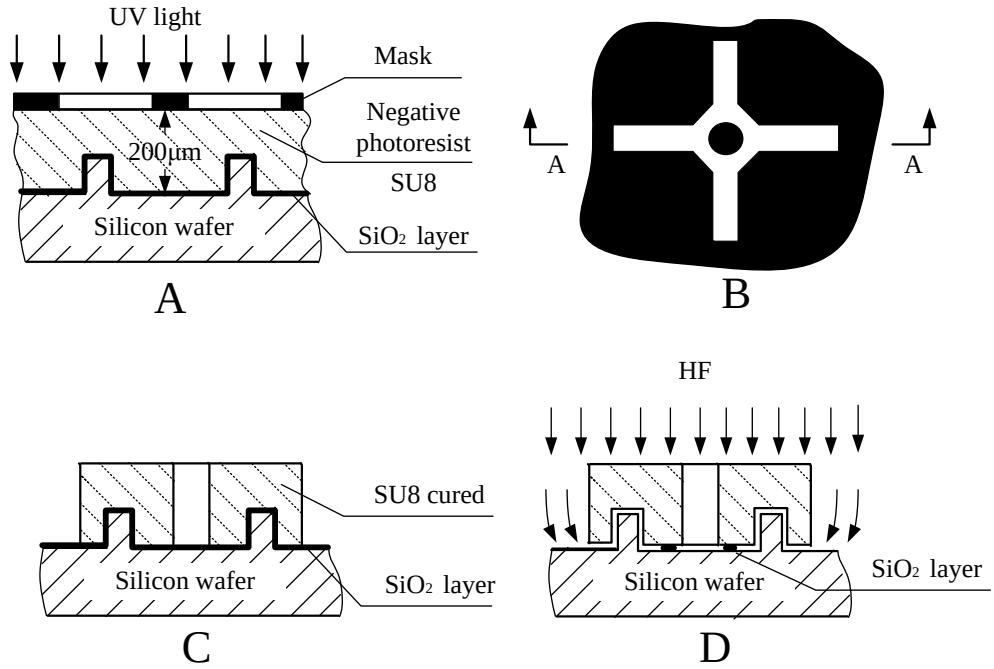

Figure 3.7: Creating microparts that can be easily separated from the wafer [128]. (A) Lithography with negative photoresist (SU8). (B) Patterned silicon wafer covered with transparency mask (top view). (C) Developing wafer arrayed with cross-shape SU8. (D) Putting the wafer into HF to remove most of the SiO_2.

Figure 3.7 shows the fabrication of the microparts. First a 200μm thick layer of SU8 (negative photoresist) is coated on the patterned wafer. Soft-baking is then carried out on a hot plate. The levelness of the hot plate is crucial to the final quality of the microparts. An unleveled hot plate will result in the reflow of SU8 and will cause varying heights of microparts or under prebaked SU8. The level of the hot plate should be adjusted with level gauges before baking. Second, the wafer is put onto a maskaligner for UV exposure and then developed. After developing, the polymer microparts are formed on the wafer. Third, the wafer will be put into HF (Hydrofluoric Acid) to dissolve the sacrificial oxide layer. The dissolution time can be controlled by observing the color changes of the wafer. The change of color is caused by the optical interference effect. The color will change from purple to white and back to purple again. After this is repeated four times, it means that the SiO_2 layer has been removed. Based on experiment, the dissolution time is about 90 seconds.

The base layer of the scaffold is also fabricated by the photolithographic technique. The CAD drawing of the mask for fabricating scaffold base is shown in Figure 3.8.

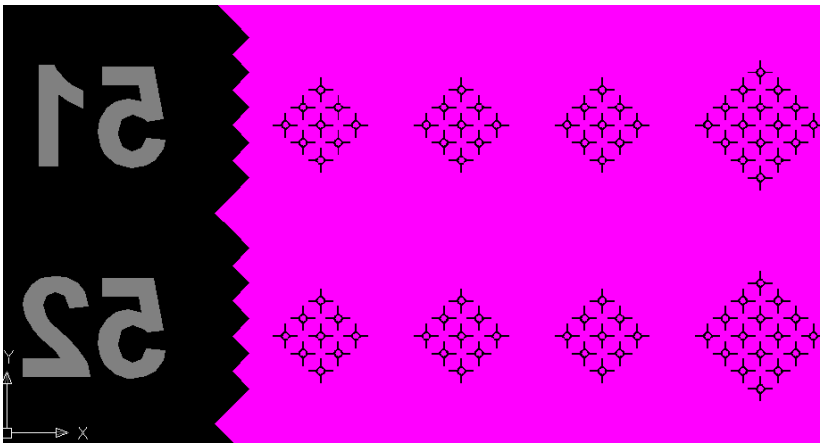

Figure 3.8: CAD drawing of the base layer mask (The number indicate the nominal wall thickness of the micropart on the base layer).

3.3 Factors that Influence the Quality of Microparts

3.3.1 Cross Section Shape of Plateaus

The shape of the cross section of the plateau will finally decide the shape of the notches of the microparts. Different etching plasma recipes and etching speed will result in different cross section shapes of the plateau. Figure 3.9 illustrates three typical shapes of the cross section of the plateaus.

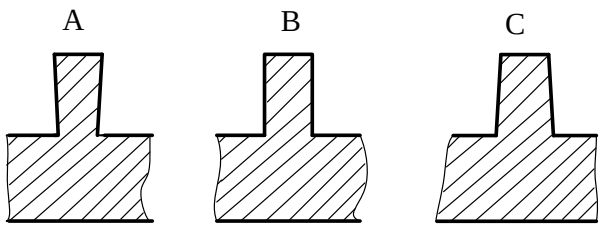

Figure 3.9: Three typical shapes of the cross section of silicon plateaus. A: The tope is larger than the bottom; B: The tope is equal to the bottom; C: The tope is smaller the bottom.

Type A: If the silicon wafer is etched under a high-speed recipe, the cross section of the plateau will normally take the shape of a trapezoid and the top is wider than the base. The advantage of this kind of plateau is that it lowers the criteria of the HF etching time after the SU8 has been fabricated. The HF etching time can be longer and even after all the SO_2 has been removed, the microparts will still be attached to the wafer because the plateaus will "hold" them. In contrast for the cases B and C, the HF etching time should be precisely controlled. A shorter etching time will make the microparts difficult to be picked up and a longer time will cause most of the microparts to fall off the wafer. In our project most of the microparts fabricated were of type A. The notch of a micropart is shown in Figure 3.10 (left): it takes a shape of a trapezoid.

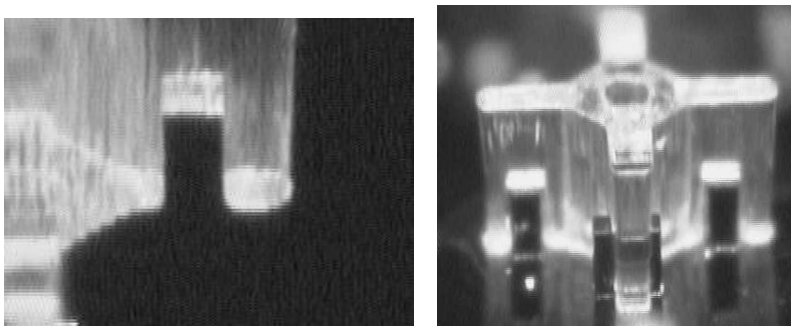

Figure 3.10: A trapezoid-shape notch seen from the bottom of the micropart (left) and a micropart with T-toping problem (right).

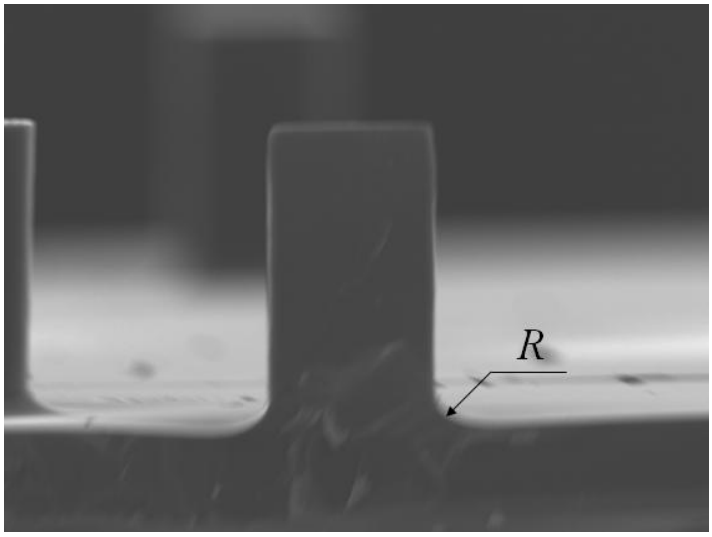

Figure 3.11: Cross section of a silicon plateau after two times of oxidization and HF erosion.

Type C is desirable in the assembly process because such kind of plateaus will produce a slope on the notches that will guide the notches to insert into the walls and reduce the alignment accuracy criteria. It is possible to produce such plateaus by decreasing DRIE etching speed, but this is difficult to realize experimentally.

Type B is a tradeoff between fabrication difficulty and quality of the final product. To facilitate the assembly process, fillets can be created at the feet of the microparts to guide the inserting action. To create fillets, the wafer will be put into HF after fabrication of the plateaus and oxidization in order to remove all the

silicon dioxide, and then the oxidization is repeated. By doing so, there will be a curve at the feet of the plateau which will create a fillet at the feet of the micropart. This oxidization and HF etching can be repeated many times to increase the size of fillet. Figure 3.11 is a SEM picture of a plateau after oxidization and HF erosion twice.

3.3.2 Dimensions of the Plateaus

The height and width of the plateau will finally decide the height and width of the notches of the micropart. In the design of Figure 3.3, a micropart at the edges may have only two notches to insert into the walls (such as the second layer). To keep it stable, its bottom has to be in contact with the second layer below it, so that in this case, the height of the notch should be larger than half the height of the micropart. In the experiment, it is difficult to precisely control the DRIE etching depth because the etching process is influenced both by the plasma recipes and the etching areas. The accuracy of the etching depth is about $5\mu m$.

During the DRIE etching, the covered area will not be totally free from the etching plasma. The width of the plateau will decrease as etching goes on. The width of the plateaus may also be influenced by other factors. To investigate the fabrication accuracy of the width of plateau, dozens of plateaus have been measured under high magnification optical microscope with the help of precise positioning workstation. Part of the data on the width of the plateaus is shown in Table 3.1.

Table 3.1: Width of plateaus whose design width are all 60μm.

Wafer	Width of plateaus measured						Mean
No. 1	55.6	54.8	54.9	55.4	55.8	54.6	55.2±0.2
No. 2	53.7	54.0	56.8	55.9	54.7	54.0	54.9±1.5
No. 3	54.0	56.9	55.8	53.6	53.0	56.8…	54.3±1.1

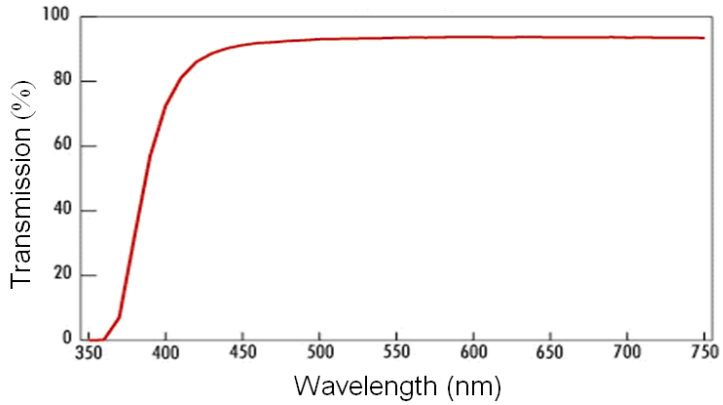

Figure 3.12: Transmission rate of Hoya UV-34 [132].

3.3.3 T-toping Problem of SU8 Cross

The photolithography process of fabricating SU8 cross is also affected by many factors. One of the most common quality problems with the SU8 cross is the T-toping problem: the top surface of the microparts is a little bit larger than the thickness of the walls (see Figure 3.10 right). In this project, the T-toping microparts would cause a total failure of the assembly process. The T-toping problem may be caused by a poorly controlled baking temperature, unqualified UV light, a gap between mask and wafer, intense heating on the surface layer of SU8 due to large exposure dosage at one time, etc.

The unqualified UV light

SU8 is sensitive in the near-UV region whose wavelength is about 365*nm*. The absorption spectrum of the photoinitiator for different concentrations can be found in [130]. The high absorption of the SU8 at wavelengths shorter than about 350*nm*

will overexpose the top layer of the SU8, causing a larger top. A solution to the problem consists of using a filter to cut down the wavelength to below 350*nm* [131]. In this project, we use a Hoya UV-34 UV long-pass filter. The transmission rate of the filter with respect to the wavelength is shown in Figure 3.12. Further technical specifications can be found in [132].

Figures 3.13 and 3.14 show two microparts fabricated on the same wafer. The two microparts went through exactly the same fabrication process except for the UV exposure steps: The first part was exposed to filtered and the other one to unfiltered UV light. It can be clearly seen that the second micropart has the T-toping problem.

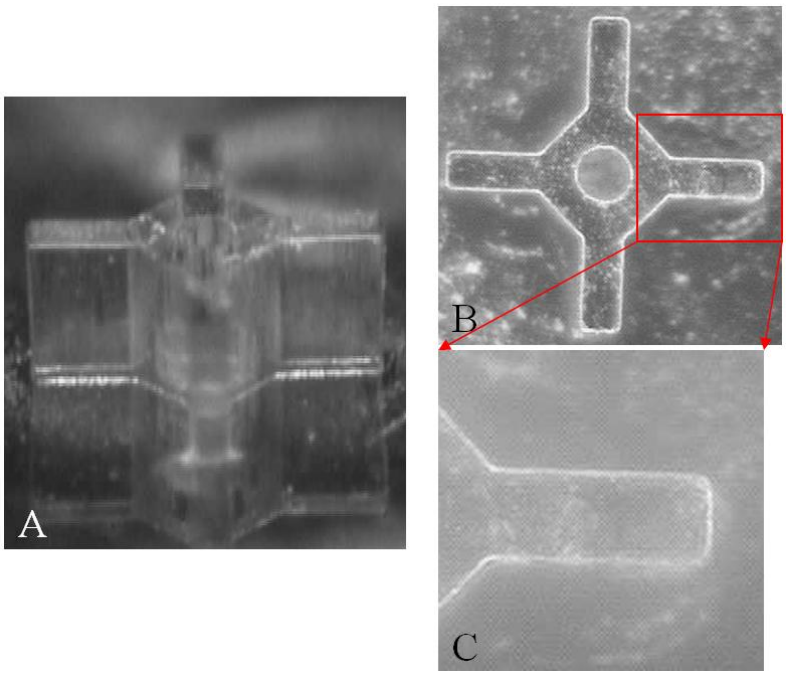

Figure 3.13: Micropart fabricated by filtered UV-light on blank wafer (no T-toping) (A) Micropart front view; (B) Micropart top view; (C) Part of micropart under high magnification optical microscope.

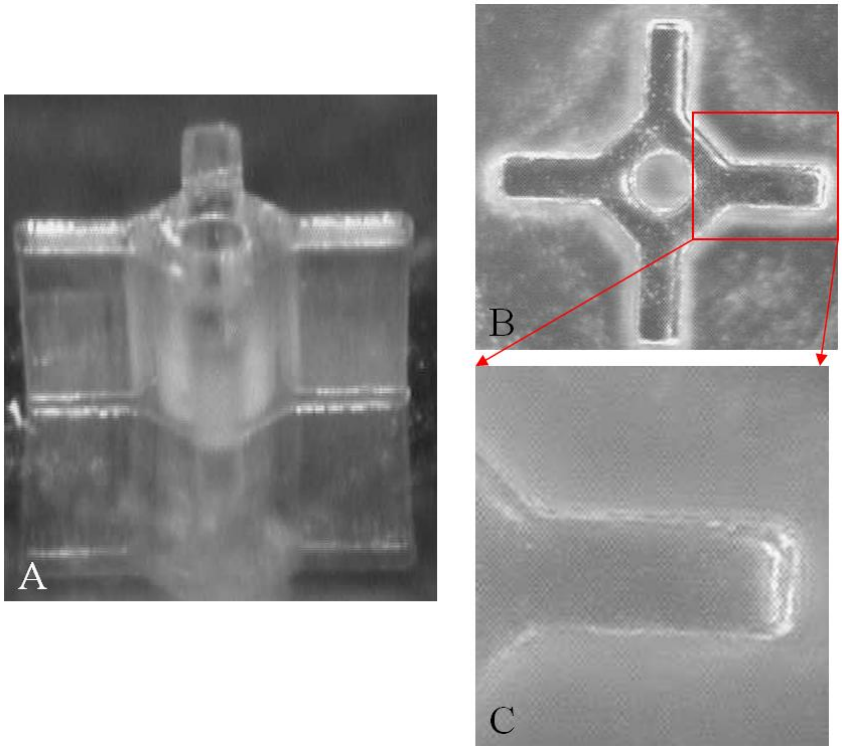

Figure 3.14: Micropart fabricated without filter on blank wafer (T-toping is observed) (A) Micropart front view; (B) Micropart top view; (C) Part of micropart under high magnification optical microscope.

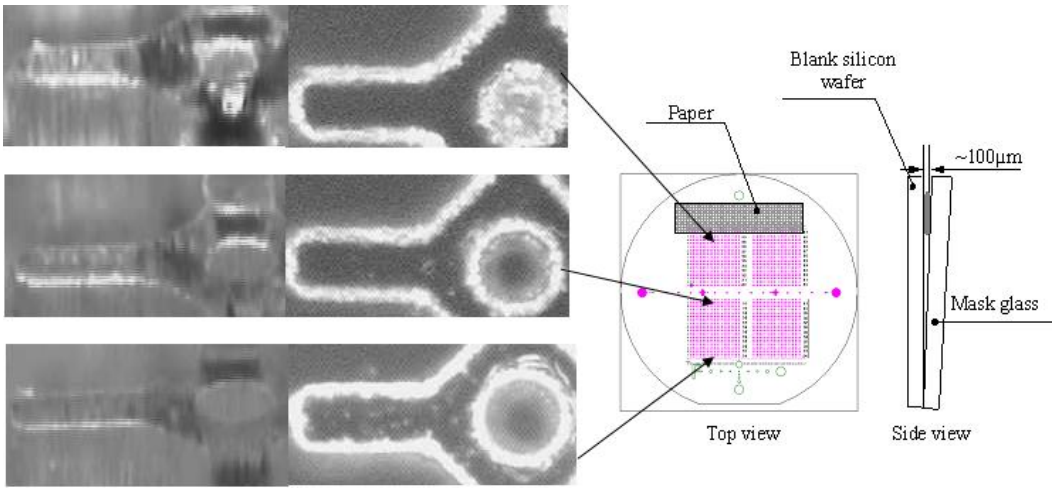

Figure 3.15: The influence of gap on the quality of the micropart (the left shows only one branch of the micropart, front view and top view). The larger the gap, the worse the quality will be.

Gap between the mask and the wafer

The gap between the mask and the wafer during the UV exposure step is also crucial. To investigate the influence of the gap on the quality of the micropart, we put a piece of paper between the wafer and the mask to form a V-shape gap when exposed. The experiment results are shown in Figure 3.15.

During microparts fabrication, unexpected gaps are often caused by the bubbles inside the SU8, which can be commonly seen after the spin coating process. For patterned wafer, it is almost unavoidable to have bubbles after SU8 coating. Large bubbles should be removed before pre-baking by sucking them out with syringes while small bubbles may be removed by longer pre-baking time.

Besides these two factors that will cause T-toping problems, the baking time and temperature, the exposure dosage also has influence on the quality of microparts. The UV exposure dosage for $200\mu m$ thick SU8 is about $400mJ$. Such a large dosage at one time will cause overheating of the surface layer of the SU8. This will cause the final product to have a "hard skin", i.e. a phenomenon similar to T-toping. Multi-exposure will help to avoid the "hard skin" problem. This consists of exposing the wafer with many small dosages and waiting 60 seconds between exposures to allow the wafer to cool down.

3.3.4 Dimensional Accuracy of SU8 Cross

To investigate the accuracy of the thickness of the walls, microparts with different nominal wall thickness and diameter of the hole were fabricated on a single wafer.

The actual thickness of the walls was measured under a high magnification microscope.

The measurement process goes as follows: Before measurement, the micropart wafer will be fixed on the precise positioning stages under top-view microscope. First a red horizontal line is drawn in the center of the microscope image (Figure 3.16). Second, the micropart is moved and the encoder is reset to zero when one edge of the wall get tangent to the red line. Third, the micropart is moved until the other edge is tangent to the red line. The encoder reading will give the thickness of the wall.

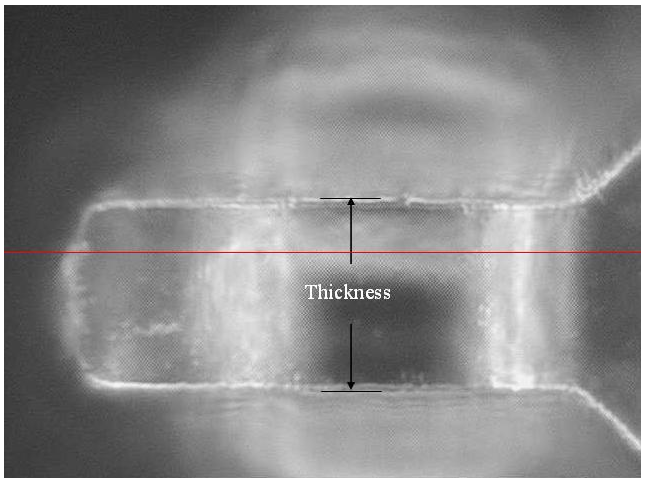

Figure 3.16: Measurement of the thickness of walls of micropart under high magnification optical microscope. (the red line is stationary, motion of micropart was accomplished by precision positioning stage and the encoder will give the thickness value.)

Table 3.2: Wall thickness of wall of microparts (sample wafer A): nominal value and actual value measured (The nominal value is the design dimension on the CAD drawing).

Nominal thickness	Mean	Thickness of wall of microparts					
55	60.0 ±0.4	59.0	60.7	60.0	60.4	60.0	
57	61.8 ±4.7	64.1	63.6	63.6	60.0	59.5	60.0
59	63.7 ±2.1	64.0	64.7	64.1	65.5	61.8	62.1

Table 3.3: Wall thickness wall of microparts (sample wafer B): nominal value and actual value measured (The nominal value is the design dimension on the CAD drawing)

Nominal thickness	Mean	Thickness of wall microparts					
55	66.8 ±0.2	67.0	67.2	66.8	66.1	67.0	
57	72.9 ±0.8	71.2	72.5	73.6	73.1	73.2	73.6

From Tables 3.2 and 3.3 we can see that the thickness error can be larger than 5μm, which is relatively large compared to the average dimension of 60μm. And for different batches of microparts, the errors will be even larger. This poses a great challenge for mass fabrication of the microparts.

3.4 Friction between the Microgripper and Part, and between Parts

Among the dimensions of the micropart, three are mating dimensions and thus are crucial for the assembly process: the diameter of the hole which mates with the diameter of the microgripper tip, the width of the notch and the thickness of the wall which mates with each other.

During the assembly process, the micropart will first be picked up and conveyed to the scaffold to get aligned with the other two microparts: the *receptor*. The micropart will then be pushed downward until the four walls of the receptor are seated into the notches of the micropart. Withdrawing the microgripper, friction between the micropart and the receptor will hold the micropart. In order to ensure that the microparts will cleave together with the receptor rather than attached to the microgripper after retracting, the diameter of the hole and the thickness of the

walls were specifically selected to make the friction between the microgripper and the micropart smaller than the friction between notches and walls.

A batch of testing microparts with hole diameter from 90μm to 101μm was used to measure the frictions between microparts and the microgripper and so investigate the relationship between friction and the mating dimensions. And for measuring the friction between notches and walls, a base wafer with wall thickness from 50μm to 60μm was designed and fabricated.

Friction between the microgripper and microparts

For a given microgripper, 80 microparts were used to measure frictions between the microgripper and microparts. The nominal diameter of the hole of the microparts ranged from 93μm to 100μm in steps of 1μm, and 10 microparts were tested for each size.

The measuring process goes as follows. First the microgripper is aligned with a micropart manually and then picked up automatically (the automatic picking up process will be described in Chapter 5). Second, the micropart is conveyed to the releasing structure and the top of the micropart is then pushed against the releasing structure and the gripper is withdrawn slowly. The force acting on the top of the part begins to increase and when it reaches a certain level, the micropart is removed off the gripper. Figure 3.17 shows a typical force profile while removing a micropart from the gripper. The minimum value of the force sensor reading gives the static friction between the micropart and the gripper.

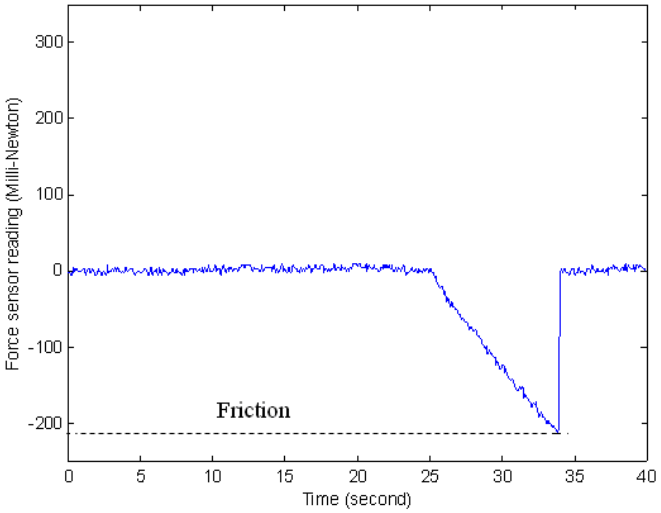

Figure 3.17: Force profile of releasing a micropart against the releasing structure. The minimum value gives the friction between the microgripper and the micropart

Because the releasing structure cannot apply an evenly distributed force on the top of the micropart, the micropart will tilt a little bit when pushed against the releasing structure, which makes friction measured this way a little bit larger than the gripper-micropart friction in assembly.

The friction values are shown in Figure 3.19, which also shows the successful picking up rate. Unsuccessful pick-ups results from two causes: For microparts whose nominal hole diameter is smaller than 94μm, unsuccessful pick-up happend when the hole is too small for the microgripper tip to be inserted under an automatic picking strategy. For the microparts with nominal hole diameter larger than 95μm, the gripper tip can always be inserted into the hole, but sometimes the friction is not large enough to lift it up.

Friction between notches and walls

During the assembly process, the four walls of the other two microparts (the receptor) will be inserted into the four notches of a part (Figure 3.12). To measure

frictions between notches and walls, about 50 receptors were tested. For each receptor, the friction was measured only once. The thickness of the wall of the receptor varies from 49μm to 54μm in steps of 1μm. For each size, about 10 receptors were measured.

To measure friction between notches and walls, a micropart needs to be fixed on the microgripper. The micropart fixed on the microgripper has a 92μm diameter hole to guarantee a firm connection between the microgripper and the micropart. The micropart with such a small hole cannot be picked up automatically: they are picked up by applying a much large inserting force manually. After pick up, the micropart is conveyed to the base wafer and aligned with a receptor. The automatic assembly action is then executed (the automatic assembly action will be described in Chapter 5). When withdrawing the microgripper slowly, the force value drops. The minimum value is the friction between notches and walls. A typical force profile during assembly process is shown on Figure 3.18.

For each micropart used for this end, the assembly trials begin with 49μm wall thickness and ended with 54μm wall thickness. And if the micropart does not fell off the microgripper through out the whole process, it will be tried from 49μm wall thickness again. After 15 trials, i.e., 3 rounds of trials from 49μm wall thickness to 54μm wall thickness, the part is abandoned on the releasing structure and another micropart is used. Totally 6 microparts were used in this measurement: 4 of them were assembled on the base wafer and 2 abandoned.

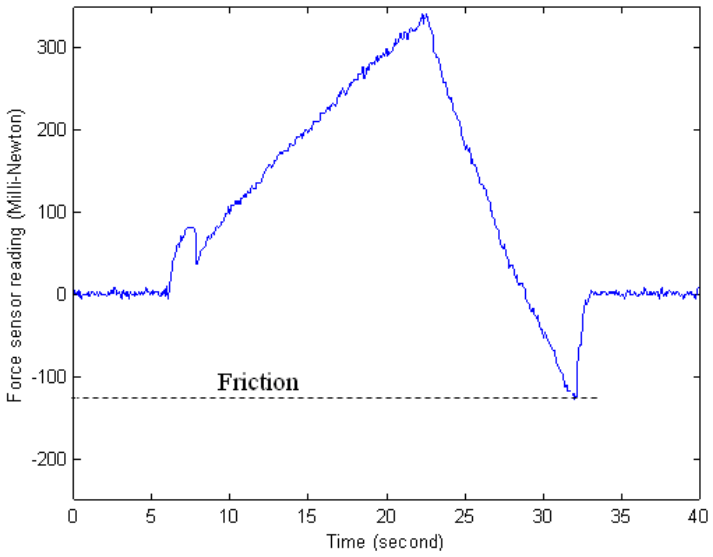

Figure 3.18: Force trajectory of assembling a micropart. The minimum value gives the friction between notches and walls.

For mass fabrication of microparts, the nominal diameter of the hole of the part is set to 98μm where the successful picking up rate is relatively high (about 70%) and friction between microparts and gripper is small, 8.3mN on average, (Figure 3.19). In the automated microassembly experiment, this friction will be further adjusted by modifying the diameter of the gripper tip (see Section 3.2.4). The change in the diameter of the microgripper tip is of the sub-micron level. The thickness of the wall in mass fabrication ranges from 40μm to 60μm to cover all possible plateau widths. Only the microparts with proper wall thickness were used in the assembly experiment.

The force between micropart and wafer during the picking up process is not measured because no obvious force was observed. A typical pick-up force trajectory is shown in Figure 3.20. We see that the force between part and wafer is negligible.

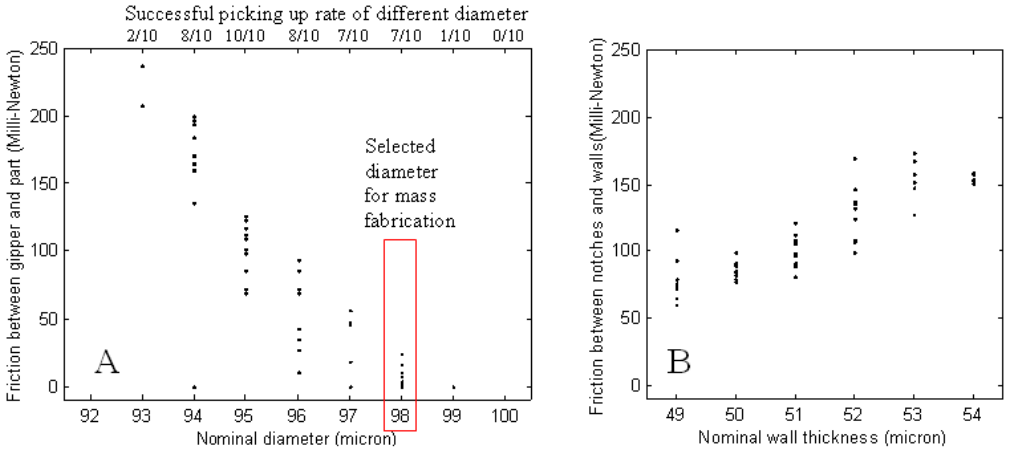

Figure 3.19: (A) Friction between a microgripper and a micropart; (B) Friction between notches and wall of different thickness.

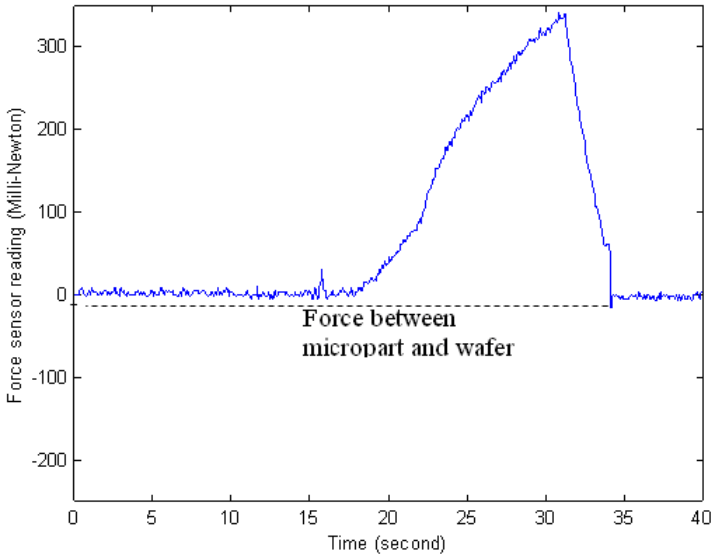

Figure 3.20: Force trajectory of picking up a micropart.

Weight of the micropart is given by

$$G = \rho V g \approx 1.2 \times (1.0 \times 0.06 \times 0.2 \times 10^{-3}) \times 9.8 = 1.411 \times 10^{-4} mN . \qquad (3.1)$$

The weight of the micropart is orders of magnitude smaller than friction and so in the assembly process the gravity of the micropart and all other inertia forces are neglected.

3.5 Properties of Fabricated Microparts

The fabricated micropart is shown in Figure 3.21. To test the feasibility of the whole assembly idea, a small cubic scaffold was assembled with the cross-shape microparts handled by the microgripper. Figure 3.22 shows the rectangular scaffold that was successfully assembled.

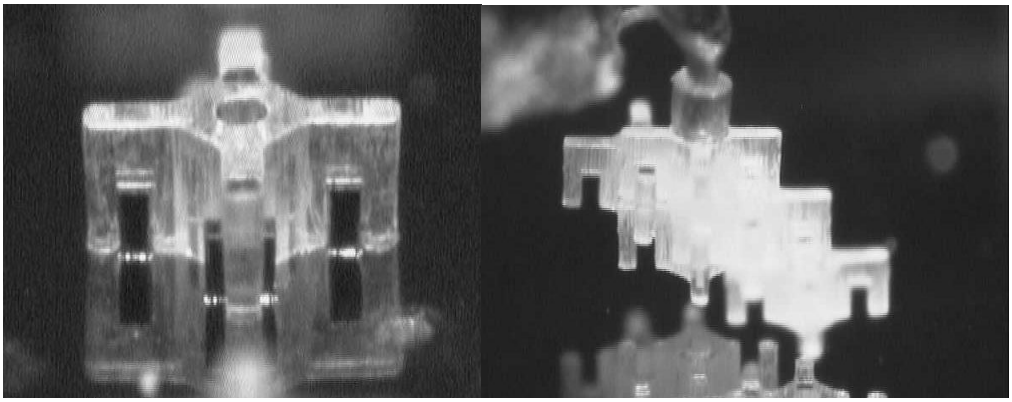

Figure 3.21: Microparts cleave together by friction between them, as is demonstrated by lifting the assembly using the microgripper inserted into the hole of the top micropart.

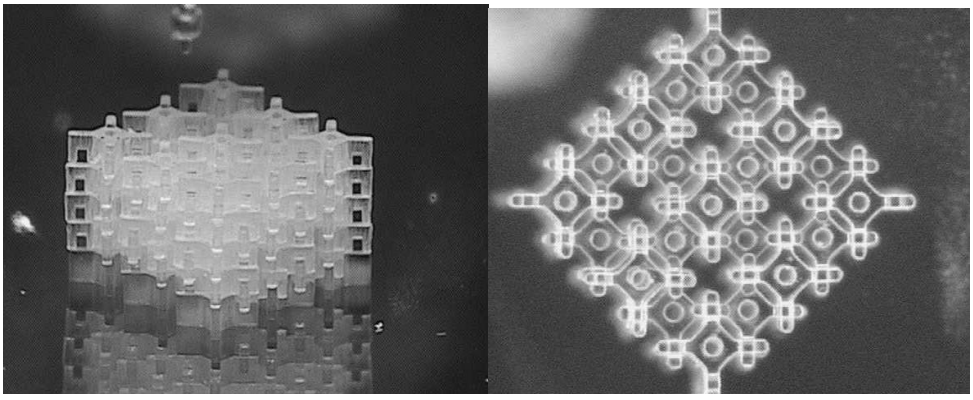

Figure 3.22: A 9-layer rectangular scaffold of a 3×3 base (front and top views).

3.6 Summary and Discussion

In this chapter, I presented the design of the 3D microscopic parts and the architecture of the tissue engineering scaffold assembled with this kind of parts. The fabrication process and many key factors that influence the quality of the microparts were also discussed.

There are two main steps in the fabrication process: the creation of plateaus on the silicon wafer, and the fabrication of cross-shape SU8 parts. After fabrication, the microparts will be regularly arranged as an array on the silicon wafer, which makes it easy to locate the parts in the automated assembly process. After assembly, the microparts cleaved together by friction, and after a certain number of layers all the microparts interlocked together to form an integrated scaffold. No heat, pressure or chemical was involved in the whole process.

Factors that influence the shape and dimension qualities of the plateau and SU8 polymer cross were discussed. These factors include the DRIE etching recipes and speed, the quality of UV light, baking time and temperatures, and the gap between wafer and masks. Suggestions to control these factors were also given.

Friction between microgripper and microparts and friction between microparts are crucial for the assembly process. For each successfully assembled micropart, the friction between the part and gripper must be smaller than the friction between the part and the two parts under it. To investigate the relationship between friction and mating dimensions, friction at different mating dimensions were measured.

A major drawback of the fabrication technique is the low relative accuracy in the microparts dimensions, which is one of the toughest obstacles on the way towards automated microassembly. In the macro domain, for example, it is easy to reach an accuracy of 0.1*mm* on a part whose dimension is 500*mm* by means of milling or turning techniques. The relative error in this case is 0.02%. However, in the microscopic domain, for instance in this project where we used photolithography technique to fabricate microparts, the thickness of the wall was 60μm and the error about 5μm meant a relative error of about 8.8%. To address this problem, during the assembly process, each micropart has to be tested, and the unqualified micropart will be abandoned on-line.

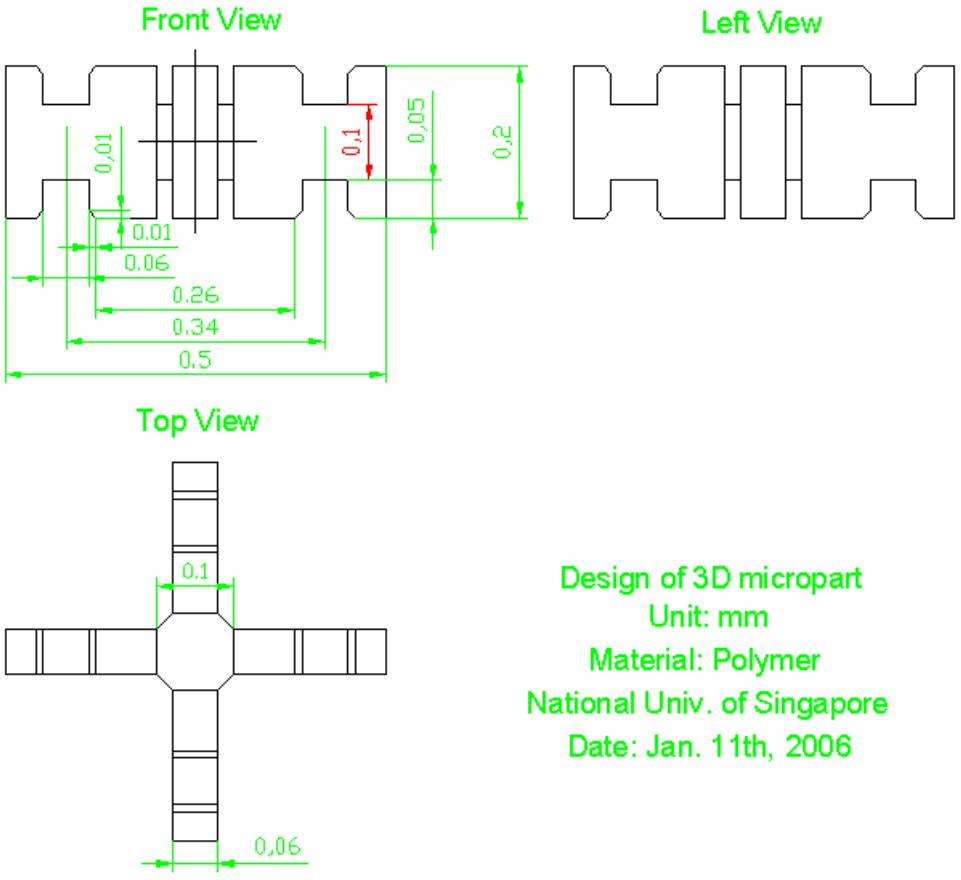

Figure 3.23: CAD drawing of the symmetric design of the micropart for micro-molding.

The material used here is SU8, which is photosensitive but not bioresorbable. In future, poly (ε-caprolactone) (PCL) will be used for fabrication of the microparts. PCL is both biocompatible and biodegradable and it has similar mechanical properties with SU8. Details on materials selection can be found in [133]. A possible way of fabricating such microparts is by using of micro-molding technique. A symmetric design of the micropart is proposed for micro-molding in Figure 3.23. This design would facilitate both the micromolding and the assembly processes.

Chapter 4

Design and Fabrication of Microgripper

4.1 Design of Microgripper

A two-finger microgripper made of shape memory alloy (SMA) was developed in [43] to build tissue engineering scaffold by micro-assembly of building blocks. However there were two major limitations with this gripper that hindered its use in the automated microassembly task. The first was that the gripper is bulky. The SMA gripper was about $2mm \times 5mm$ viewed from top. This relatively large size occluded the part to be picked up when viewed by the top-view microscope, which was essential for automated alignment in my selected scheme. The second limitation was the unpredictable relative position between the gripper and the micropart it holds. As reported in [133], when the micropart made contact with the scaffold, it would slide against the gripper. If the impact force is too large, the micropart may break away suddenly. These limitations posed great challenges to automating the assembly process.

The inspiration of a new microgripper design came from peg insertion. We envisioned that by inserting a peg into a hole fabricated on the micropart, this

micropart will be stably "grasped" by the peg, and it will thus become possible to control its position and orientation. In order to leave the space over the micropart free when viewed from the top, an L-shape microgripper was designed, as shown in Figure 4.1. The arm which held the gripper was a cantilever beam structure and it also functioned as a mechanical amplifier to produce a larger torque at the fixed end where a force sensor was mounted.

The gripper probe had a metal tip and a pushing shoulder. The tip was less than 100μm in diameter, so as to interface with a through hole on the micropart. The tip was designed to be 180μm in length, which was shorter than the height of the micropart by 20μm. This will guarantee full contact of the part with the pushing shoulder after insertion.

The pushing shoulder, made of SU8, was fabricated by using photolithography. The outer diameter of the pushing shoulder was about 200μm, which was small enough so as not to occlude the parts in the top-view, while at the same time large enough to apply a pushing force on the top surface of the micropart during assembly. The height of the pushing shoulder was selected as 150μm, a tradeoff between the strength of the component and fabrication difficulties. The strength will be increased with a longer height, but that will make the fabrication process more difficult as a thicker layer of SU8 coating will be required, thereby needing a larger exposure dosage causing more control problems.

The L-shape microgripper had the following advantages over the two-finger SMA microgripper:

1. Low cost. Compared with the old design, this microgripper was much simpler and hence cheaper. During the automated microassembly experiment, the microgripper was one of the most fragile elements, and so low cost and easy exchange were highly desirable.
2. Fixed relative position between the microgripper and the micropart being handled. For the two finger microgripper, the contact point on the micropart could be any parallel surfaces on the micropart, but for the L-shape microgripper, the contact point must be the hole and the top surface of the micropart which made the relative position between microgripper and micropart the same for all the microparts grasped. This fixed relative position also meant that the relative position between the precise positioning stage and the micropart was known, which simplified the closed-loop position control based on vision feedback.
3. Evenly applied force on the top surface of the micropart. The evenly applied force provided by the pushing shoulder prevented tilting and sliding of the micropart when coming in contact with the scaffold, which makes automated inserting action feasible.

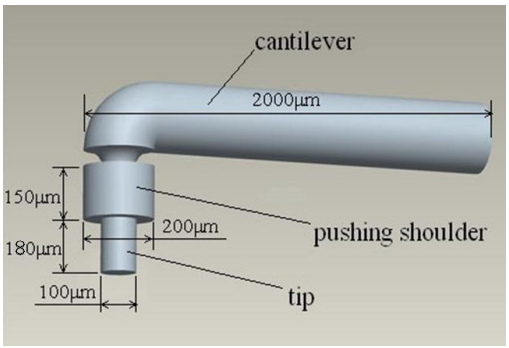

Figure 4.1: Design of L-shape microgripper.

4. Ease to integrate force sensing in the arm. With this L-shape microgripper, it was easy to incorporate a force sensor as shown in Figure 5.4.

4.2 Fabrication of Microgripper

Tungsten was chosen to fabricate the main body of the gripper for its excellent mechanical properties (hardness 14*GP*a and Young's modulus 380*GPa* [134]). Since the invention of STM in the 1980s, tungsten was widely used for fabricating tiny sharp tips. Possible fabrication methods with tungsten include electrolyte or electrochemical etching, chemical polishing/etching, ion milling, cathode sputtering, etc. [135]. Electrolyte etching was adopted here for its low cost, simplicity and ease of observation.

4.2.1 Total Charge and Tungsten Tip Diameter Relationship

The electrochemical reaction of dissolution of tungsten in an alkaline solution is given by [136]

$$W + 8\,OH^- \rightarrow WO_4^{2-} + 4H_2O + 6e \,. \tag{4.1}$$

When a voltage is applied to the tungsten rod (anode), the etching process will take place at the air/electrolyte interface. In the electrochemical reaction, the tungsten rod will be oxidized and the resultant tungstate anion (WO_4^{2-}) is soluble in water. According to Faraday's Law of electrolysis, the mass of the substance altered at an electrode

$$m = (\frac{Q}{F})(\frac{M}{z}) \,, \tag{4.2}$$

where, Q the total electric charge passed through the substance, F the Faraday constant, M the molar mass of the substance, and z the valence number of ions of the substance (electrons transferred per ion).

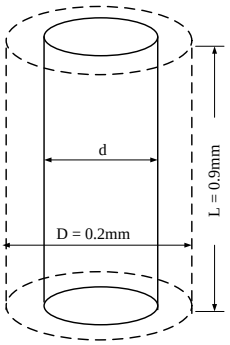

Figure 4.2: Calculation of the weight etched off if we assume that the tungsten tip remains a cylinder shape all the time. The length immersed into electrolyte is 0.9*mm*.

The total charge Q is the electric current $I(\tau)$ integrated over time τ

$$Q = \int_0^t I(\tau)\, d\tau \,, \tag{4.3}$$

is obtained by a specially designed circuit and a computer, as will be explained in Section 4.2.3.

If we assume that during the etching process the tungsten tip remains at a cylinder shape (Figure 4.2), the mass of tungsten etched off the tip is then given by:

$$m = (\frac{\pi D^2 L}{4} - \frac{\pi d^2 L}{4}) \times \rho \,. \tag{4.4}$$

In the experiment, the original diameter of the tungsten rod was 0.2*mm* and the length immersed into KOH solution 0.9*mm*. From Equations (4.2) and (4.4) we get the following relationship between the diameter d and the total charge Q,

$$d = \sqrt{D^2 - \frac{4MQ}{\pi L \rho z F}} \,. \tag{4.5}$$

In our case, the values of all parameters are listed in Table 4.1. From Equation 4.5 we can see that the diameter of the tungsten tip can be controlled by controlling the total charge *Q*.

Table 4.1: All parameters for calculation of the etched diameter.

Faraday constant (F)	96485.3383 C/mol
Density of Tungsten (ρ)	19.25 $g \cdot cm^{-3}$
Atomic weight (M)	183.84 $g \cdot mol^{-1}$
Valence number (z)	6
Original diameter (D)	0.2 mm
Length (L)	0.9 mm

To precisely control the etching charge during the tungsten tip etching process, a circuit was designed and implemented (Figure 4.3). The resistance of the power resistor is a constant value. By reading the potential of the power resistor, the current going through the electrochemical circuit is known in real-time. The sampling rate of the ServoToGo card for reading potentials from the power resistor is 100*Hz*. Total charge can then be obtained by integrating with time by the computer.

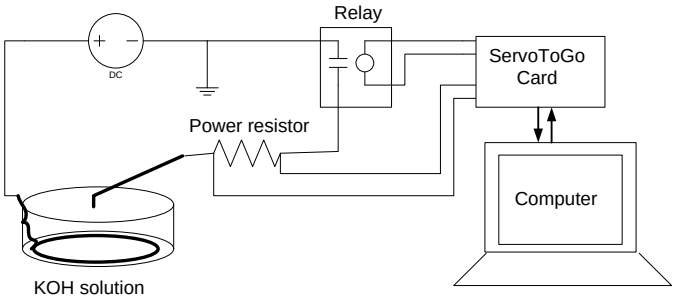

Figure 4.3: Etching charges control circuit

4.2.2 Current-Voltage Relationship

To find the proper voltage used for electrochemical etching process for a given tungsten tip, the current values under deferent voltages is recorded (Figure 4.4).

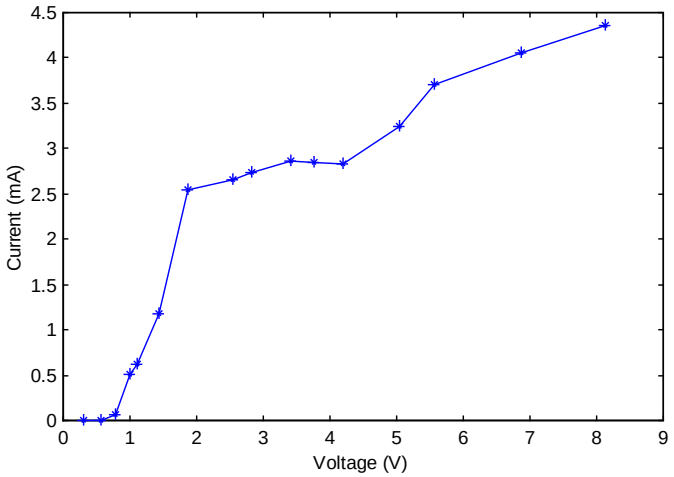

Figure 4.4: Typical current-voltage relationship obtained during electrolyte etching of the tungsten tip.

Similar *I-V* curves were also reported by [137, 138]. We see in Figure 4.4 that when the voltage increases from zero to a certain value, the current will increase dramatically, and then enter into a plateau, that is, although voltage keeps increasing, the current remains relatively stable. As reported by [137], an applied voltage larger than the plateau phase will result in violent electrochemical reactions and hence produce cavities, holes and poor quality of the surface on the tungsten part. So in our experiment, for coarse etching, the DC power is set to be about $5V$ and for final fine etching the voltage is reduced to about $1V$.

4.2.3 Experiment Setup

The experimental setup for fabrication of the microgripper included a set of precision positioning stages (PI M-511 series), three sets of optical microscopes, a plastic container, a DC power supplier, a data acquisition card (ServoToGo card) and a PC. The precise position stages were used to manipulate the tungsten tip and the fabrication process observed under the microscopes. Electro-chemical etching

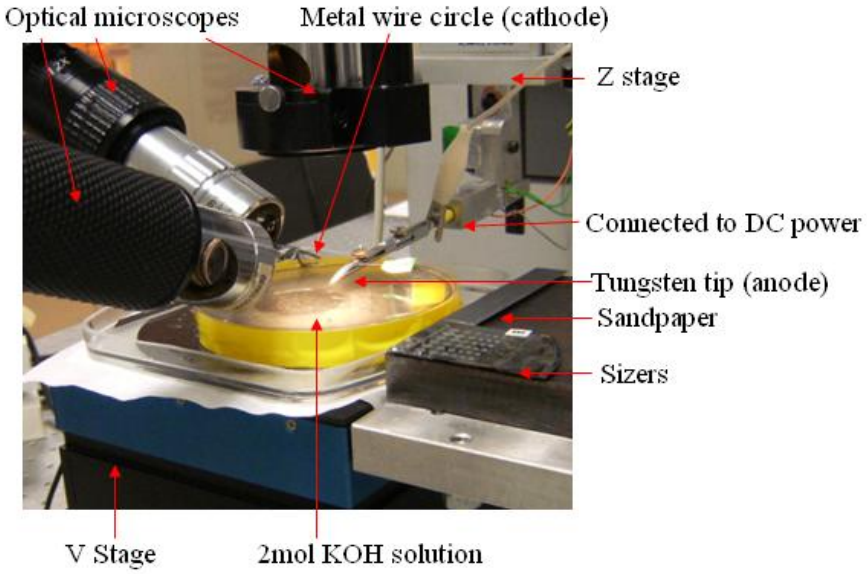

Figure 4.5: Microgripper fabrication setup.

charge control was accomplished by a circuit and the computer. The whole setup was placed on an anti-vibration table in order to avoid perturbations.

A closed-up view of the experiment setup is shown in Figure 4.5. The tungsten rod was clamped by a clamper mounted on the *Z* stage, and the whole etching process was monitored using two microscopes. The length immersed into the KOH solution was controlled by both the *Z* and *V* stages. The electrolyte used was 2*mol* KOH solution.

Microgripper fabrication software

The software used for fabricating microgripper provided a friendly interface for the user to manipulate the precision workstation and observe the etching process through the optical microscopes. The software was also used to monitor the current, voltage, etching time, and shut off the power supply of the etching circuit automatically, so as to control the diameter of the tungsten tip during the etching process. Automated grinding process was also controlled by this software.

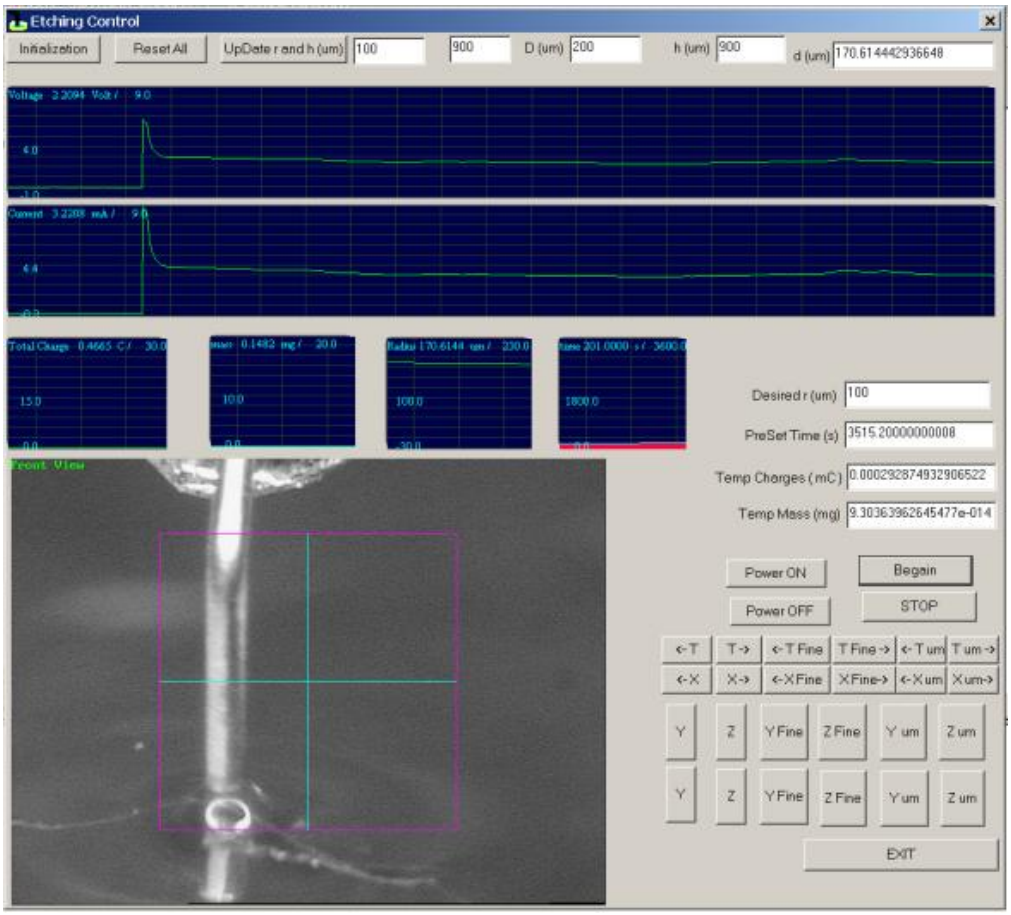

Figure 4.6: Graphical user interface of microgripper fabrication software.

This software also allowed the user to set the desired diameter before etching, and the DC power supply will be cut off when the diameter reached this value. The diameter accuracy that can be achieved in this way was about 10 microns. The low accuracy was due to the irregular shape of the ends of the etching part of the tungsten rod and the inaccuracy of the length immersed into the KOH solution. After coarse etching, the diameter of the tungsten rod can be estimated from the number of pixels of the tungsten tip on the screen, or for higher precision using the sizer. After measurement, the diameter of and etching length of the tip should be updated on the GUI and etched again. The detailed fabrication process is described now.

4.2.4 Fabrication Steps

1. Bend the tungsten rod manually with a modified tweezers after cleaning with acetone. The angle of the bent tungsten rod is larger than 90^{o} to leave some space for the clamper. After bending, the tungsten rod is mounted on the *Z* stage through a clamper. The angle of the clamper is adjusted so that the tungsten tip is perpendicular to water level contours (Figure 4.8 A).
2. Immerse the end of the tungsten rod into the KOH solution by operating the *Z* stage manually. Leave the 0.9*mm* tungsten rod above the surface of the solution, and etch off all the longer part.
3. Move the 0.9*mm* long tungsten rod into the electrolyte and set the desired diameter to 110μm and start etching (Figure 4.8 B). The reason for etching such a long tip is to avoid tapered cylinder shape at the end. After the DC power is disconnected automatically, draw back the tungsten tip and clean the tip carefully with dust free papers immediately. Long exposure of the etched tungsten in the air will cause the surface to coat with probably WO_3 [138], which is hard to remove (Figure 4.8 C).
4. Estimate the diameter of the tungsten tip by measuring the pixel distance of the tungsten tip on the microscope images. Update the diameter value on the control software GUI, and set desired diameter to 100μm, and start etching again.
5. Draw up the tungsten tip by 380μm, and then etch off the longer part (Figures. 4.10 D, E).

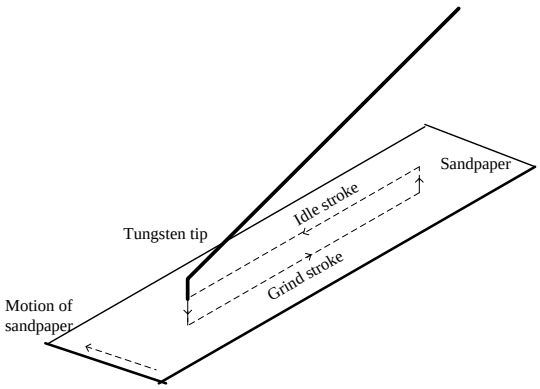

Figure 4.7: Relative motion of the tungsten tip against sandpaper in grinding process.

6. Move the tungsten tip to the sandpaper, push it against the sandpaper and then click auto-grind button to start grinding process. Grinding is used to remove the sharp end of the tip (Figure 4.8 F).
7. In each cycle only one stroke is used for grinding, that is the stroke whose relative moving direction is opposite to the bend direction of the tungsten tip so as to avoid breaking of the bending point. After each cycle, the sandpaper will move to one side by 100μm in order to avoid over-wearing a particular track on the sandpaper (Figure 4.7).
8. Measure the diameter of the tungsten tip with the *sizer* (Figure 4.8 G) (*sizer* is a set of microparts fabricated on a silicon wafer with the size of the holes of the microparts range from 95μm to 105μm in steps of 1μm) and then update the etching length and diameter on the GUI to prepare for the final fine etching. By repeating the measuring, updating, and etching steps, the tungsten tip diameter accuracy can become smaller than 1μm.
9. After the tungsten rod is ready, move it to the pushing shoulder wafer. Pushing shoulder made of SU8 is fabricated by using photolithography technique, i.e. as for microparts. The inter diameter of the pushing

shoulders ranges from 70μm to 100μm. Select a proper pushing shoulder and insert the tungsten tip into the hole. The connection between the pushing shoulder and the wafer will be broken by the insertion (Figure 4.8 H).

10. Withdraw the tungsten rod; the pushing shoulder will come up with the tungsten tip. Then insert the tip into a larger hole, move downward the tungsten tip to push the pushing shoulder to the upper end of the tungsten tip (Figure 4.8 I). Because the diameter of the upper end will be larger than the lower end, the pushing shoulder will be fixed there. Figure 4.8 J shows the finished microgripper compared with a human hair. The performance of the gripper will be discussed in the following section.

A) Tungsten rod bent for electrolyte etching.

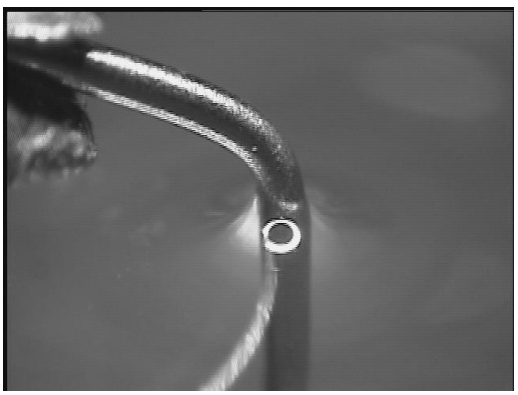

B) Etch tungsten rod to a certain diameter.

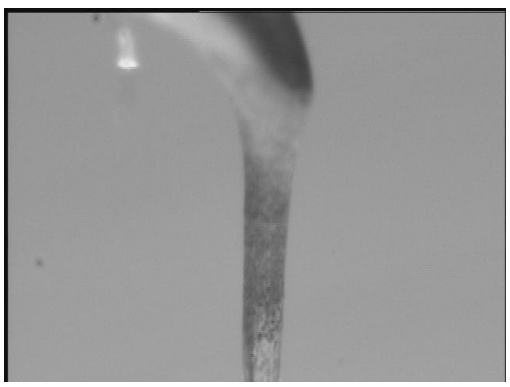

C) Etched tungsten tip covered with WO_3 probably [138].

D) Etch off the extra length.

E) Tungsten tip after electrolyte etching.

F) Grind against sandpaper.

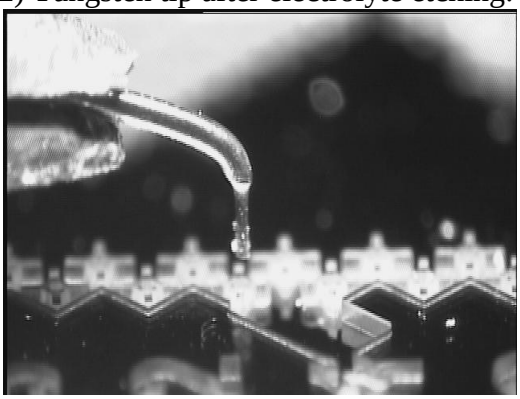

G) Measure the diameter of the gripper with sizer.

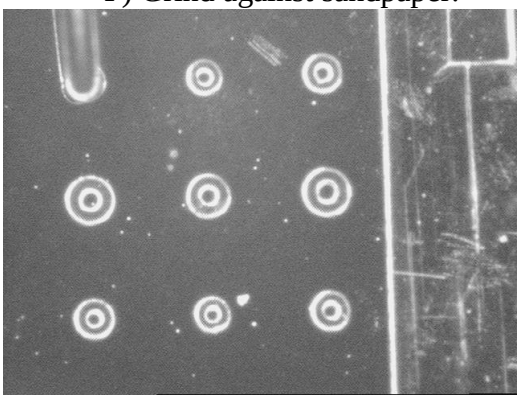

H) Put on pushing shoulder (top view).

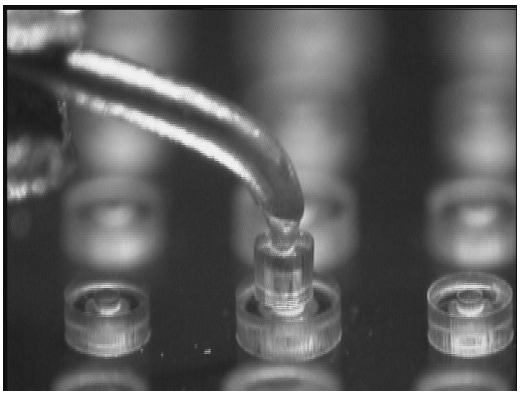

I) Fix the pushing shoulder on tungsten tip by pushing against a larger girdle.

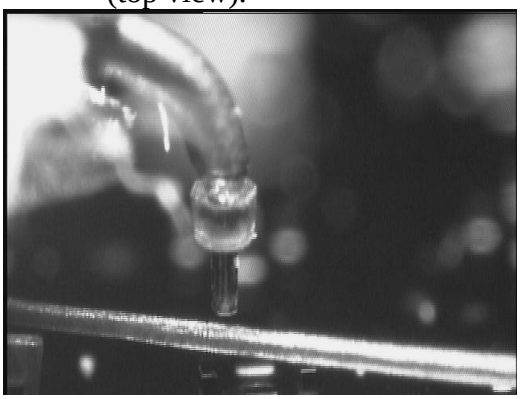

J) Finished microgripper compared with a human hair.

Figure 4.8: Microgripper fabrication steps.

4.3 Design and Fabrication of Releasing Structure

As discussed in the above, a major advantage of the L-shape passive microgripper is the simple structure and the relatively low cost. But on the other hand, because there is no actuator with this gripper, it can not release a micropart actively. For

unqualified micropart, for instance, a micropart misses one branch due to the bulbs during the spin coating process; there must be an active releasing strategy to remove it from the gripper.

To release the unqualified micropart actively, a releasing structure was designed and fabricated. The releasing structure was a half-circle-shape notch machined on a small metal plate. The dimension of the notch must be big enough for the micro-gripper tip with pushing shoulder to go through, while small enough to block the microparts. The diameter of the half circle was designed to be $300\mu m$. The height of the releasing structure should be of the same order as the scaffold to prevent collision during the assembly process.

The notch was machined by electrical discharge machining (EDM) technique. The main body of the releasing structure was also made of tungsten. A tungsten rod, $1.2mm$ in diameter, was grinded on both sides to form a thin plate at one end. EDM was then used to cut a straight line at the end and cut in to form a half-circle-shape notch. After fixing the tungsten rod to a square magnetic plate, the releasing structure was completed.

The releasing process was shown in Figure 4.9. The micropart adhered to the releasing structure after drawing up the microgripper due to the static electricity produced. During the automated assembly process, after releasing a micropart, the microgripper was programmed to go down again to remove the micropart from the releasing structure. Although a micropart stuck to the releasing structure will not disturb the next releasing action, it will influence the alignment of the releasing structure through machine vision.

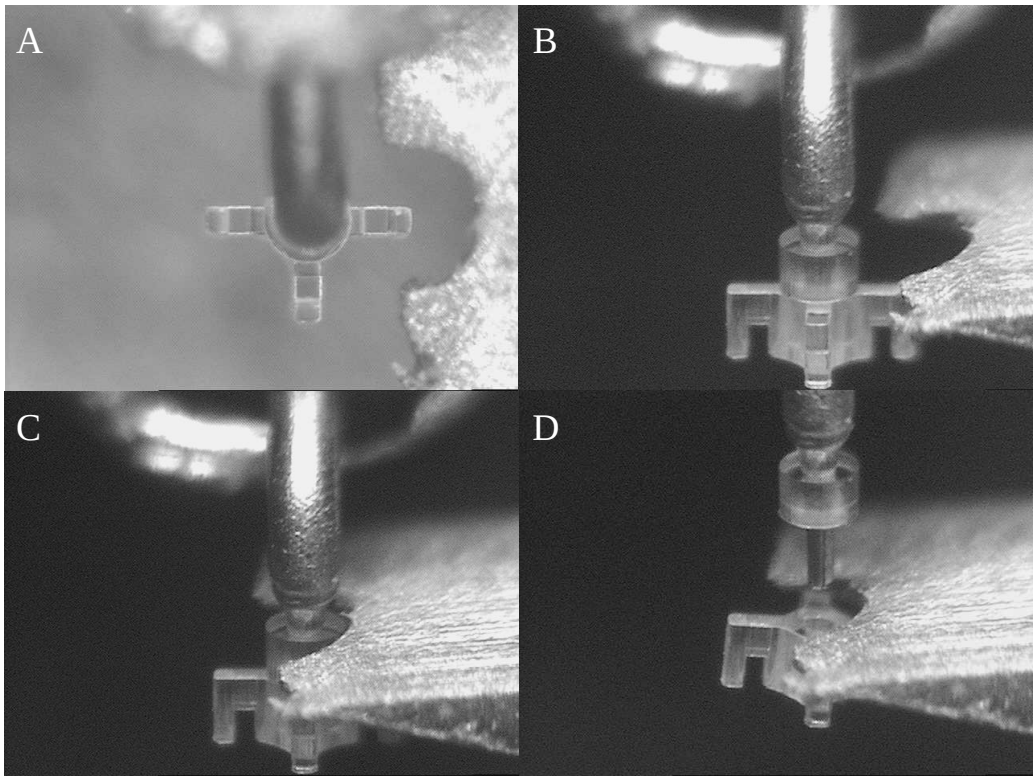

Figure 4.9: Process of releasing a micropart. (A) Top-view of the releasing structure. (B) Align the gripper with the releasing structure. (C) Move the half-circle notch above the micropart. (D) Retract gripper to remove the micropart.

4.4 Discussion

This chapter presented a novel microgripper designed for handling the microparts which will be used to build tissue engineering scaffolds. The L-shape microgripper had a more compact size compared with the two-finger shape-memory-alloy gripper previously used and it will not occlude the microscopic building blocks from top view. The simple structure of this microgripper made it low cost and easy to exchange. With a pushing shoulder mounted on a tungsten tip, the microgripper can apply an evenly distributed force on the top surface of the micropart so as to facilitate the automated inserting process. The "grasping" action was achieved by inserting the tungsten tip into the hole of the micropart so that the relative position

between the microparts and the manipulator is fixed which makes the automated alignment based on visual information simple.

As no actuator is involved with this gripper, successful grasping and releasing depend on friction. And because the friction involved in the microassembly process is hard to control, the pick-up and release success rates are relatively low, and for unsuccessful assembly, the unqualified micropart must be disposed off, which can be automated, but slows the process. Another limitation is the accuracy of the diameter of the tungsten tip. Lack of proper measurement prevented sub-micron accuracy with is highly desired for friction control.

Chapter 5

Closed-loop Force Control

5.1 Introduction

Force control has been used in mainly three applications in the micro world: to control grasp, impact or in assembly or insertion control. To date, most of the research on force control in the microworld has been performed for grasping [11, 36, 123, 139, 140], which is crucial for micro-manipulation but not necessary in microassembly. To grasp bio objects or optical fibers, a force sensor mounted on the gripper fingers prevents damage and enables reliable picking up.

Impact force control is essentially done via approaching velocity control. Impact force is almost solely determined by the mass of the collision objects and the relative velocity, because other factors such as stiffness, elasticity and viscosity of the part are invariant for a certain task. Yang and Nelson successfully controlled the impact force by reducing approaching velocity using a proximity sensor [15] that is able to estimate position where the optical microscope may not be able to because of the limited depth-of-view.

Insertion force control is necessary to successfully accomplish a peg-into-hole task without damaging the microparts. One difficulty for insertion control is the embedding of force sensors between the arm and the gripper. Micro assembly intrinsically demands a high positioning accuracy, which requires precise stages and high stiffness of the connections, i.e. adapters, arms and joints. While high resolution force sensors normally have a delicate and fragile elastic element, embedding such an element into the gripper will largely reduce the system positioning accuracy and robustness. Designing a force sensor with both high stiffness and high resolution is still a challenge and thus most of insertion tasks were done in a tele-operated fashion based on visual feedback [9, 12, 87, 58].

We have previously developed insertion force control by using a flexure stage [141]. Because the flexure stage was friction free in its moving direction, it was ideal for explicit force control. However the flexure stage had an intrinsic problem. To make it frictionless, the motion part of the stage was supported by 4 spring structures, which made the natural frequency of the stage very low and caused large variations during conveying and insertion. Therefore the whole system could only work at very low speed and in turn resulted in low efficiency.

To increase the assembly throughput, a new force sensor and admittance control laws were implemented in this project. These were used on off-the-shelf commercial stages. The new design also enabled the system to analyze the insertion status based on both position and force information, thus enabling realignment based on force feedback when visually controlled alignment failed. The force sensor was designed to have a cantilever beam structure with the gripper

fixed at the free end and an elaborately designed elastic element at the supporting end. The cantilever beam worked as a mechanical amplifier to produce a relatively large moment at the supporting end when a force was loaded at the free end. Deformation of the elastic element was measured by a strain gauge glued to the surface of the elastic element. The measurement range of the force sensor was about 500*mN*, with a resolution of 3*mN*, which was just suitable for the application in this project.

Admittance control was implemented in this project [142]. The idea of admittance control is that when the manipulator gets in contact with the environment, the force sensor will report the force value to the controller, and based on this force value new position, velocity or maybe acceleration command will be sent to the actuator. The manipulator is given a behavior of desired admittance by modifying position commands based on force feedback. Since there is no need to model the environment, which is difficult to carry out in most cases, implementation of admittance control becomes very simple.

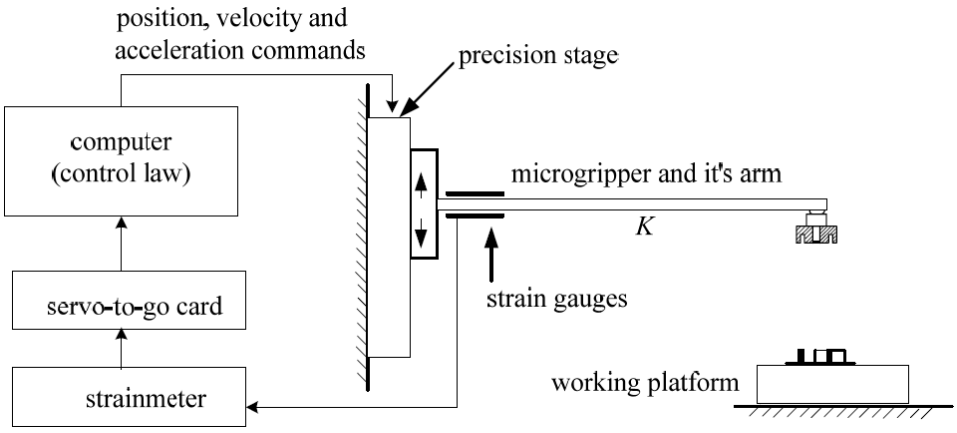

Figure 5.1: Implementation of admittance force control with our setup.

The working principle of the force control system is illustrated in Figure 5.1. A gripper fixed on the arm was carried by the *Z* stage to move up and down to realize insertion and retraction. The arm was a cantilever beam, which will sustain the force when the free end of the cantilever made contact with the environment. Contact force control was accomplished by adjusting the *Z* stage position based on the strainmeter reading.

The value of the gripper arm stiffness *K* was crucial for the performance of the admittance control system. If *K* was too large, i.e. the arm was very rigid, the force will be sustained by the deformation of the micropart, and if the micropart was brittle, the contact force will increase dramatically after contact, which may damage the micropart or the gripper. On the other hand, if *K* was too small, i.e. the arm was very flexible, the position information will be less reliable for perceiving inserting status and may even cause vibration. The stiffness of the arm was computed from the working distance and the resolution of the position encoder of the *Z* stage. The design of force sensor was coupled with the design of *K*, as will be further discussed in the following sections.

Both picking up and assembling of a micropart can be interpreted as a peg-into-hole problem. The combination of the position and force information will tell whether the peg has been inserted into the hole properly so as to realize "blind" realignment, i.e. based on force information solely. Two strategies can be taken to combine the two kinds of information:

1. Pushing down by a certain distance and checking out the force;
2. Applying a certain force and checking out the position.

In this project, the latter one was adopted because it will also help in protecting the part from damage by large contact forces. The details will be further discussed.

5.2 Force Sensor Design

The forces in microassembly are in the range of hundreds of *mN*, which demand a very flexible elastic element. However large flexibility would deteriorate the positional precision, which is crucial in microassembly. The design of the force sensor for microassembly is thus a tradeoff between sensitivity and rigidity.

In this project, we used an elastic element that will deflect under load with two semiconductor strain gauges attached to the surface. One end of the elastic element will be fixed onto the *Z* stage (the vertical stage) and a gripper clamper will be fixed to the other end to form a cantilever beam structure. The main body of the sensor is shown in Figure 5.2. Force was loaded on the free end of the cantilever and strain gauges will be glued to the support end where the strain is maximal.

To simplify the problem, in the following analysis, the microgripper with its clamper was simplified as a rigid cantilever beam with a concentrated force loaded at the free end of the beam. The elastic element has a rectangular cross section.

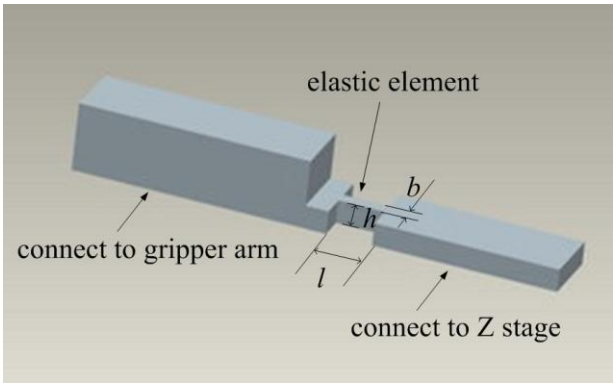

Figure 5.2: Force sensor body designed

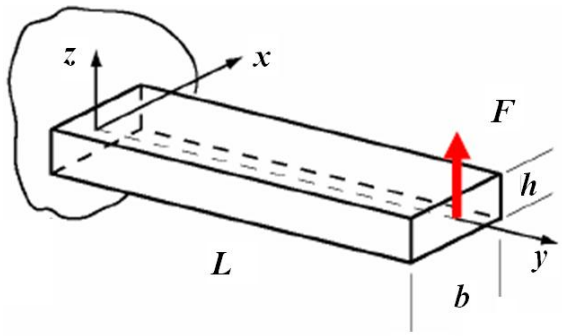

Figure 5.3: Cantilever deformation.

The two most important values to consider are: the strain measured by strain gauges, which represents the sensitivity of the force sensor, and the deflection of the free end under load, which represents its stiffness. The design criterion is that the strain should be large enough, $\varepsilon \geq 30\mu$, to guarantee an acceptable resolution, and the deflection should be sufficiently small, $\delta \leq 100\mu m$, to assure stiffness.

Figure 5.3 shows a cantilever beam under load. The maximum bending moment, at the support end of the cantilever, is given by

$$M = FL, \tag{5.1}$$

where F is the loading force from the microgripper and L the length of the cantilever. According to theories of mechanics of materials, the strain is given by

$$\varepsilon = \frac{6FL}{Eh^2b} \tag{5.2}$$

where E, the elastic modulus, indicates the stiffness of material within the elastic range. And the deflection of the free end is given by

$$\delta = \frac{12FlL}{Ebh^3}. \tag{5.3}$$

Comparing Equations (5.2) and (5.3), l affects stiffness only. We first set $l = 3mm$, considering the length of the strain gauge and fabrication process. F should be less than $1N$ based on experiment. L should be larger than $70mm$ to enable us to use a microscope placed above the working platform for control. For aluminum, $E = 73.1GPa$. A relatively larger h and smaller b will increase the stiffness without compromising the sensitivity. The value of b should be selected as small as possible. While considering the strength and area for gluing strain gauges, it was set that $b = 3mm$ and then h was determined from the above equations as $h = 6mm$.

Two bar-shape semiconductor strain gauges (Model SS-027-013-500P, Micron Instruments, USA - overall length: 6:858mm, width: 0:2286mm, gauge factor: 155 ±10, operating strain: ±2000μ) were attached to the top and bottom surfaces of the elastic element. Signal processing was accomplished by a TML's one-channel dynamic strainmeter: DC-92D, which provided the functions of forming a half Wheatstone bridge, auto-balancing, signal filter and signal amplifier. The finished sensing module is shown in Figure 5.4.

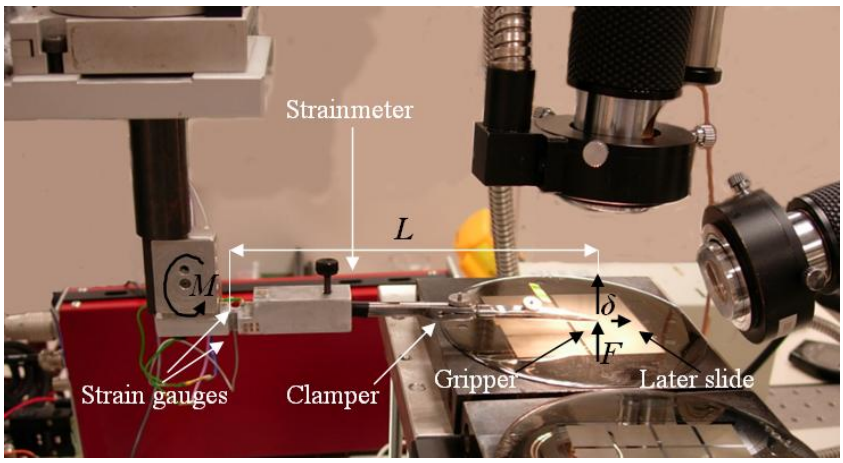

Figure 5.4: Close-up view of the force sensor, gripper and its clamper.

5.3 Force Sensor Calibration

Calibration of a force sensor usually consists of establishing the relationship between the output signal and the loading force. For this project, two more relationships will also be used: the relationship between force load and deflection of the end tip will be used to examine the status of inserting process based on position encoder reading and force sensor reading, and the relationship between force load and lateral slide of the end tip helps compensates for alignment error in the *Y* direction during insertion.

a. Output signal and force load relationship

Calibration was performed as follows: First the force sensor, clamper and gripper are mounted on the *Z* stage. A digital balance with total measurement range of $200g$ and accuracy of $0.01g$ was mounted on the *V* stage under the gripper tip. The stage is moved down in 5-micron steps and the gripper will push against the digital balance. The digital balance gave the value of force load, and for each step the output of the strainmeter is plotted against the force load. After the force reaching about $500mN$, the *Z* stage moves backward with the same step size, and the data is also recorded.

Through a least-square fit with a straight line, the sensitivity of the force sensor was estimated to be $15.8mV / mN$. Figure 5.5 showed the good linearity of the force sensor.

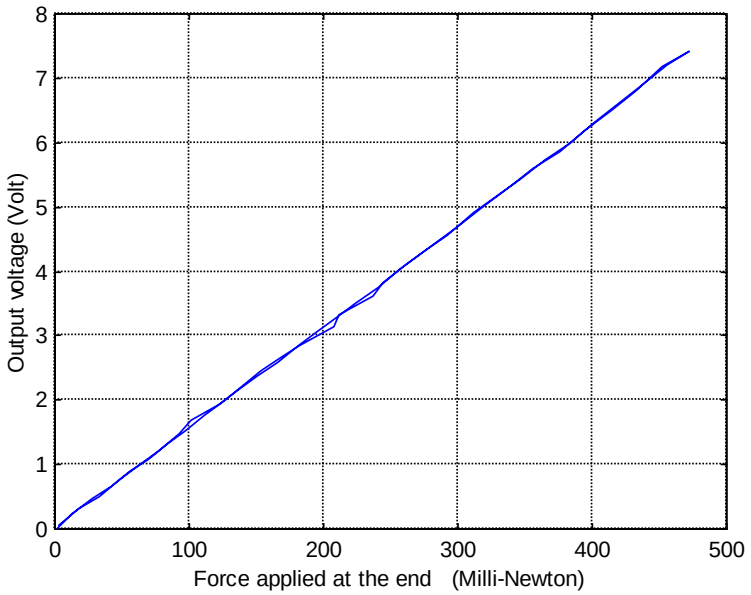

Figure 5.5: Calibration result: force load and output voltage relationship.

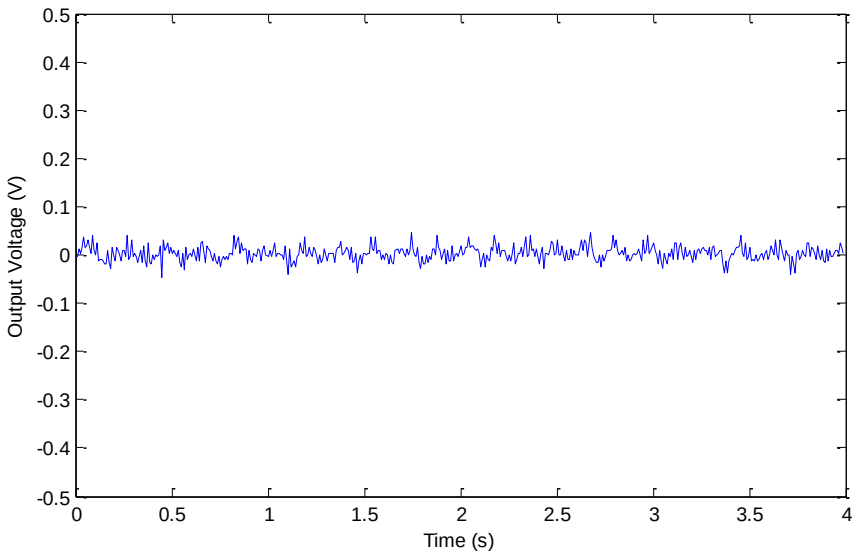

Figure 5.6: Sensor noise in idle state.

Since the output of the sensor is analog, its resolution strongly depends on the noise level of the strainmeter and the data acquisition card (DAQ). The output of the strainmeter in the idle state of the force sensor is shown in Figure 5.6 .The

maximum deviation of the output voltage from the sensor is about $0.05V$, which accounts for a force sensor resolution of around $3mN$.

b. End tip deflection and force load relationship

As discussed above, the position information and the force information will be combined to infer how the insertion is progressing. The encoder of the *Z* stage can give the position of the supporting end of the arm, and when the deflection of the gripper tip is known, the exact position of the gripper tip will be determined, from which we will then know whether the part has been inserted or not.

The calibration process is similar to the above process; however this time the digital balance is replaced by a piece of iron. Because the surface of the iron is so hard that no deformation is observed under microscope when pushed against by gripper tip, the encoder reading of the *Z* stage is the deflection of the end when loaded. For each motion step of the *Z* stage, the encoder reading and the output voltage of the strainmeter are recorded. The whole calibration process was programmed with visual C++ and performed automatically. Using the force-output relationship established before, the deflection and force relationship was obtained (Figure 5.7), and this deflection is consistent with the design.

c. Lateral sliding and force load relationship

When a force was applied to the gripper tip, the gripper tip will move a little bit along the *Y* direction (Figure 5.8). This motion is caused by the deformation of the fixtures. Although the motion distance is of the order of microns, it will negatively affect the insertion. To compensate for this lateral sliding, the applied force and sliding distance relationship should be established first.

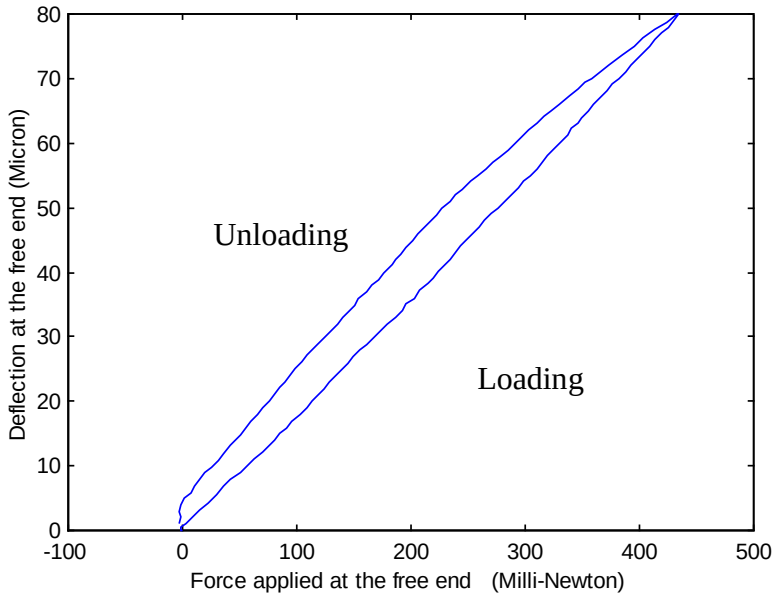

Figure 5.7: Calibration result: relationship between deflection and force loaded at the gripper tip.

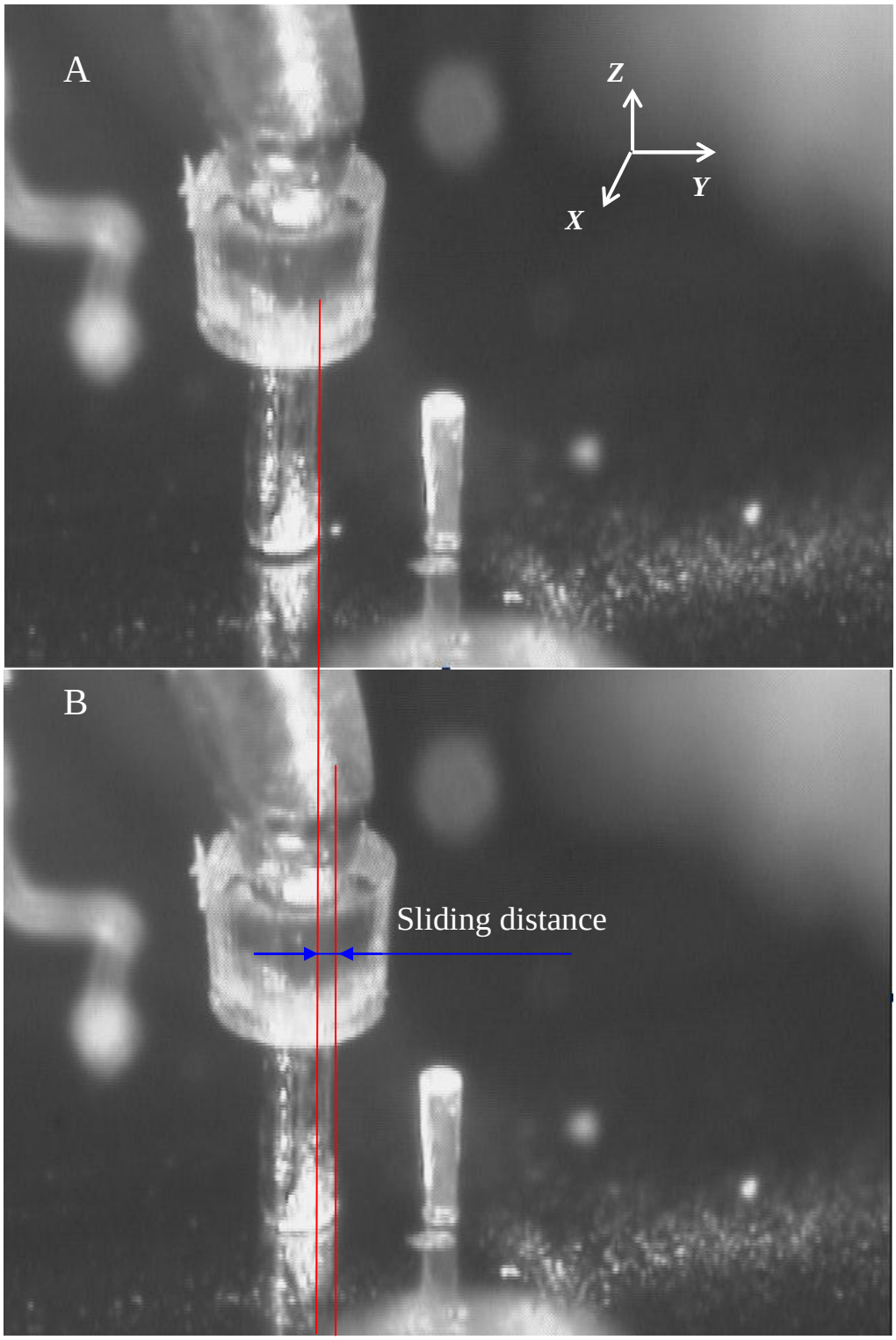

Figure 5.8: Gripper tip slide along *Y* direction as pushing force increased. (A) before the gripper tip was making contact with the wafer; (B) after the gripper pushing against the wafer.

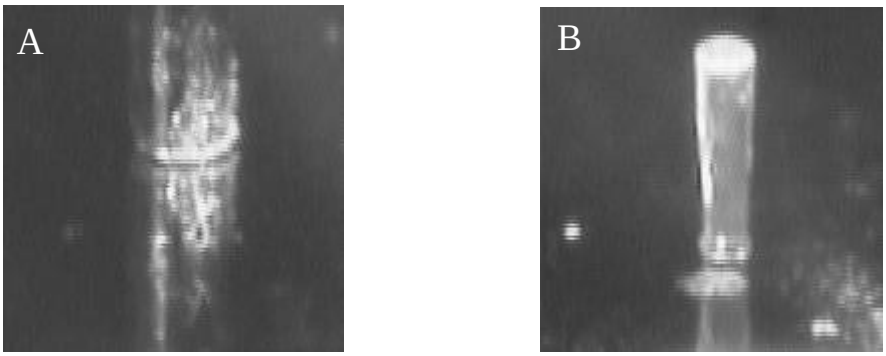

Figure 5.9: (A) Template of the gripper tip; (B) Template of a mark.

The sliding distance of the gripper tip will be measured by image processing, in particularly by pattern matching. Before the calibration, the relationship between the pixel distance (the distance in the image) and the real world distance should be obtained. This is also accomplished using pattern matching.

Figure 5.9 B shows the template of a SU8 mark fabricated on the wafer, which was then fixed on the *Y* stage. The position encoder of *Y* stage was first set to zero and the mark's position in the image was determined through pattern matching. Then the *Y* stage was commanded to move a certain distance and a new image was taken, the mark's position was estimated and recorded again. This was repeated two more times, and the resulting data is shown in Figure 5.10. The relationship between the pixel distance and the real world distance is then obtained, which is that each pixel represents 1.6μm in the real world.

The pattern matching algorithm used in the above process is the same as the one used to determine the gripper tip position. Because the template image is a sub-image of the source image, the estimated position can be very accurate (sub-pixel accuracy). The details of pattern matching will be presented in Chapter 6. The template of gripper tip is shown in Figure 5.9 A.

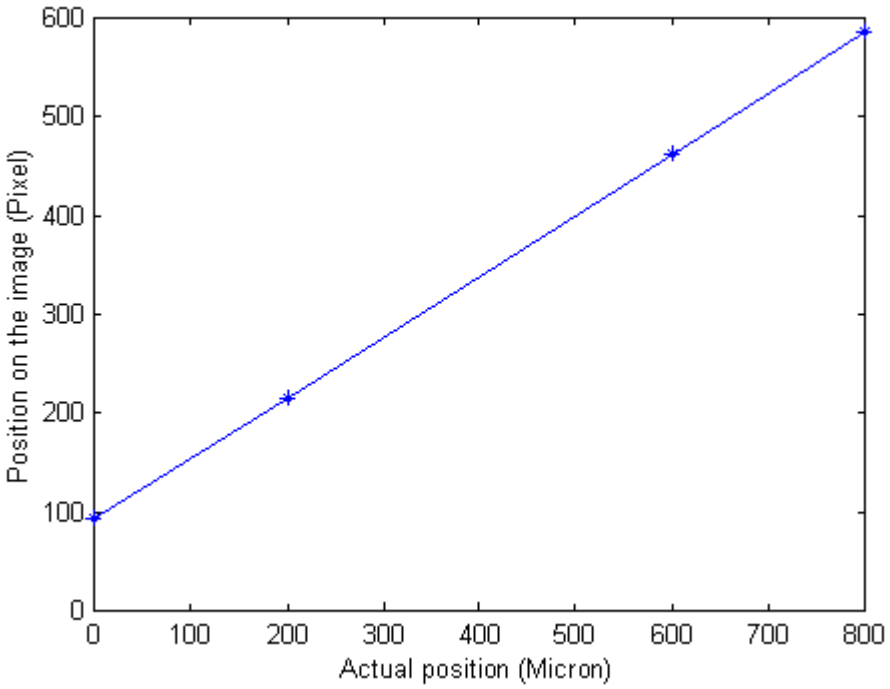

Figure 5.10: The relationship of the real world position given by encoder and pixel position in the image of a SU8 mark.

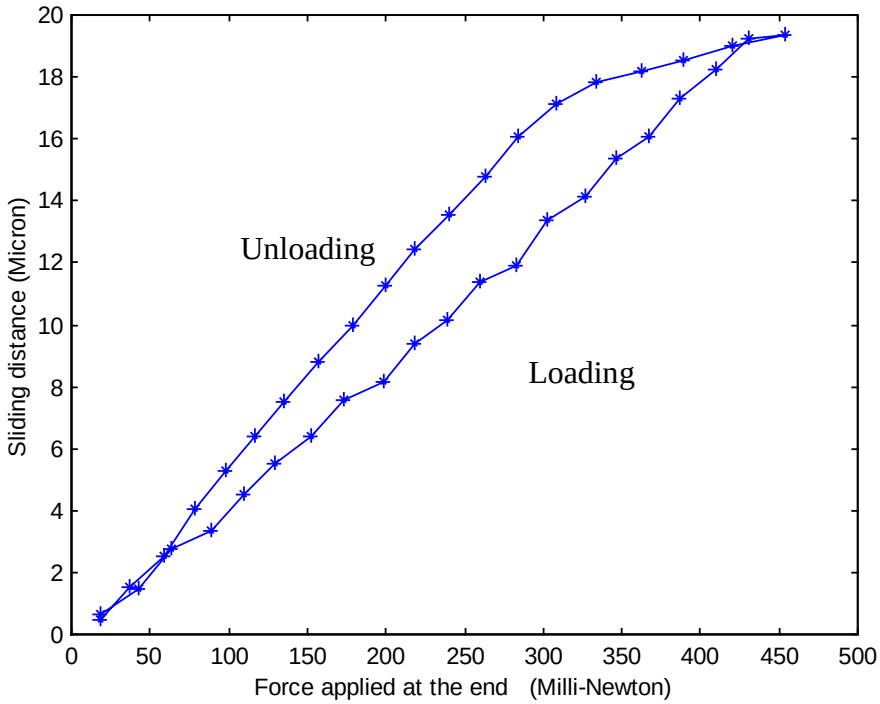

Figure 5.11: Calibration result: relationship between forces applied at the gripper tip and the lateral sliding distance of the gripper tip.

To measure the sliding distance, the loading force was also performed by moving the *Z* stage in steps as described in the calibration process above. After each step, both the pixel position of the gripper tip and output voltage of strainmeter were recorded. All the motion, image processing and recording processes were programmed and accomplished automatically. The real sliding distance was then calculated using pixel-real world distance relationship and the sliding distance was plot against force applied at the gripper tip (see Figure 5.11). Despite the hysteresis, the estimated sliding distance can achieve an accuracy of less than $5\mu m$. In the experiment, Figure 5.11 was used to reduce the alignment error.

d. Natural frequency of the force sensor and clamper

With a cantilever beam structure mounted on the *Z* stage is moving up and down, one of the most important issues is the vibration in the *Z* direction. If the natural frequency of arm is similar to the working frequency, it will affect the control tremendously.

The natural frequency was measured by attaching a human hair to the free end of the cantilever, and dragging the hair upwards until it broke. Then the arm will vibrate freely and the output voltage of the force sensor was recorded with an oscilloscope (see Figure 5.12). From the figure, we can see that from 0.05 to 0.1 seconds, there are totally 9 waves, so the first order natural frequency of the cantilever is about

$$F_n = 9/0.05 = 180Hz \quad (5.7)$$

The frequency of the motion command sent from host PC to stage controller is 66.67*Hz*, which is 3 times smaller than the natural frequency of the force sensor and the clamper. Actually, no resonance was observed in the experiment.

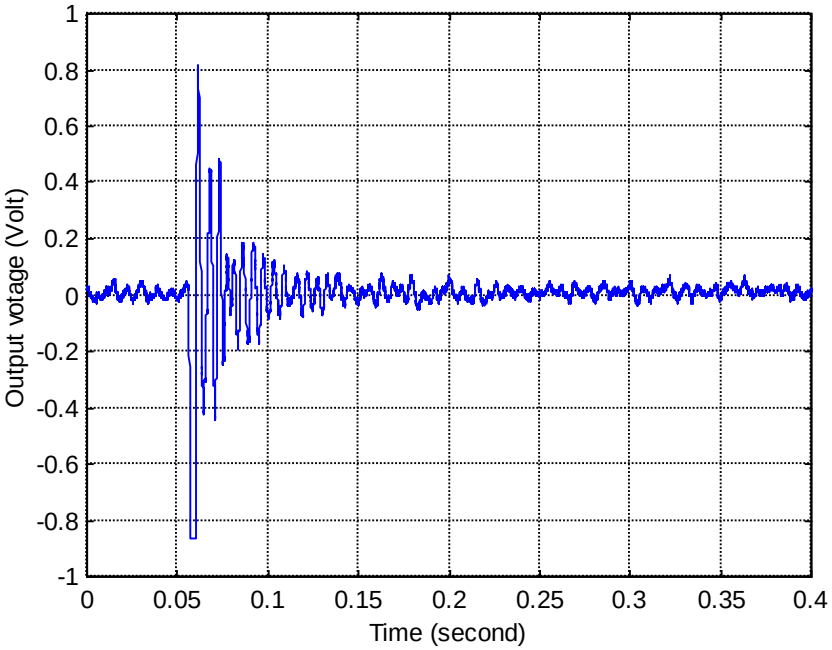

Figure 5.12: Strainmeter output of free vibrating arm.

5.4 Force Control Strategy

In this project, the actuator used for admittance force control is a precision stage. The maximum force output of the stage is about 80*N*, which is much larger than the environment force (in the range of hundreds of *mN*). Therefore, as seen from the environment, the actuator is very stiff, which enables good admittance control because the position of the actuator can be precisely controlled even with the presence of environment forces.

5.4.1 Assembly of a Micropart Process

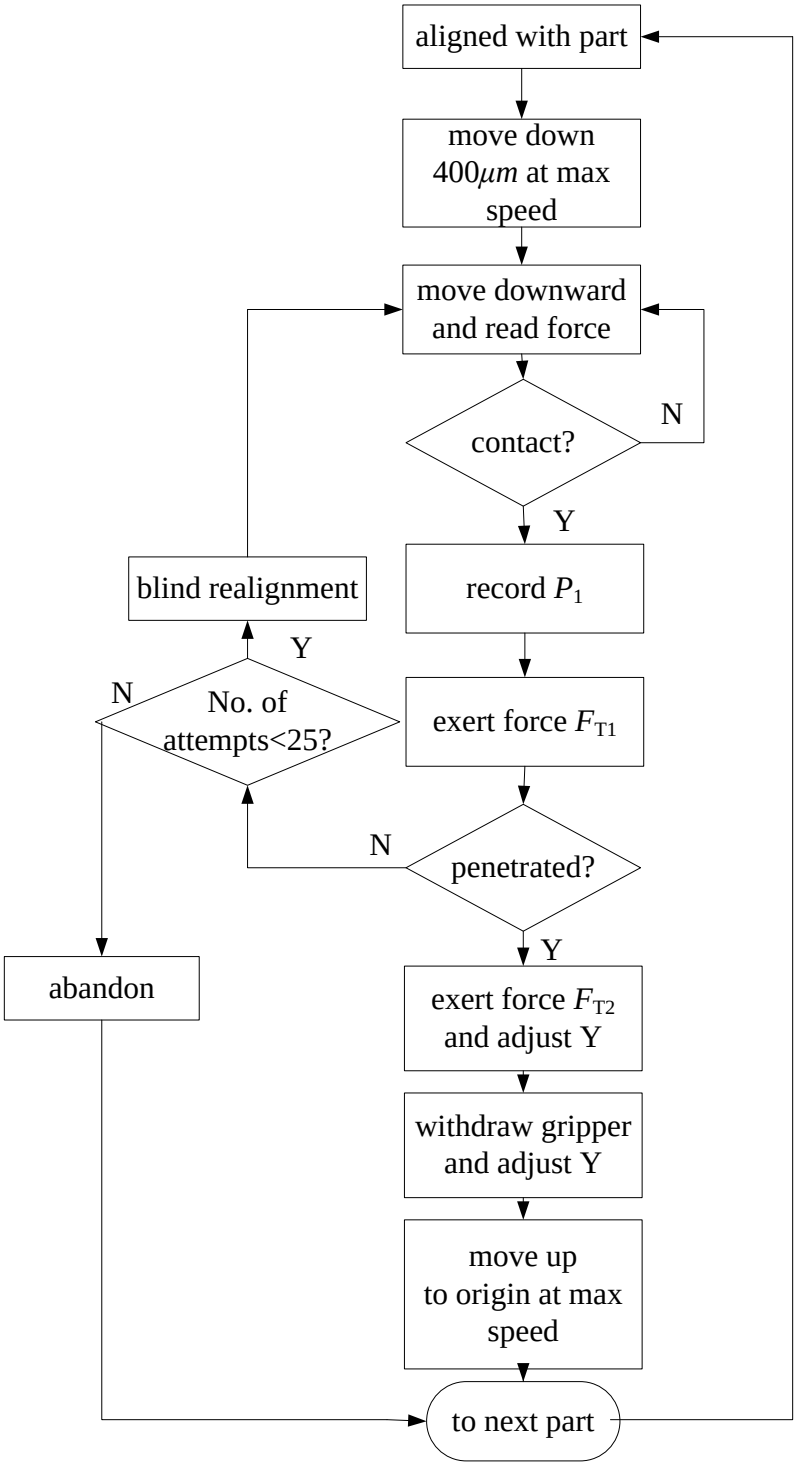

Figure 5.13: Flow chart of assembly a micropart onto the scaffold.

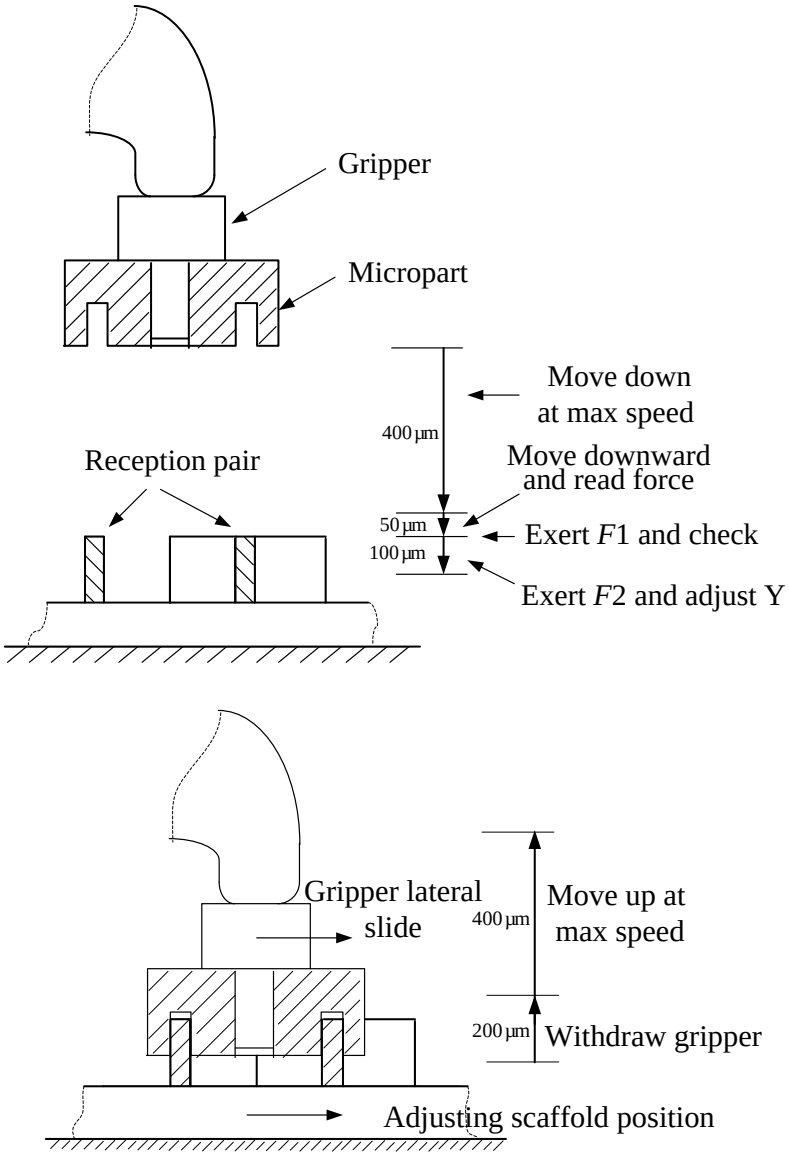

Figure 5.14: Illustration of assembly of a micropart.

Let us first describe the assembly process. Figure 5.13 shows the flow chart for the assembly of a micropart onto the scaffold and Figure 5.14 illustrates the assembly process.

The original position of the gripper was set to about 450μm above the top of the scaffold. After visually alignment, the gripper with the micropart will move down 400μm at the maximum velocity of 50mm/s. Then velocity was reduced to 200$\mu m/s$

and the host PC started reading the force values from the force sensor. When a strainmeter output larger than $0.1V$ (according to Figure 5.6, the noise is within $0.05V$) was observed, it is deemed that the micropart has made contact with the receptor.

After contact, the position of the Z stage, P_1, will be recorded for further usage and the mechanism will load a certain force, F_{T1} (the value of F_{T1} is carefully selected, see the following paragraph), on the micropart to try to assemble it. The moving down velocity of the stage will be reduced to

$$V = V_{safe}\left(1 + k_1 F_{votage}\right), \tag{5.4}$$

where $F_{voltage}$ is the strainmeter reading (the relationship between actual force and strainmeter reading is shown in Figure 5.5) and V_{safe} is maximum safe velocity during assembly which will be discussed in Appendix A. The value 1 was added to prevent a sudden change of velocity and k_1 was set to 1 in the experiment.

Figure 5.15 shows a typical force profile recorded when a part was pushed down at constant velocity after alignment. And Figure 5.16 illustrates the assembly process. When the Z stage moved about $450\mu m$, the bottom of the micropart just touched the top surface of a receptor (Figure 5.16 A). As the Z stage continued to move down, the force will increase at a rate similar to the case of pushing against a hard surface as shown in Figure 5.5. During this period from P_1 to P_2, (Figure 5.15) although the Z stage kept moving down, the part was stopped by receptor, because the width of the notch of the part is smaller than the thickness of the wall. Force increment was sustained by the bending of the cantilever structure: the elastic

element and the clamper (Figure 5.16 B). When the force reached a certain level, the part will be pushed down onto the receptor abruptly, and this was the penetration point, point *B*. The pushing force at this point was about 150*mN*. So, the value of F_{T1} was set to be 180*mN*. After that the force value will increase again as part is pushed down continuously.

Assembled?

To decide whether the micropart has been properly assembled, a position threshold, P_T, was selected based on Figure 5.15. If the *Z* stage passed P_T, it was deemed that the micropart had penetrated and will be pushed further. If not, the micropart will be realigned and the assembly tried again.

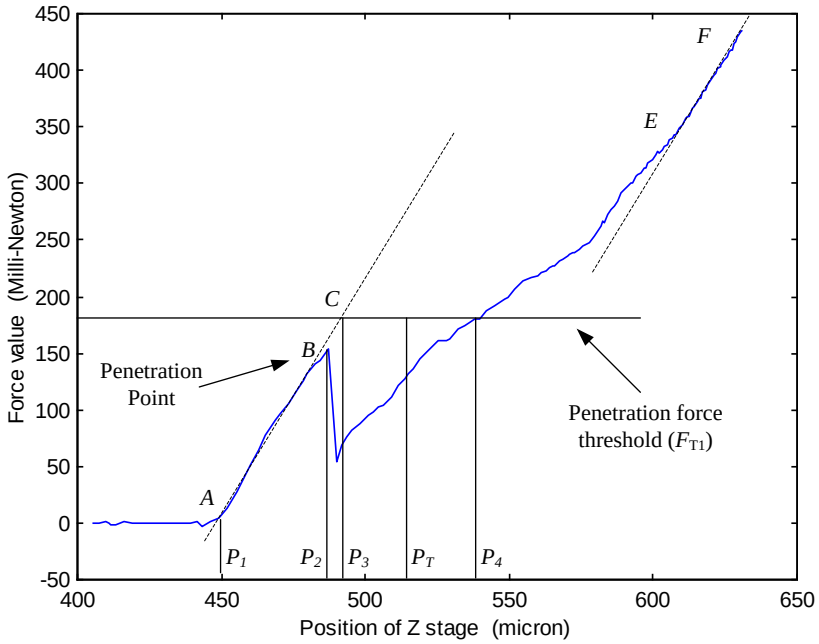

Figure 5.15: Typical force profile of insertion of a micropart into the scaffold at constant velocity. P_1: micropart making contact with scaffold, P_2: micropart penetrated into scaffold, P_3: where the *Z* stage will be when force reaching without penetration, P_T: position threshold (if the *Z* stage passed this point when force reaches F_{T1}, it means that the micropart has penetrated into the scaffold) P_4: actual position of the *Z* stage in case of penetration, *E*: fully inserted.

P_T was decided as follows. If there was no penetration, i.e. the part was not assembled properly, the encoder reading of the Z stage will be around P_3 (Figures 5.16 C and 5.15) when the force reached F_{T1}. If the part was properly assembled, the position of the Z stage will be around P_4 (Figures 5.16 D and 5.15). A position threshold P_T was selected between P_3 and P_4. If the position of the Z stage passed P_T when the force value reached F_{T1}, it was deemed that the part had penetrated

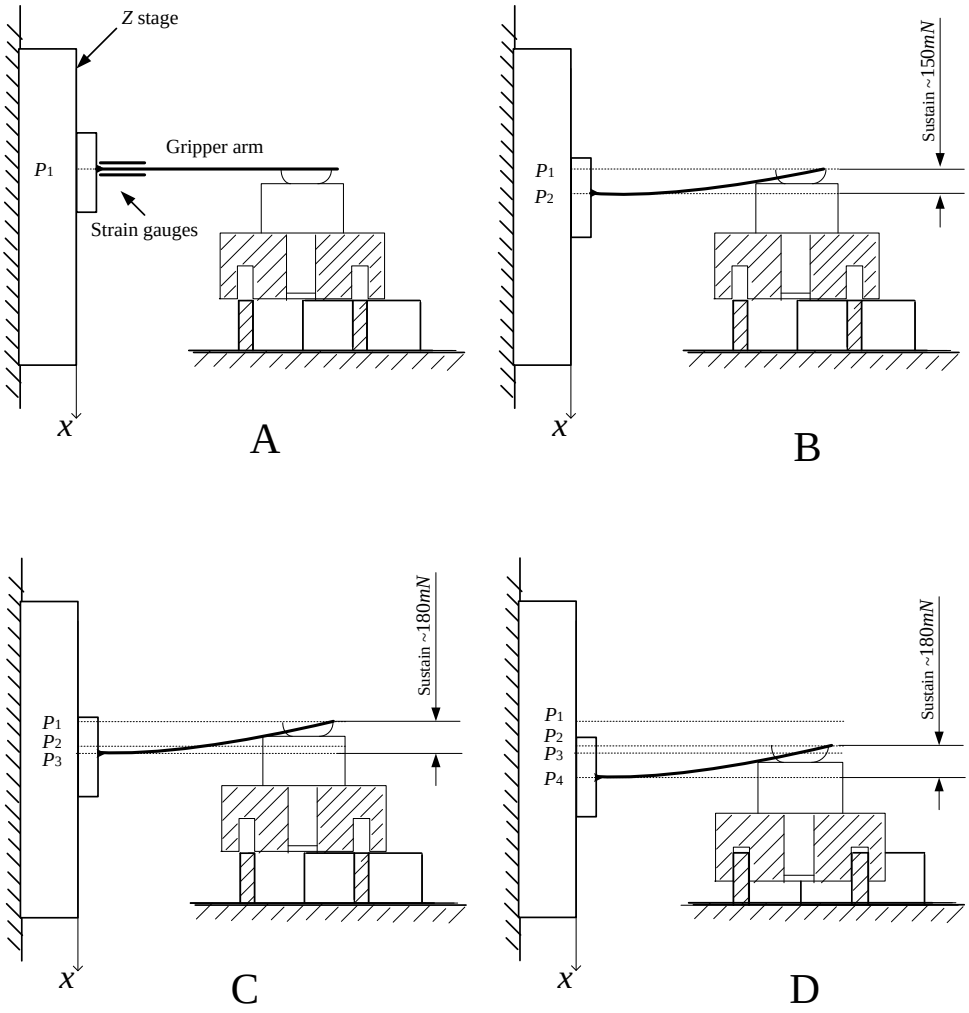

Figure 5.16: Illustration of insertion process. (A) The bottom of the micropart contacts the top surface of the receptor; (B) Just before penetration. Deflection caused by the increasing force is sustained by the deformation of the gripper arm; (C) The stage exerts F_{T1} on the micropart, if it does not penetrate into scaffold, the position of the Z stage will be around P_3; (D) If the micropart penetrate into scaffold under F_{T1}, the position of the Z stage will be around P_4.

into the scaffold. If not, the part was not inserted into the scaffold at all and was stopped at the surface, either because of misalignment or defection of the part.

The determination of P_T was crucial to the inserting process. If P_T was too close to P_4, there will be a larger possibility that a properly assembled part was assumed otherwise. If P_T was too close to P_3, non-assembled part may be assumed to be assembled properly.

In the automatic assembly process the penetration position threshold P_T was set as:

$$P_T = P_1 + 70\mu m, \tag{5.5}$$

where P_1 was the position of the Z stage when the part made contact with the scaffold. For different trials, P_1 may be a little bit different. Setting P_T in this way rather than using a certain value eliminated the negative influence of the uneven surface of the scaffold. The height of the top surface of the micropart will become less predicable as more layers are built on the scaffold.

It is worth mentioning that in Figure 5.15 point E was the fully assembled point. The slope AB was similar to slope EF and they were all similar to the slope of pushing against a hard surface (Figure 5.5). Point E indicated the full insertion point, i.e. part will not be able to move down further after this point. The pushing force for full insertion was about $350mN$.

For some micropart assembly process, the sudden force drop point B may be not as evident as shown in Figure 5.15, and in some cases there may be no peak at all. However this will not affect the performance of the assembly strategy: as long as

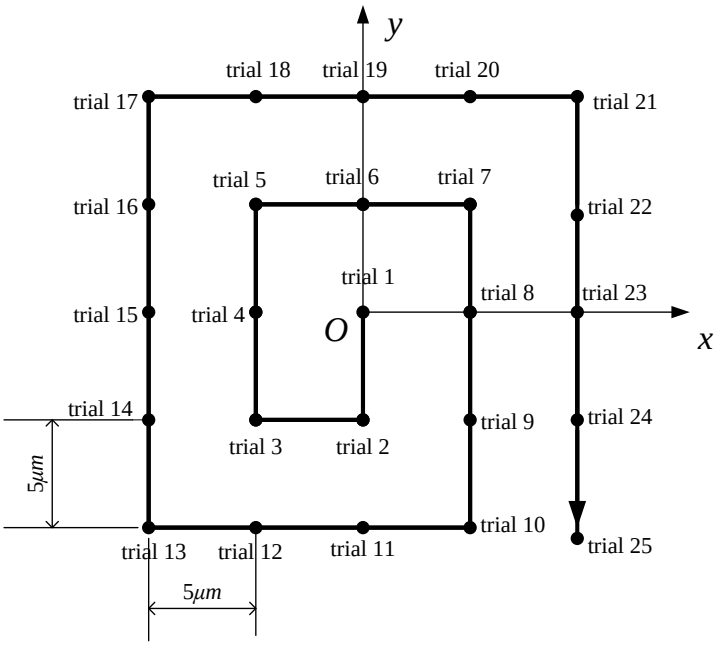

Figure 5.17: Blind realignment route.

the friction between the part and receptor was larger than the touching threshold, the assembly strategy will work.

Blind fine realignment

If the insertion was deemed as failed, the *Z* stage will withdraw 100μm and the part realigned. Realignment was not based on vision information, but by touching. The *XY* stage will move along the predetermined route (see Figure 5.17) and after each motion step, the part will be tried again for assembly. Because the alignment tolerance was about 5μm based on manual assembly experiment, the step size of the *XY* stage was set to 5μm.

Exert F_{T2} and adjust *Y*

If the insertion was deemed to have succeeded, the *Z* stage will move further down to exert an even larger force F_{T2} on the micropart to secure the micropart. F_{T2} was

the final force exerted on the part. As discussed before, when the force exerted on the tip of the gripper increases, the gripper will slide against the wafer (Figure 5.4). This also happens when the insertion force increases. Experiments show that when the slide is larger than 10 microns, it will cause the part to tilt.

Upon successful insertion, the position of the *Y* stage, P_{Y0}, will be recorded. And as the pushing force increased, the position of the base of the receptor will be adjusted by motion of *Y* stage according to the pushing force. And the target position of *Y* stage is

$$P_Y = P_{Y0} + 2.87F_{voltage}, \tag{5.6}$$

where $F_{voltage}$ is the reading of the strainmeter. The coefficient of $F_{voltage}$ was obtained from Figure 5.5. Both velocity and acceleration limits of *Y* stage were set to the maximum values in order to reduce time delay.

The *Z* stage will keep moving down at the velocity described by Equation 5.4 until the force reached F_{T2} to guarantee the part has been fully assembled. F_{T2} was set to be $450mN$. As shown in Figure 5.15 for full assembly, the force was around $350mN$, and so $450mN$ was enough for enforcing the proper assembly of the microparts.

Withdraw gripper and adjust *Y*

As the gripper was withdrawn, the force will drop and the gripper will slide in the reverse direction. During this period, adjusting of *Y* stage was still needed. The target position was also obtained from Equation 5.6.

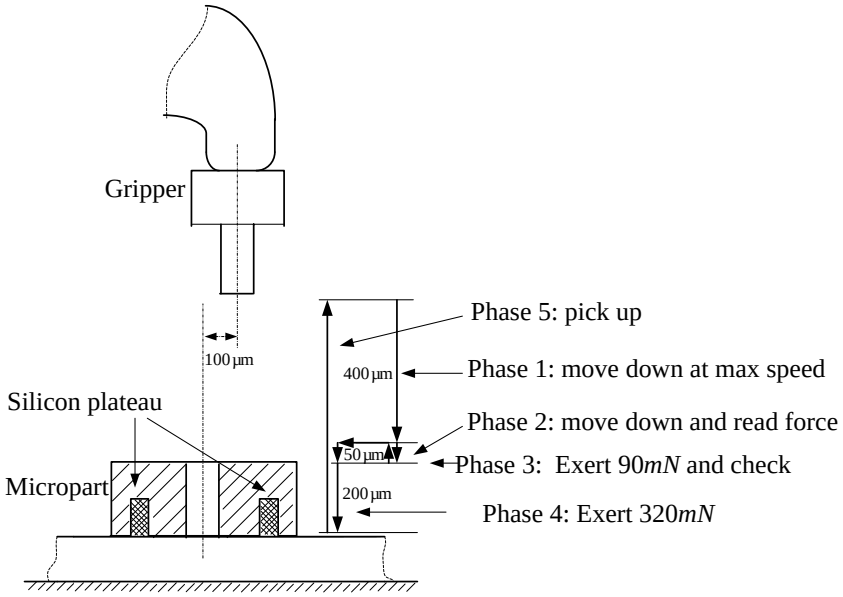

Figure 5.18: Illustration of picking up a micropart process.

A sudden force drop will cause a large and sudden sliding step. Although the maximum velocity of *Y* stage was up to 50*mm*/*s*, for a motion in the range of 10 microns, the velocity was quite low because it was controlled by a PID controller. To avoid the *Y* stage from failing to compensate for the sliding, the withdrawing velocity of the *Z* stage was set to 50*micron*/*s*, which was comparatively small.

After the gripper was retracted for 200μm, i.e. the tip of the gripper was clear of the part, the host PC will stop reading from the strainmeter and the *Z* stage will be set to its maximum velocity and go back to the original position.

5.4.2 Picking Up a Micropart Process

The pick-up process used a similar but simpler strategy (Figure 5.18). The major difference between assembly and pick-up processes was the way to determine contact position. In the pick-up process, if well aligned, there will be no obvious force increase even after the gripper tip has inserted into the hole of the micropart.

To detect the top surface position of the micropart, the gripper will be offset from the center of the hole by $100\mu m$. And then the gripper will move down until it touched the micropart. At the same time the position of the Z stage will be recorded as P_{Z0}. These are phases 1 and 2, which are essentially the same as the respective phases in the assembly process. Then the gripper will be withdrawn $60\mu m$ and move to the center of the micropart. Phase 3 was essentially the exerting of F_{T1} and penetration decided as described in the assembly process, except that the pushing force was reduced to $90mN$ to prevent breaking the brim of the hole. In similar way the position threshold is

$$P_{threshold} = P_{Z0} + 70\mu m \,. \tag{5.7}$$

The realignment strategy was the same as in the assembly process. In phase 4, the Z stage will keep moving down until the force reached $320mN$. This time, no adjusting of the Y stage was needed, because the lateral slide of the gripper will helped separate the micropart from the wafer. In phase 5, the Z stage will move back at its maximum velocity.

5.5 Experiment and Results

Experiment was carried out to test the effectiveness and efficiency of the picking up and assembly strategies. The first part of the experiment consisted of picking up a micropart automatically. The micropart was aligned automatically by visual servoing (details on visual servoing will be discussed in Chapter 6) and the automated picking up process begins. All the actions was programmed beforehand and executed under the control of a computer.

The image of picking up a micropart process is shown in Figure 5.19 and the force profile and motion of the *Z* stage are shown in Figure 5.20 and Figure 5.21, respectively. From these two figures we can see that this micropart was picked up after 5 trials and the total time used was about 15 seconds.

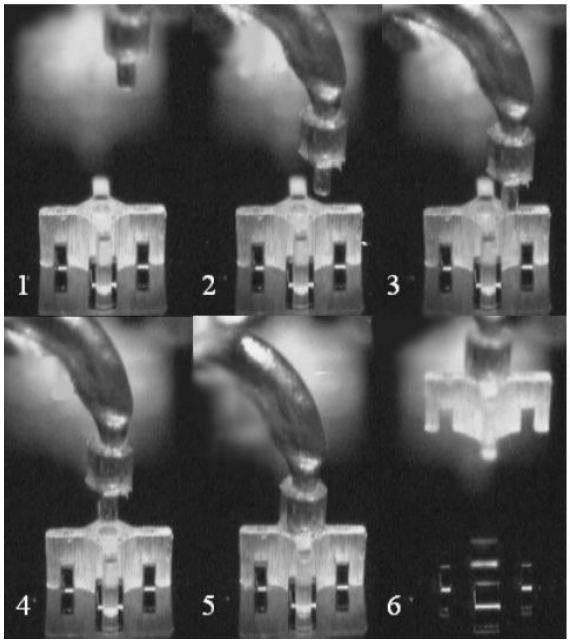

Figure 5.19: Image of automated process of picking up a micropart: 1. Gripper offsets 100μm; 2. Move down 400μm at max speed; 3. Touch the top surface of the micropart; 4. Go back 100μm to get aligned; 5. Exert force 320mN; 6. Move up as max speed and pick up the micropart.

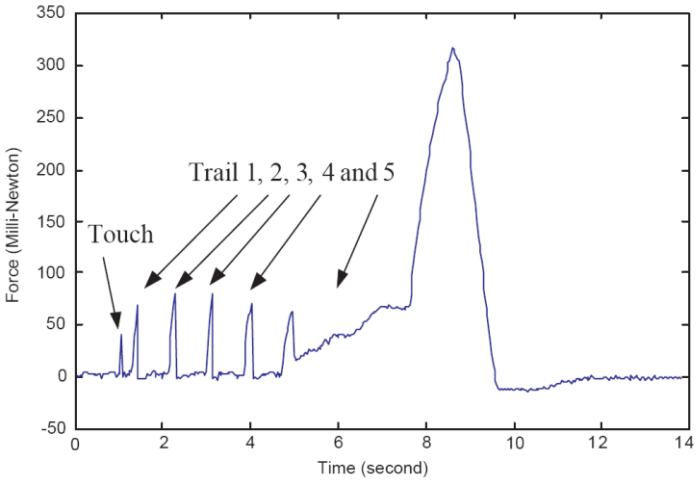

Figure 5.20: Force profile of an automated picking up process (this micropart was picked up after 5 trials).

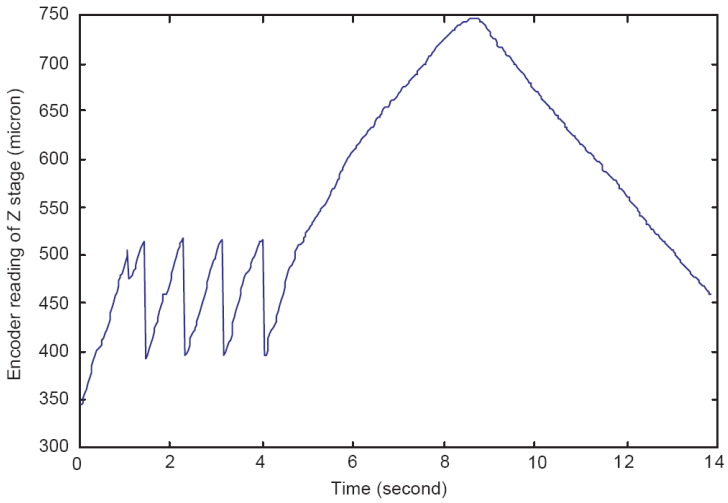

Figure 5.21: Motion of the *Z* stage during an automated picking up process.

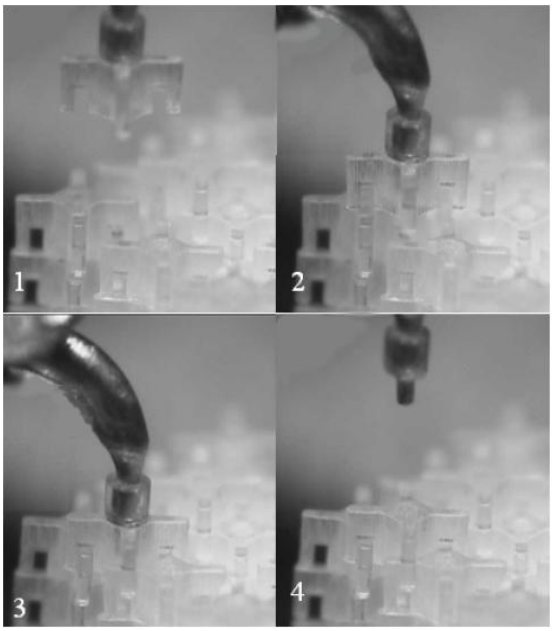

Figure 5.22: Image of automated assembly process: 1. Get aligned with the receptor; 2. Move down 400μm at max speed; 3. Exert force on the micropart; 4. Gripper move up, finished.

After picking up, the micropart was conveyed to the scaffold area and aligned with a receptor, also by visual servoing. And then, the automated assembly process was executed also under the command from the computer. The microscope image of the assembly process is shown in Figure 5.22 and the force profile and motion of

the *Z* stage are shown in Figure 5.23 and Figure 5.24 respectively. The whole process took about 15 seconds.

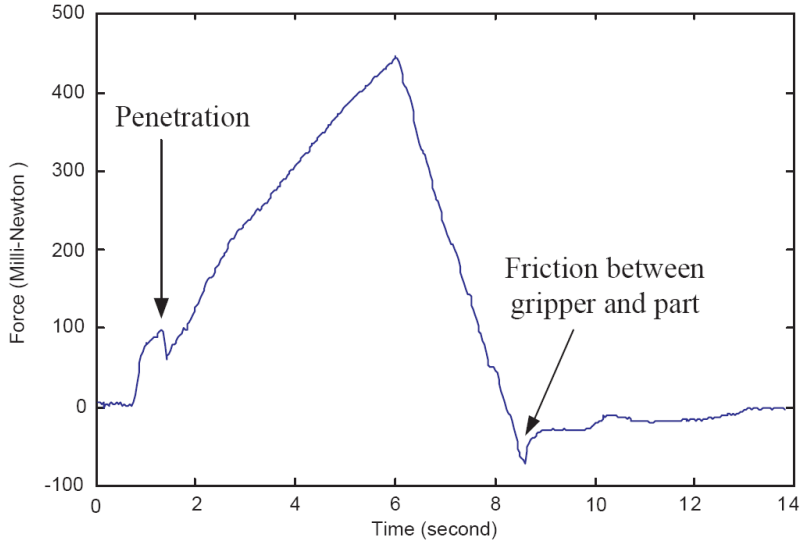

Figure 5.23: Force profile of an automated assembly process.

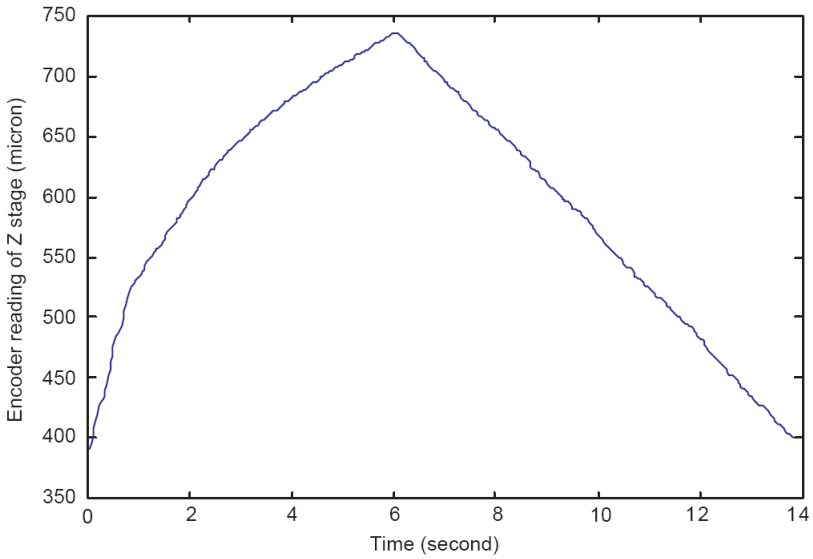

Figure 5.24: Motion of the *Z* stage during an automated assembly process.

Comparing with the flexure stage used previously [119], both the picking up and assembly time were largely reduced, and the system worked more stably and was safer for the micro components.

After assembly of dozens of microparts, it was observed that realignment occurred more frequently in the picking up process than in the assembly process. This may be caused by the following:

1. The image processing algorithm used in visual servoing is different for the two cases: pattern matching for alignment with a single micropart and Hough transform for alignment with receptor. Pattern matching is fast and simple for application but it is more sensitive to defects of the micropart, which may cause low positioning accuracy.
2. The picking up process is more sensitive to the alignment error than the assembly process. This is due to the smaller threshold force, F_{T1}, and the fact that the parts wafer is stiffer than the scaffold.

5.6 Conclusion

In this chapter, we presented the closed-loop force control in the picking up and assembly processes.

Because no off-the-shelf force sensor was found with specifications suitable for this project (they are either too delicate [157] or have a too long response time [158] to be implemented in this project), we designed and fabricate a force sensor dedicated for this assembly task. The main component of the force sensor was an elaborately designed elastic element that deformed under force load. The force value was obtained by measuring the deformation through two semiconductor stain gauges via a Wheatstone bridge circuit. The completed force sensor had a range of about $500mN$ and a resolution of $3mN$.

The calibration of the force sensor was carried out after it was embedded into the gripper arm. Calibration not only established the relationship between the output signal and the loading force, but also established the relationship between the force load and the deflection of the end tip, and the relationship between the force load and the lateral slide of the end tip. The latter two relationships were used to facilitate the automated picking up and assembly processes.

Admittance control was employed for controlling the forces in both picking up and assembly. In all the processes, intelligent strategies were developed to prevent damages to the micropart, compensate misalignment and guarantee firm assembly. A salient feature of the processes was the use of a combination of position and force information to infer the status of the insertion process. For improperly inserted situation, realignment will be carried out. Realignment was accomplished by a predefined process.

The effectiveness and efficiency of the force control system was demonstrated experimentally. Microparts can be picked up and assembled automatically even in the presence of misalignment. No micropart or scaffold damages were observed by using these pick-up and assembly strategies.

Chapter 6

Visual Servoing

6.1 Introduction

This chapter presents algorithms for aligning the gripper with a part and for aligning a part with a receptor before insertion. Because the alignment accuracy of $5\mu m$ demanded by the task is too small to be achieved by open loop control, vision information was introduced for closed-loop position control.

The use of artificial vision in closed-loop pose or position control is called visual servoing [143]. It has been extensively studied since the early 1980's due to its very large potential in improving flexibility and robustness for industrial robotic systems [144]. A taxonomy of visual servoing architectures has been proposed by Sanderson and Weiss [145] and Hutchinson [146]. The traditional visual servoing tasks were classified into two categories: image-based visual servoing (IBVS), and position-based visual servoing (PBVS). In IBVS, features are extracted directly from the image, and compared with a target image setpoint, thus generating an error signal. The error signal is used as input to the control law, which then drives the robot. In contrast, in PBVS, the actuators have an independent encoder-based

position control loop. Features extracted from the image are used to estimate position or orientation, which is then compared to a target Cartesian setpoint for generation of the error signal [147]. In this project, the PBVS was adopted and the system worked in a look-and-move fashion to circumvent high computation, system instability and a complex control.

Ideally, the techniques of visual servoing developed in the macro domain could be leveraged toward automation of microassembly tasks. However, there are significant differences in implementing vision feedback in the macro and micro domains. In the micro world, the need for high resolution demands the use of high numerical aperture lens systems, which results in a very small depth of field and a limited field of view. The depth of field of the optics normally used in micro assembly tasks today ranges from $0.2\mu m$ to $120\mu m$. The defocused object is quite blurred or sometimes even invisible.

In the macro world, 2D images can be used to reconstruct 3D configuration of the real object, while this is extremely difficult in the micro domain. Passive autofocus was developed [148], where the focal plane was determined by means of image power measure and coarse/fine turning, and no external means for measuring distance such as lasers or ultrasound was used. [23] utilized a proximity sensor to determine the position of the probe along optical axis and hence realized visual servo in the direction perpendicular to the image plane. In this project, the focusing problem was solved by mounting a V stage on the XY stage to keep the object of interest in the focal plane. The motion of the Z stage carrier is parallel to the optical axis of the microscope used in the visual servoing loop.

Another difficulty in using vision in micro assembly is the limited field of view which is also caused by the high magnification of the microscope system. Though microparts used in the microassembly task are very small, they will normally be conveyed over a long distance. [23] and [147] solve this problem by employing several cameras: one zoom-out camera provides image of the whole working platform to facilitate coarse alignment or during the conveying phase and a high magnification microscope is used for final fine alignment. In this project, the long conveying distances depended on the encoder of the precision positioning stage only. The parts were regularly arrayed on the wafer with accuracy of the order of tens of microns, and the accuracy of the stage was $0.1\mu m/50mm$ which was accurate enough to move the object into the field of view of the microscope. The supervisory unit had to calculate the position of the part and the assembly location. The field of view of the microscope was about $1.0\times0.7mm$ and after the objects were brought into the view, automated alignment will be carried out.

The rest of this chapter is structured as follows: Section 2 describes the whole control loop, while Section 3 presents the alignment strategy and the control law. The image processing will be discussed in Section 4.

6.2 Visual Servoing Control Loop Configuration

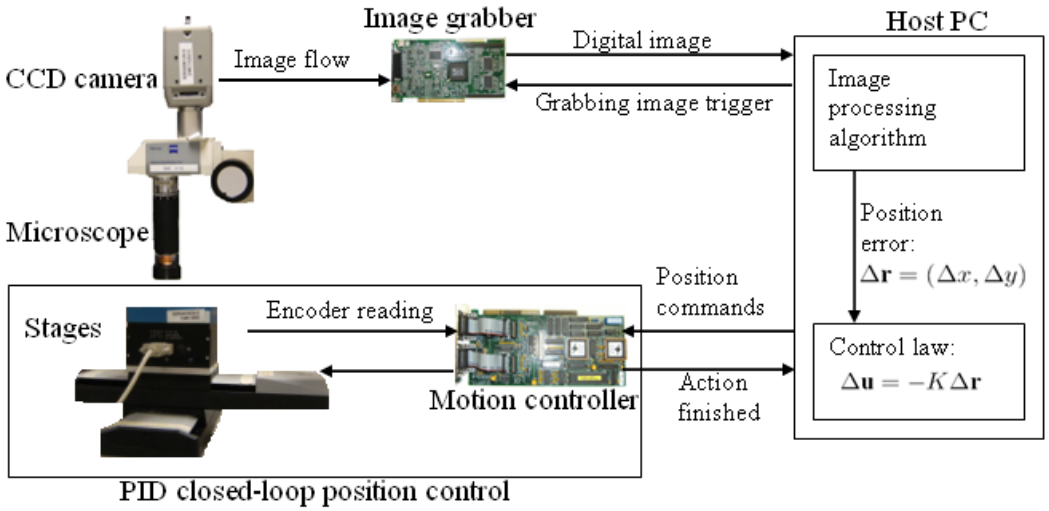

Figure 6.1: Vision control loop schematic.

Figure 6.1 shows the equipment for visual servoing: The top view was provided by a microscope (Model SEC-zoom4, ZEISS) with 8× magnification and a 1/3-inch CCD camera (Model SSC-DC10, Sony) mounted on it. This camera was connected to the Matrox Meteor II graphic board plugged in a Pentium III 400-MHz 512-MB RAM computer using Windows NT; two high-resolution translation stages (Model M-511.DD, Physik Instrumente (PI)) and a vertical micropositioning stage (Model M-501.1PD, PI) are controlled by the 32-bit digital controller (Model C-842, PI); the control software is coded in visual C++ for speed and portability. A user friendly graphical user interface (GUI) was realized.

The part wafer and the scaffold wafer were mounted on different platforms: the parts wafer was put on a height fixed platform and the scaffold wafer on a vertical stage, the *V* stage. Both platforms were mounted on the *XY* stages through an adaptor. When a layer of parts was completed on the scaffold, the *V* stage moved

down to keep the top layer in the focal plane. The optical axis of the microscope was adjusted to be perpendicular to the *XY* plane formed by the *XY* stages, and both the motion direction of the gripper and the *V* stage were parallel to the microscope.

This configuration reduced a 3D assembly task to a 2D alignment job. The motion of the gripper was realized by closed-loop force control using another translation stage, and the visual servo was only used to align the *XY* plane and so kept it in focus.

The key feature of this configuration was the use of the single top-view microscope for the alignment in both *X* and *Y* directions. Because the image plane was parallel to the assembly platform, i.e. to the *XY* plane, no complex Jacobian was needed to transform data from camera to world coordinates, which also simplified the control. Although another two microscopes, e.g. one from the front and one from the side, are in principle necessary to identify the geometric configuration in the 3D space, in our case it would pose a great challenge to use the side view, both for image process algorithm and control law.

This is illustrated in Figure 6.2, which compared a side-view image and a top-view image with the same magnification and illumination conditions. The material used for fabrication part, SU8, was almost transparent which caused a lot of diffusions and reflection and hence deteriorated the image. The limited depth of field blurred the defocused feature shown in Figure 6.2 A. All these factors made it difficult to reconstruct the edge, corner or vertex or to determine the pose or position of the object. In contrast, Figure 6.2 B needed only a simple 2D analysis as the features were much easier to locate.

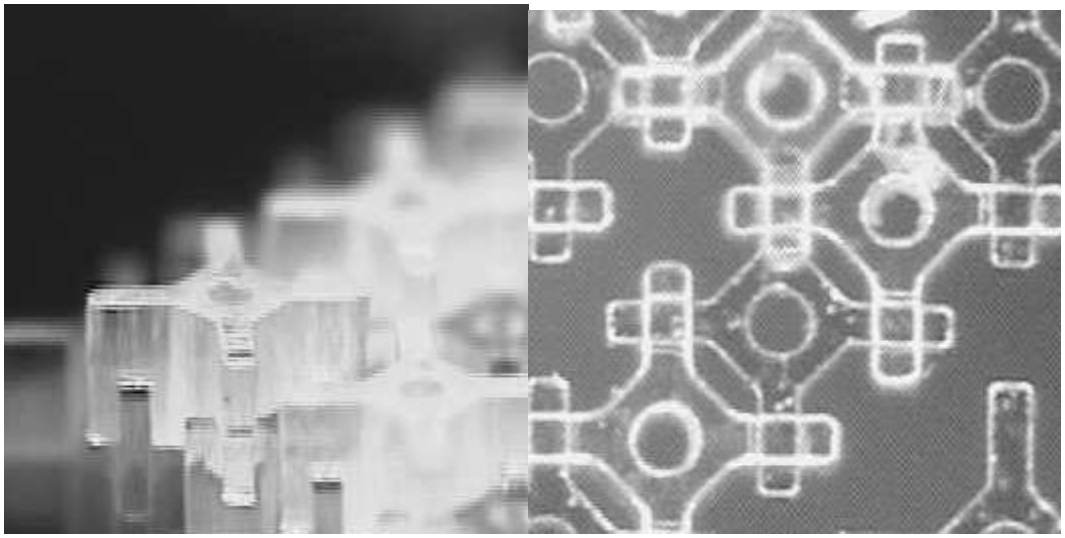

A B

Figure 6.2: Comparison of a side-view image (A) with a top view image (B) taken in the same magnification and illumination conditions.

6.3 Alignment Strategy

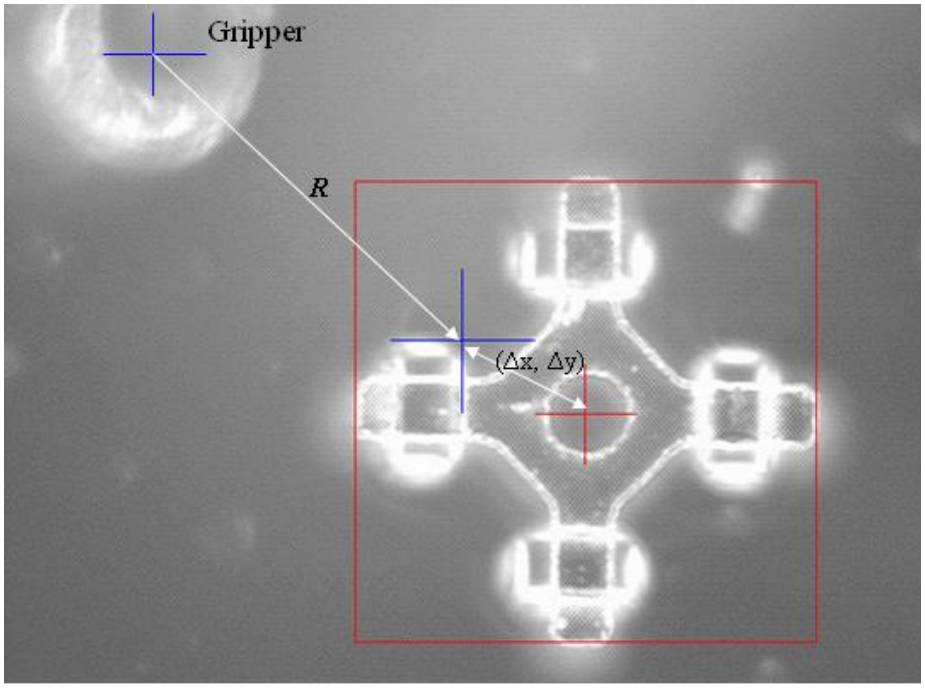

Figure 6.3: A typical top-view image for part alignment (before alignment).

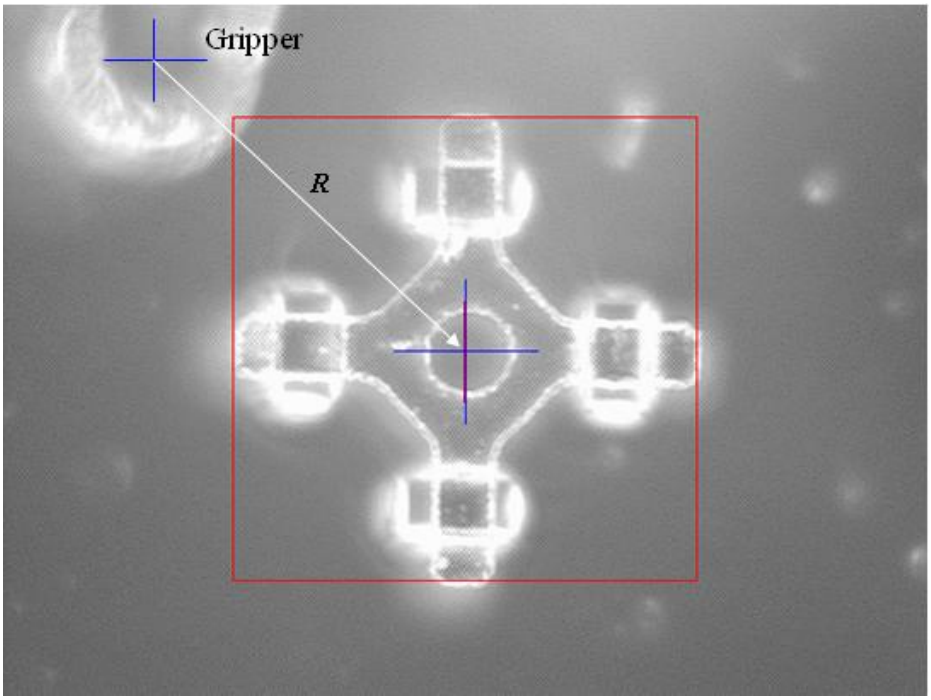

Figure 6.4: A typical top-view image for part alignment, after alignment.

In this project, fine alignment had to be performed in three operations: to match the gripper position with a part before picking it up; to align a part held by the gripper with the receptors at the scaffold area before assembling this part on them; and to align the gripper with the releasing structured before disposing of a defective part. The same alignment strategy was applied in these three cases, and so we detailed now the alignment process for the first case only.

Figure 6.3 shows a typical top-view image when aligning the gripper with a single part. Since the motion of the gripper was parallel to the optical axis of the microscope, the distance between the projection of the gripper and the center of lenses of the microscope on *XY* plane did not vary i.e.

$$\boldsymbol{R} = \text{constant}. \tag{6.1}$$

The exact value of ***R*** can be obtained through the calibration process. If we place the part precisely at the center of the image, shown in Figure 6.4, the gripper can be aligned with the part just by sending a command to the *XY* stage to move a distance of ***R***. The immediate objective of closed-loop position control is thus to move the part to the center of the image.

In the calibration process, first a home position was defined and the encoders of the *X* and *Y* stages were set to zero. The first part on the part wafer was then moved into the field of view of the top-view microscope manually. Then the 'defined first part' button was activated on the GUI, and the part was placed precisely at the center of the image automatically using the same control law as aligning a part. The readings of the encoders of *X*, *Y* stages were then recorded. This part was then aligned with the gripper manually using the front- and side-views. By activating the 'confirm' button, the encoder reading was again recorded. ***R*** was then obtained from the control system by subtraction of these too readings. The details of the calibration system and calibration process will be discussed in Chapter 7.

6.4 Control Law

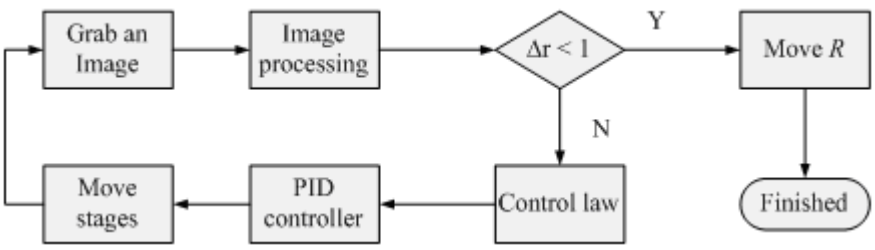

Figure 6.5: Time sequence of the alignment process.

To avoid instability, the alignment process worked in a look-and-move fashion. The time sequence of the alignment process was shown in Figure 6.5. First an image was grabbed and then image processing gave the position of the feature in the image. Real position error was then obtained and sent to the control law, which computed a position command to the PID controller, thus moving the *XY* stage. After the motion was completed, the PID controller will inform the computer and a new image was grabbed for processing. If the position error was still larger than the acceptable level, the above steps were repeated until the error became smaller than the threshold, which was set to 1 pixel in the experiment.

As discussed before, since the image plane was parallel to the working-platform, no Jacobian matrix was needed to translate coordinates from image frame to real world frame, and there was no need to match an image to the real world. The coordinates of a feature in the real world frame was no needed, only the position error was needed. Since the magnification of the microscope was fixed, the real position error can be obtained from

$$\Delta r_{real} = K_1 \Delta r_{image}, \tag{6.2}$$

where Δr_{real} was the real position error, Δr_{image} the pixel position error in the image, and K_1 can be obtained by measuring the real world size of the field of view. The field of view was measured by using a silicon micro ruler. By seeing the ruler though the microscope we could measure the field of view as 1*mm* in length. As the size of the image was 640×320 pixel, so $K_1 = 1000/640 = 15.6 \mu m / pixel$.

The proportional control law was the same for both *X* and *Y* axes and described by

$$U = k\Delta r_{real} . \tag{6.3}$$

where U is the distance command sent to PID controller and k a proportional coefficient. The influence of k on the performance of the controller was shown in Figure6.6. For k = 0.3, it will take about 9 cycles to converge, and if k = 1.0, there will be instability in the system, the object will vibrate around the target position. In the automated assembly experiment we set k = 0.5.

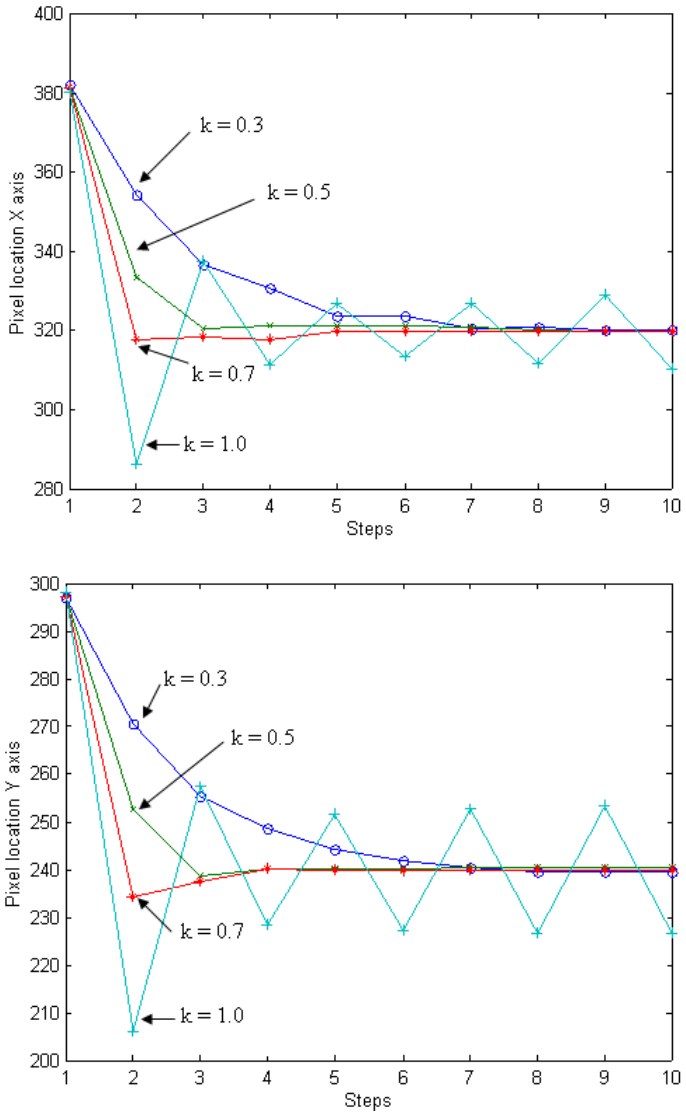

Figure 6.6: Influence of k on convergence.

6.5 Image Processing Algorithm

Different image processing algorithms had to be used for locating features in different cases: pattern matching was used for locating a single part or releasing structure, while Hough transform (HT) was implemented for locating a receptor. Pattern matching was simple, fast and easy to implement, but it was sensitive to variations in the background. In the former case, the background did not change, and so pattern matching was reliable. However, for determining the position of the receptor as layers of parts was assembled, the background kept changing, and an algorithm based on HT had to be implemented. The details of both algorithms are presented below.

6.5.1 Pattern Matching Technique for Locating a Part

The image processing algorithm used for locating a part on the part wafer used pattern matching. The pattern matching technique consisted of searching a predefined template (a typical target image) in the whole source image (images grabbed in process) by using normalized grayscale correlation.

Figure 6.7 shows the part template, which was a typical image of a part with the wafer as background. The reference position of the template was set at the center of the template, so that the searching result gave the center position of the part on the source image. In fact, the reference point could be any point of the template. The normalized correlation of the template with a sub-image of the same dimension from the original image was computed, and the maximum correlation coefficient

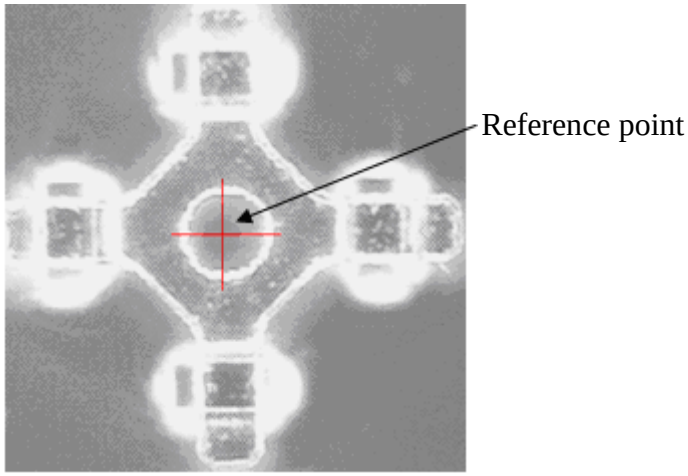

Figure 6.7: Micropart template, a typical micropart image on the wafer.

was interpreted as a match. The correlation coefficient is computed as

$$r = \frac{N\sum_i I_i M_i - \left(\sum_i I_i\right)\left(\sum_i M_i\right)}{\sqrt{\left[N\sum_i I_i^2 - \left(\sum_i I_i\right)^2\right]\left(N\sum_i M_i^2 - \left(\sum_i M_i\right)^2\right)}}, \tag{6.4}$$

where N indicates the number of pixels in the model, M_i, I_i denote the pixel value in the model and in the sub-image respectively and r is the normalized correlation coefficient [133]. The final score was computed as

$$Score = \max(r^2) \times 100\%. \tag{6.5}$$

If *Score* is larger than acceptance level, the corresponding sub-image is determined to be a match. In this project, the acceptance level and certainty level were set to be 60%. Upon successful matching, the position of the part was obtained and the pixel position error was then computed as

$$\begin{cases} \Delta x = 320 - x \\ \Delta y = 240 - y \end{cases}, \tag{6.6}$$

where (x, y) is the coordinate of the template in the source image and (320, 240) is the centre of the image.

If the target pattern was not found after searching the whole image, a 'NULL' result will be sent to the supervisory system. A failed search was often caused by defects in the part or the absence of the part.

The same technique was used in locating the releasing structure. The height of the disposal structure was designed so that it will also be in the focal plane during the calibration stage. But, because the disposal structure was fixed on the *V* stage, it will move downwards as layers of parts were assembled, which will cause it to be defocused. To circumvent this problem, each time before searching for the releasing structure, the *V* stage will be move back to its original position to make sure that the releasing structure was in focal plane. The template and the source image of the disposal structure are shown in Figure 6.8.

6.5.2 Modified Hough Transform for Locating a Receptor

The exact position of the receptor was determined by locating the hole of the part, which appeared as a circle in the image, as shown in Figure 6.9. Hough Transform (HT) technique is a straightforward and robust way to detect circles. The main advantage of Hough transform technique is that it is relatively unaffected by image noise. The use of the HT to detect circles is outlined by Duda and Hart in [149]. Yue compared variety of circle detection methods based on HT in terms of computational efficiency, storage, accuracy and reliability in [150].

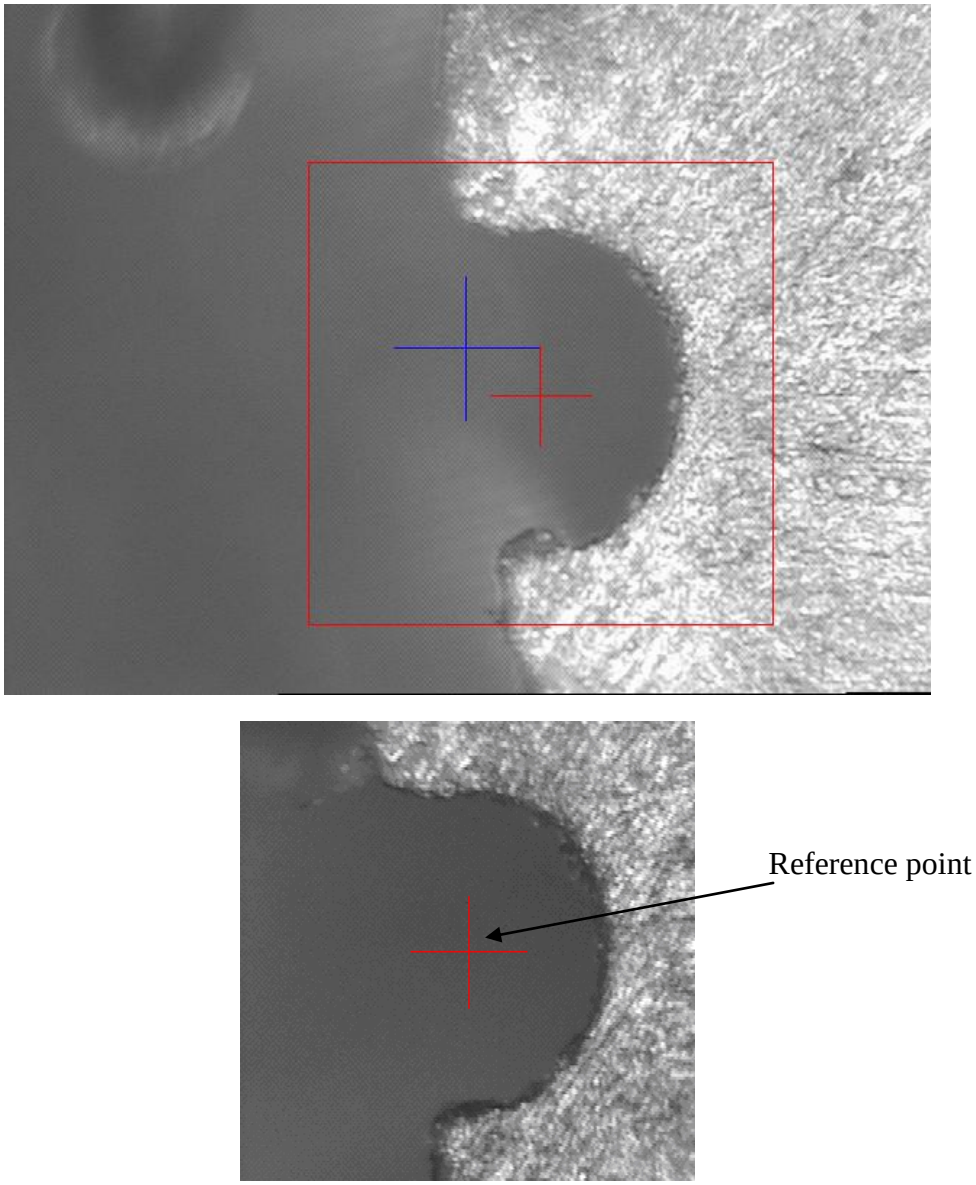

Figure 6.8: A typical top-view image of the releasing structure and releasing structure template.

As described in [150], HT computation goes as follows. First a constraint equation was constructed to describe the searched shape. For each feature point, votes were accumulated for all parameter combinations which satisfied the constraint. The votes were collected in an array of counters which was called the

accumulator array. The accumulator array was a discrete representation of the continuous multidimensional space which spanned all feasible parameter values.

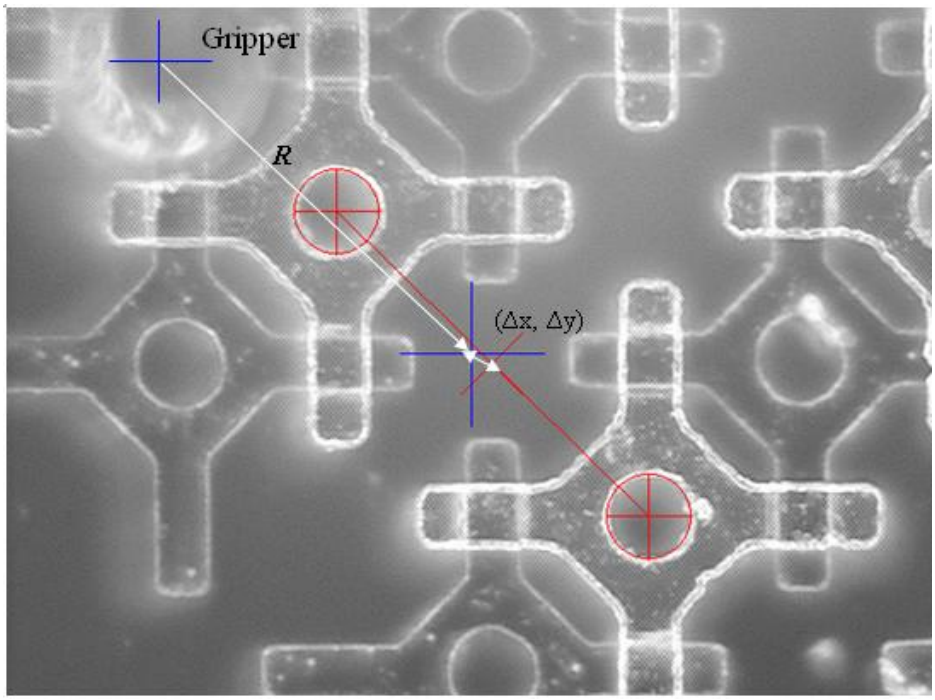

Figure 6.9: A typical top-view image for aligning a receptor, before alignment.

Edge points from a single instance of a shape vote coherently into the accumulator counter which is closest to the parameters of the shape. At the end of the voting or accumulation process, those array elements containing large numbers of votes indicated strong evidence for the presence of the shape with corresponding parameters. Shapes were detected by identifying peaks in the accumulator array.

The constraint equation for describing a circle is

$$(x-a)^2+(y-b)^2=r^2, \tag{6.7}$$

where (a, b) are the coordinates of the center and r is the radius. (x, y) is a point coordinate on the edge of the circle. And, if r is fixed, for any edge point (x, y) could be a point on any circle whose center is r distance away from this point on

the *a*-*b* frame. If for all the candidate edge points, a circle of *r* in radius is drawn in the *a*-*b* frame, the more the circles intersected at a particular point, the larger the

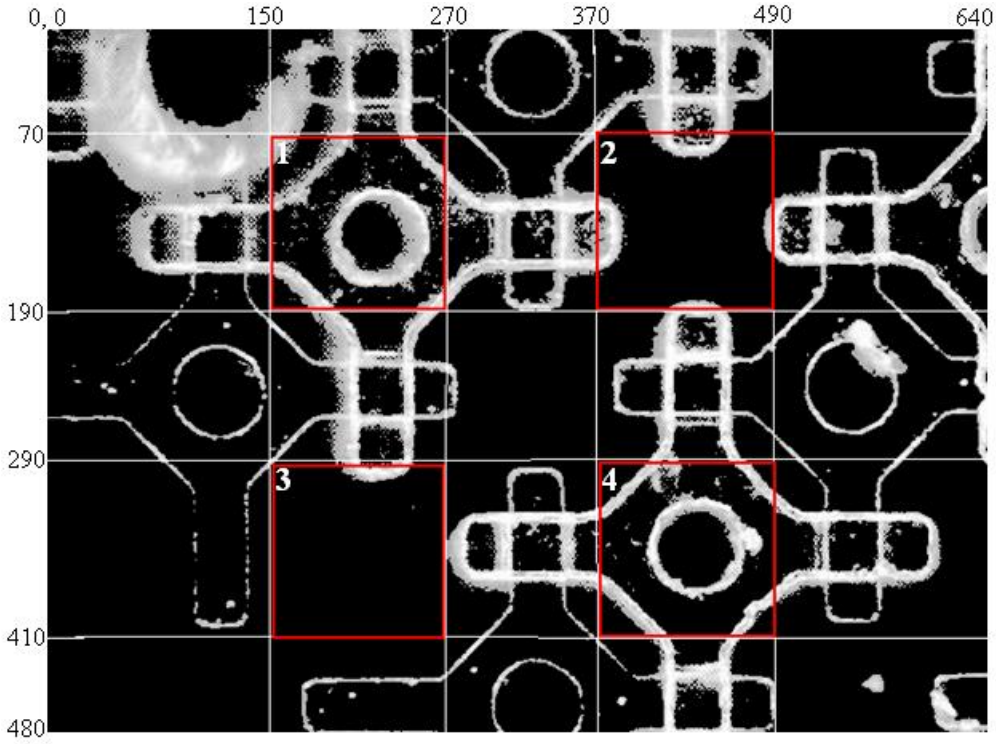

Figure 6.10: Image of receptor after thresholding (threshold is 170).

possibility that the coordinate of this point is the center of a circle in the image.

In our case, radius *r* was not a fixed value, but confined to a certain range, from 28 pixels to 32 pixels, based on experiment, and the line width of the circle ranged from 2 to 5 pixels. Since only the center position of the circle was needed, the 3D parameter space was reduced to a 2D space. A 2D accumulator array was employed and the array had the same dimension of the original image.

The candidate edge point was obtained by thresholding the original image. Thresholding was typically used to get a binary image out of a grayscale image. In this project, the thresholding was to set the pixels whose values were smaller than a threshold value to zero and those with values larger than the threshold were

unchanged. The original image was single-channel grayscale image with a depth of 8 bits, which meant that the maximum value of the brightness is 255. The threshold was set to be 170, and the image after thresholding was shown in Figure 6.10.

Further, brightness of the pixels was also considered to achieve a better accuracy. For each non-zero point, votes were given to all its parameter cells in 2D space and all possible radius values: 28, 29, 30, 31 and 32. If an accumulator was voted by a point, the intensity value of the point will be added to this accumulator so that weight was given to each point according to its brightness.

In order to reduce computation, only part of the image was considered as shown in Figure 6.10. In this case, because the receptors are located at the top-left and bottom-right of the image, only areas 1 and 4 were transformed, while in the case when receptors are located at the top-right and bottom-left of the image, only areas 2 and 3 will be transformed. Based on the design of the scaffold and the assembly sequence, the decision of which areas will be transformed was made before HT was performed. The peak points were identified by thresholding and local maximum detection. If more than one peak point was identified in a single square area, the maximum of these peaks will be considered as the center of a circle.

After the centers of the two circles were located, the center position of the receptor was obtained from

$$\begin{cases} x_c = \left(x_{c1} + x_{c2}\right)/2 \\ y_c = \left(y_{c1} + y_{c2}\right)/2 \end{cases}, \tag{6.8}$$

where (x_{c1}, y_{c1}) and (x_{c2}, y_{c2}) are the pixel coordinates of the centers of the two circles.

There are two salient features about this HT algorithm. First, instead of adding 1 for each pixel votes to the accumulator, the intensity of the pixel was added to the accumulator, so the brighter the point, the more weight will be given. Second, for each pixel the radius value covered all possible radii. This way the computation and storage are reduced, but the exact radius cannot be obtained through HT. This was not important here since only the center position of the circle was needed.

6.6 Conclusion

This chapter presented the fine alignment strategy and control law in all possible situations. Basically, the control strategy was simple position-based visual servoing. For alignment with a single micropart and the releasing structure, pattern matching was used to estimate the position of the features, while an algorithm based on the Hough transform had to be developed for locating the circles corresponding to the microparts center. Experiments tested the feasibility and efficiency of these algorithms.

The alignment accuracy was not analyzed theoretically, because for the real image, it was hard to tell where the true center was. [150] used synthetic images for measuring errors of different HT algorithms. For a synthetic image, the exact position of a feature was known, and error was obtained by comparing with the estimated position. But for the HT used in this project, the image processing

always gave the exact value of the parameters in the synthetic image. Gradient information was not used in the HT, as it was too sensitive to noise, and will cause instability in the system, as was actually experienced initially. Other methods for locating the circles were tested such as fast Hough transform (FHT) and ellipse fitting; however none of them worked well and they were found to be unstable.

The experiments showed that the accuracy was acceptable for this microassembly task. For picking up and assembly alignment, misalignment occurred about once in 5 trials, due to defects in the micropart and the noise caused by motion of the stages.

Chapter 7

Dedicated Workstation for Automatic Assembly

In this project, microscopic building blocks (of size $0.5 \times 0.5 \times 0.2 mm$ with $0.06 mm$ wall thickness) will be assembled automatically to fabricate tissue engineering scaffolds. Different from robotic tasks in the macroworld, microassembly poses new challenges and problems in the fabrication of microscopic components, handling tools, the design of the conveying and alignment mechanisms, control strategies, etc. The difficulties for positioning control and force control have been discussed in Chapters 5 and 6, respectively. This chapter will present the whole automated microassembly system, i.e. its hardware and software. The calibration and the automated assembly processes will also be presented in this chapter.

7.1 Experiment Hardware

Hardware of the automatic microassembly system consisted of mainly four modules: the visual module, the motion module, the force sensing module, and the microgripper. The force sensor and microgripper had been discussed in Chapters 5 and 4. The following paragraphs will present the motion and visual modules.

7.1.1 Motion System

All the necessary motions including conveying, alignment, insertion and abandonment were accomplished by four precision stages (see Figure 7.1). All the precision stages are from Physik Instrumente (PI).

Two precision translation stages (*X* and *Y* stages) were fixed together to serve both as a conveyer for long distance conveying and the vision-based positioning control loop for alignment. The working platform (a vertical stage, an adjustable plate and an adaptor) was fixed on the *XY* stage. During the assembly process, the position of the gripper remained constant in the *x*-*y* direction; it was through the motion of the whole platform that microparts were conveyed and assembled. Both the *X* and *Y* stages (PI, M-511.DD) have an optical linear encoder mounted close to the ball-screw, providing a resolution of 0.1μm. The maximal velocity is 50*mm/sec* and travel range is 102*mm*. The accuracy per 50*mm* is 0.2μm.

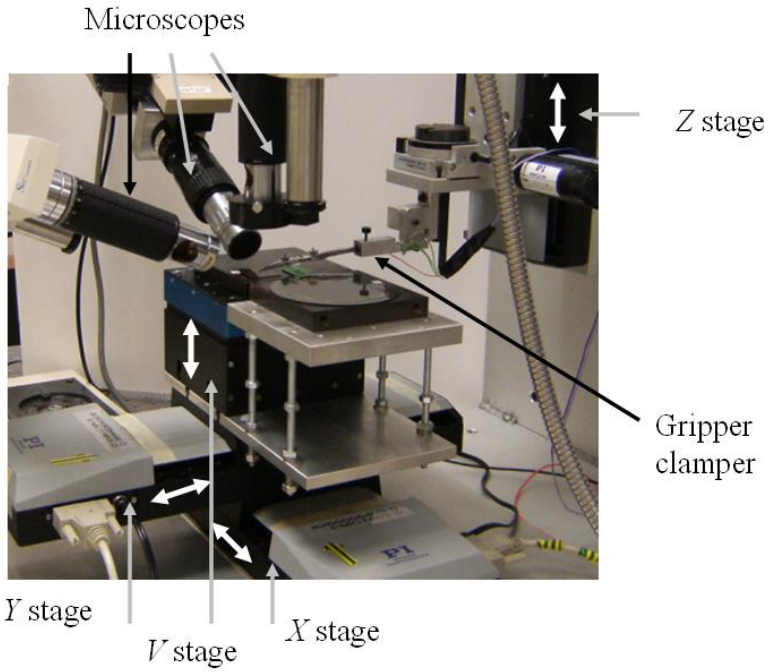

Figure 7.1: The precision desktop workstation.

The *Z* stage (PI, M-511.DDB) carried a clamper with the microgripper to move up and down and accomplished picking up and assembly actions. The *Z* stage shared the same parameters with the *X* and *Y* stages in terms of travel range, velocity, resolution and accuracy. What was special about it was that it had a brake integrated to lock the stage when powered off, so that it will not slide down due to gravity.

A vertical micropositioning stage (PI, M-501.1PD), *V* stage, was used to keep the object of interest in the focal plane of the top-view microscope. After each layer of parts was assembled onto the scaffold, the *V* stage will move down a certain distance so that the top layer of the scaffold will always be in the focal plane. The motion distance may be different for different scaffold architecture design; normally it is in the range from 100μm to 120μm. The designed resolution of *V* stage is 0.008μm, travel range 12.5*mm* and maximal velocity 15*mm/sec*.

All the four stages were controlled by a multi-channel controller (PI, C-842). The control card was based on a multi-processor architecture. It included a fast DSP motion-control chip set (providing trajectory generation and closed-loop digital servo control based on position information from the encoders) and a host processor for communication and command handling. It had an *S*-curve profile generation which enabled smooth velocity changes and a 32-bit PID servo-control.

A rotation stage (PI, M-037DG) was used to provide rotation during the calibration of the gripper's orientation and then will remain idle during the assembly process. It was driven by a 3 *Watt* DC motor with 29.6:1 back-lash free gear head and a 2000-count encoder mounted on the motor shaft. It was equipped with precise

worm gear drive allowing unlimited rotation in either direction, with 0.1° graduation.

7.1.2 Visual System

Three microscopes with CCD camera were used to provide front, side and top views of the working area. The top-view microscope (Zeiss, 8× SEC-zoom4) with a 1/3-inch CCD camera (Sony, SSC-DC10) was used for closed-loop position control. The side-view microscope (Navitar, 12× 1-50504) with camera (JVC, TK-C1481BEG) was used both for calibration and monitoring assembly process. The front-view microscope (Zeiss, 8× SEC-zoom4) with camera (Sony SSC-DC10) was used in the calibration process. Signals from the microscopes were transmitted to a Matrox Meteor II graphics board, and then to the computer for further processing. The graphic board was programmed using the Matrox Imaging Library (MIL). The host PC was a Pentium III 400-MHz 512-MB RAM computer using Windows NT. All the hardware was placed on an anti-vibration experimental bench in a clean room environment.

7.2 Hardware Calibration

Hardware calibration included the following factors: relative position and direction of the translation stages, position and direction of the microscopes, direction of the wafers, height and levelness of the working platform, and spatial orientation of the gripper tip.

7.2.1 Perpendicularity between Stages and Microscopes

The purpose of calibrating the translation stages was to ensure that the *X* stage was perpendicular to the *Y* stage and that the motion direction of both *Z* and *V* stage were perpendicular to the plane defined by the *X* and *Y* axis. The calibration work was done by using a dial gauge. Details are described in [133]. The shaft of the rotation stage and the optical axis of the top-view microscope also needed to be perpendicular to the *X*-*Y* plane which was also achieved by using similar method described in [133].

7.2.2 Calibration of Working Platform and Wafers

The design of the working platform is shown in Figure 7.2. The scaffold wafer was mounted on top of the *V* stage so that after each layer of microparts was assembled, the *V* stage will move down a certain distance to keep the top layer in the focal plane of the top-view microscope. Part wafers were fixed just beside the scaffold wafer to reduce the conveying distance. The base of the part wafer will be kept at the same height during assembly process, but its height was adjustable through the four supporting screws. The four screws were also used to adjust the level of the parts wafer to make it parallel to the *X*-*Y* plane.

The direction of both the part wafer and the scaffold base wafer must be consistent with the *X* and *Y* stages for two reasons. First, no re-orientation was carried out after a part was picked up, and so the part had to be aligned in the same direction with the parts on the scaffold base before assembly process. Second, before vision-

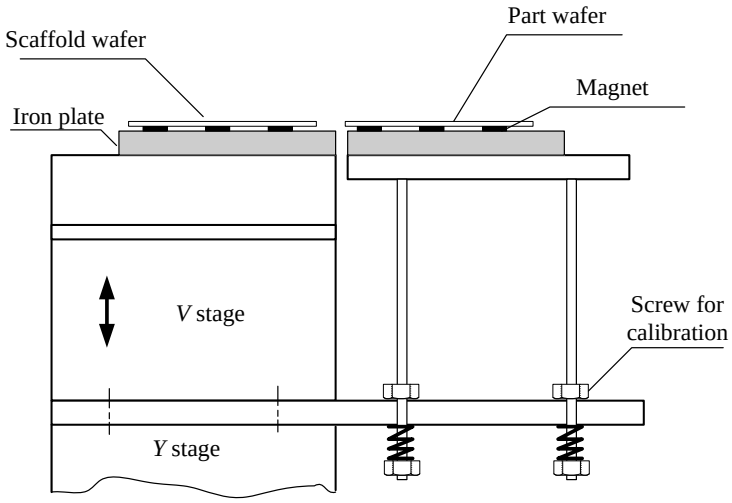

Figure 7.2: Front view of the working platform.

based alignment, locating a micropart or a receptor was done in an open-loop way: the position coordinates was calculated and a command was then sent to the *XY* stage to bring the object into the field of view of the top-view microscope. If the direction of the part array or the scaffold base was not consistent with the motion direction of the stages, a small angle error may cause a large position error for the object far from origin, which may cause the top-view microscope to miss the object.

To facilitate the adjustment of the wafer direction, the wafers are fixed on the base by a layer of magnet (of about 1*mm* in thickness) (Figure 7.2). Commonly, wafers were held by the use of vacuum, such as in spin coater, UV exposure machine, etc. Vacuum produced a large pressure difference on the top and bottom surface of the wafer so that the wafer was "pushed" against its substrate firmly. In our case, we do not need such a large force. A piece of iron with flat surface on both sides was first fixed on top of the working platform; magnets were glued to the wafer by double-sided glue. Using magnet as a fixation method made exchanging of wafers

and adjustment easy. The releasing structure was also fixed the same way on the *V* stage.

Calibration of the wafer direction goes as follows. First a cross was drawn at the center of the top-view microscope image. The cross functioned as a stationary reference point through the calibration process. Next the *X* and *Y* stages were moved to place one micropart at the center of the image (see Figure 7.3). Then the *X* or *Y* stages were moved 3.4*mm* (distance of 10 microparts). If all the centers of the microparts in the same row passed through the reference point, it meant that the direction of the wafer was consistent with the *X*-*Y* stage. If not, the top-view image will show the error. The wafer was adjusted to reduce the error. The adjustment process was repeated until minimum error was achieved. A wrong way of adjusting the wafer direction was to make the part parallel to the image. In fact, the image direction defined by the CCD camera direction was by no means a reliable one. The direction of the CCD camera should be calibrated according to the calibrated scaffold wafer. The calibration of part wafer was performed in the same way.

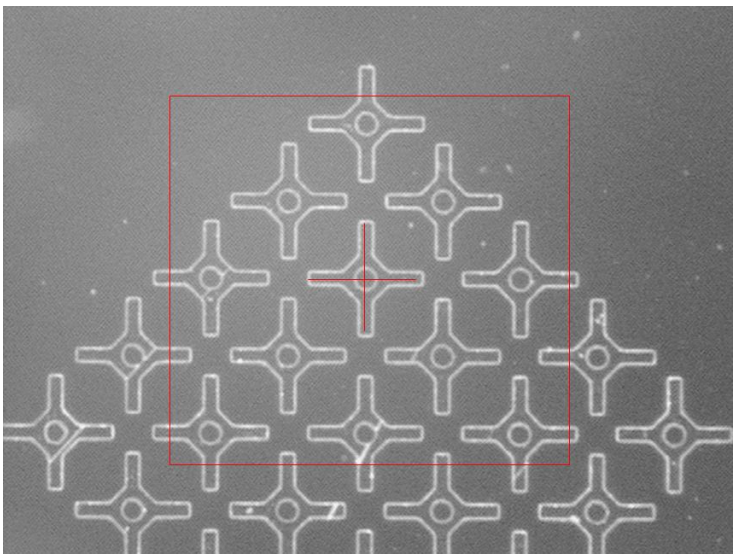

Figure 7.3: Calibration of the wafer direction.

7.2.3 Adjusting Spatial Orientation of Gripper Tip

Spatial orientation of the gripper clamper was adjustable in all three rotation axes, which meant that the gripper can present an arbitrary attitude. Here, we borrowed the terms used in aerospace engineering to define the orientation of the gripper clamper. The attitude of a rigid body can be determined by three angles: yaw (ψ), pitch (θ) and roll (φ) (see Figure 7.4).

In the calibration process, the first angle to be adjusted was the yaw angle (ψ). The rotation stage was adjusted until the tip of the microgripper was in the field of view of the top-view microscope. As the adjustment of φ and θ were coupled, the pitch angle θ was first adjusted until the gripper tip was normal to the wafer surface as seen through the side-view microscope. Then the roll angle φ was adjusted until the gripper tip was normal to the wafer surface as seen through the front-view microscope. As the pitch angle may be affected by the roll angle, the pitch angle was adjusted again. The process was repeated until the gripper tip was normal to the surface of wafer through both the side- and front-view microscopes.

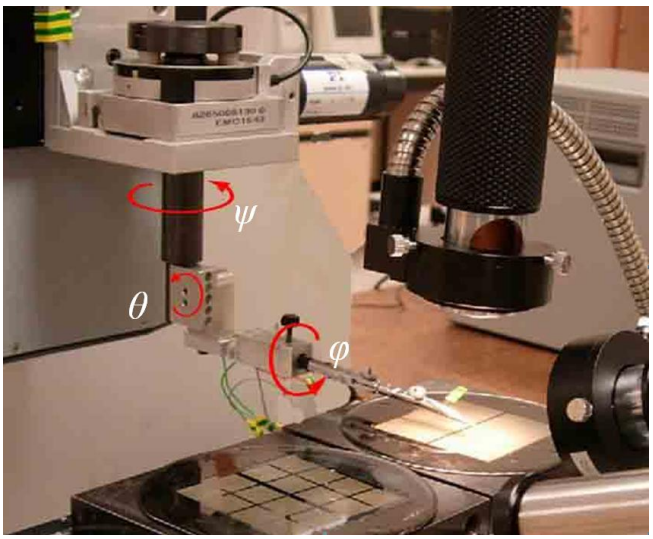

Figure 7.4: Closed-up view of the working space and the gripper fixtures.

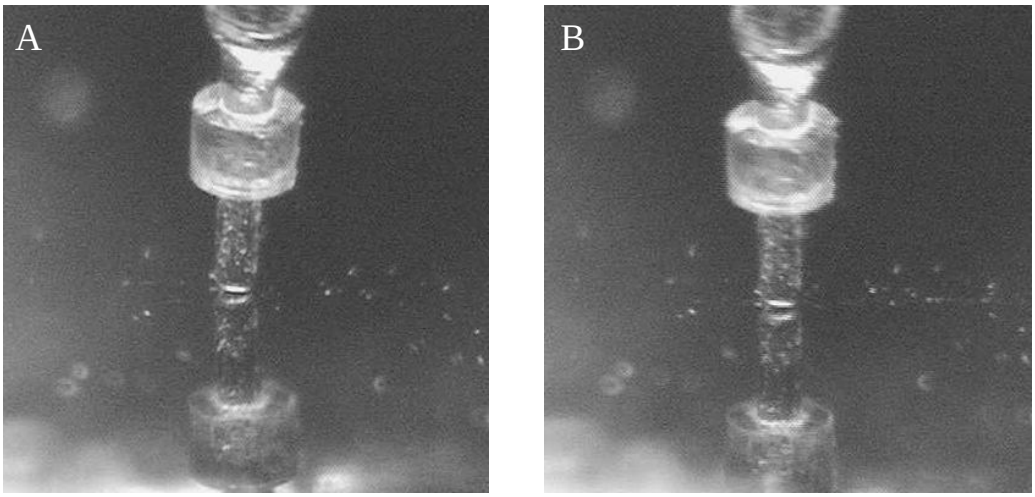

Figure 7.5: Adjusting spatial orientation of microgripper tip. (A) Gripper tip is not normal to the wafer surface. (B) Gripper tip is normal to the wafer surface.

There was a simple way to decide whether the tip was normal to the surface accomplished by checking the image reflected by the silicon wafer. If the image of the gripper tip was in line with the gripper tip, it meant that the gripper tip was normal to the surface of the wafer (see Figure 7.5). Again, the direction of the image can not be the reference for adjusting the direction of gripper tip.

7.3 Experiment Software

A program in visual C++ was developed to control and coordinate all the hardware and also provide a user-friendly graphic user interface (GUI) for easily calibration, manipulation and observation of the automated assembly process.

Figure 7.6 shows the GUI of the control program. The controls on the right side of the GUI are divided into four groups: (1) Vision controls used for switching image from different microscopes during calibration process, saving pictures and testing image process codes, etc. (2) Manual operation controls used for the four stages in

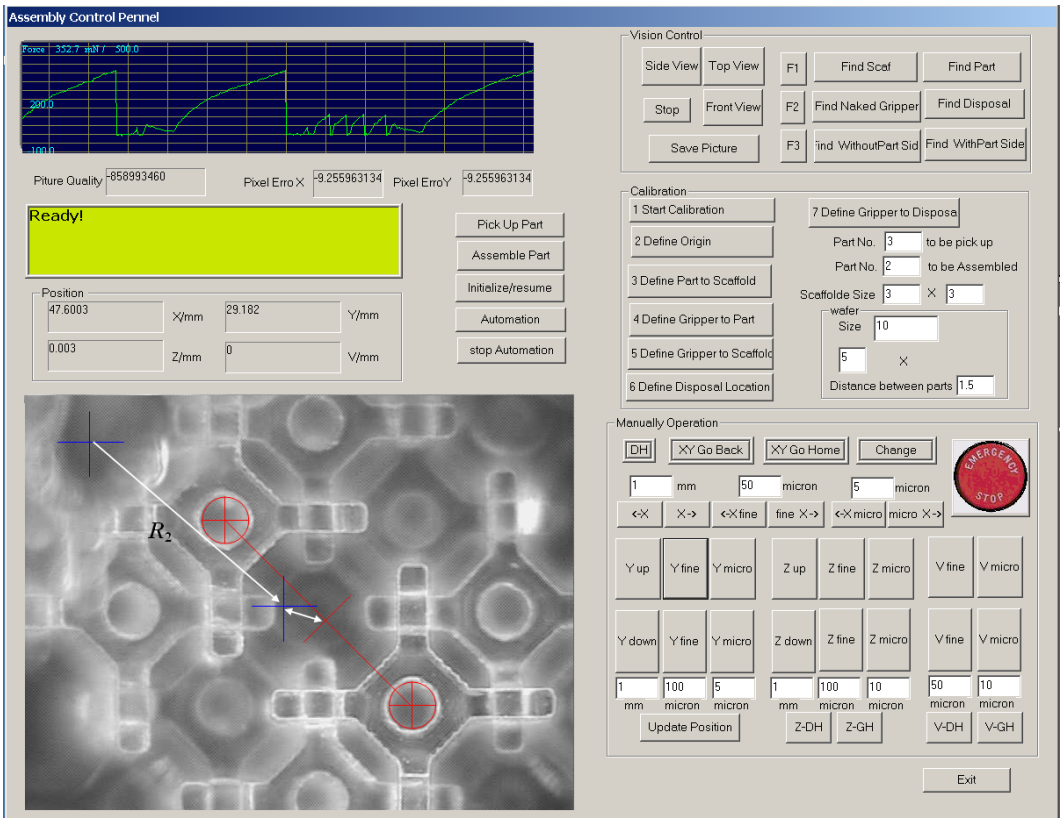

Figure 7.6: Graphic user interface of the proposed software.

tele-operation fashion, which will also be used in the calibration process. (3) Calibration controls are seven ordered controls. During the semi-automated calibration (details will be discussed in Section 7.4) process, all the seven buttons will be clicked so that the program will be loaded with the designated positions. The size of the perspective scaffold, the type and size of the parts array, etc will also be loaded prior to the assembly process. (4) Automation controls have five buttons; they are used for automatic picking up, autoassembly, and begin, pause, stop or resume an automated process. On the left side of the GUI, are the real-time force profile display, image properties, notice board, position of all stages, and real-time image from microscopes. The notice board will present the instructions

for the operator during the calibration process, and if the system stops, the fault type will also be presented on the notice board.

The program also helps in preventing damages to the microgripper from misoperations. Two types of misoperations may damage the microgripper: moving down the gripper by a too large step that causes it to collide with the base; turning on the power of the stages before initializing the control card which may cause the *Z* stage to drop down. To prevent the damage from the first misoperation, force value will be read every time a move-down *Z* stage button is activated. Once the force value is larger than a certain threshold, the *Z* stage will be stopped automatically. To prevent the second kind of damage, a relay is used to allow the program to control the power supply of the stages. Stages will turn on automatically after the initialization process.

7.4 Software Initialization

Prior to the automated assembly process, the program must be loaded with the position of the first receptor (*0, 0*), position of the first micropart on the parts array (x_{p0}, y_{po}) and position of the releasing structure (x_r, y_r). As shown in Figure 7.7, the coordinate frame *x-o-y* was fixed on the platform with its origin coinciding with the center of the first receptor and the *x, y* directions consistent with the *XY* stages, respectively. The accurate relative position $\boldsymbol{R}$ (refer to Chapter 6) should also be loaded into the program. $\boldsymbol{R}$ may differ slightly in the three situations for which closed-loop position control was needed: alignment with a single part, alignment

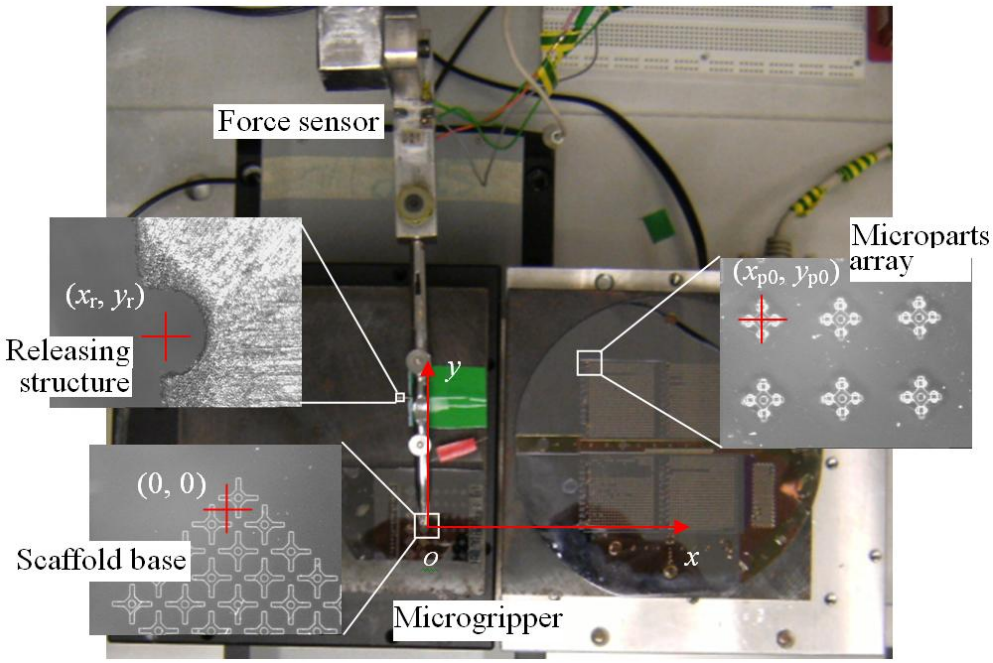

Figure 7.7: Top-view of working platform.

with a receptor and alignment with the releasing structure, which we denote by $\boldsymbol{R}_1$, $\boldsymbol{R}_2$ and $\boldsymbol{R}_3$ respectively.

The program initialization process began by activating the "start calibration" button on the GUI. The steps are:

1. Manually move the *X*-*Y* stage to bring the first receptor into the field of view of the top view microscope. Clicked on the 'define origin' button. The program will begin the closed-loop position control process which is the same as described in Chapter 6. After the center of the receptor coincides with the center of the image, the program will set the *XY* stage position encoder to zero.
2. Move the *XY* stage to bring the first part into the field of view of the top-view microscope. Click 'define first part' button and the program will begin closed-loop position control again to place the part in the center of

the image and then the program will record the encoder reading of the *XY* stage. This will form the coordinates of the center of the first part in the working platform frame (x_{p0}, y_{p0}). The accuracy of the encoder is $0.1\mu m/50mm$, which is sufficiently accurate for the calibration process.

3. Move the *XY* stage manually to place the first part under the gripper. Then adjust the *XY* stage using the side- and front-view microscopes to align the gripper tip with the hole of the part. Click 'define gripper to part' button. The encoder reading will be recorded as (x_{p1}, y_{p1}). The relative position $\boldsymbol{R_1}$ is given by

$$\boldsymbol{R_1} = (x_{p0} - x_{p1}, y_{p0} - y_{p1}). \tag{7.1}$$

4. Pick up the part and click on 'go home' to move the first receptor under the microscope and then align the part with the receptor through the side- and front-view microscope. Click the 'define gripper to scaffold' button. The position of the *XY* stage (x_{01}, y_{01}) will be recorded. $\boldsymbol{R_2}$ is then given by

$$\boldsymbol{R_2} = (- x_{01}, - y_{01}). \tag{7.2}$$

5. Bring the releasing structure into the field of view to load the program with (x_r, y_r) as in previous two situations.

6. Align the notch of the releasing structure with gripper tip. This time, different from the above process, not only the position of the *XY* stage but also the position of the *Z* stage will be recorded, because the releasing process is an open-loop action in the *Z* direction. The pushing shoulder should be lower than the top surface of the releasing structure.

7.5 Automated Microassembly Process

After calibration and initialization of the program, by activating the 'auto-assembly' button on the GUI, the automated assembly process will be conducted under the control of the supervisory unit. The whole system was hierarchically organized: the high-level supervisory unit planned movement tasks, made decisions and presented a set of commands to the lower-level controllers; while lower-level systems worked in a closed-loop fashion. Vision information was used for closed-loop positioning control to achieve positional accuracy less than $10\mu m$. With the assistance of closed-loop force control, insertion action was accomplished without the risk of damaging the microparts.

Figure 7.8 shows the flow chart of the whole automated assembly process. The assembly of each micropart consists of the following steps:

1. The gripper moves above a micropart and then aligns with it using vision feedback. If the micropart has already fallen of the wafer or if the micropart has some major defects, the top-view vision will fail to locate the micropart and supervisor unit will command to move the gripper to the next micropart.
2. The micropart was automatically picked up from the wafer by closed-loop force control as discussed in Chapter 5. The supervisory unit then switches to the side-view image to infer whether the micropart was picked up or not. Details about side-view image processing will be discussed in Section 7.6. If not, the gripper will move to the next micropart.

3. The micropart is conveyed to the scaffold and aligned with the receptor, based on vision feedback.
4. The micropart is assembled onto the scaffold, and then a side-view image will be taken again to infer whether the micropart was assembled successfully or not. If failed, the micropart is disposed with the releasing structure and another part will be picked up to be assembly to the same receptor again.

If an action fails three times in a row, it is deemed that a fault situation occurred and the whole system will be stopped to prevent damages. The fault type will be shown on the notice board.

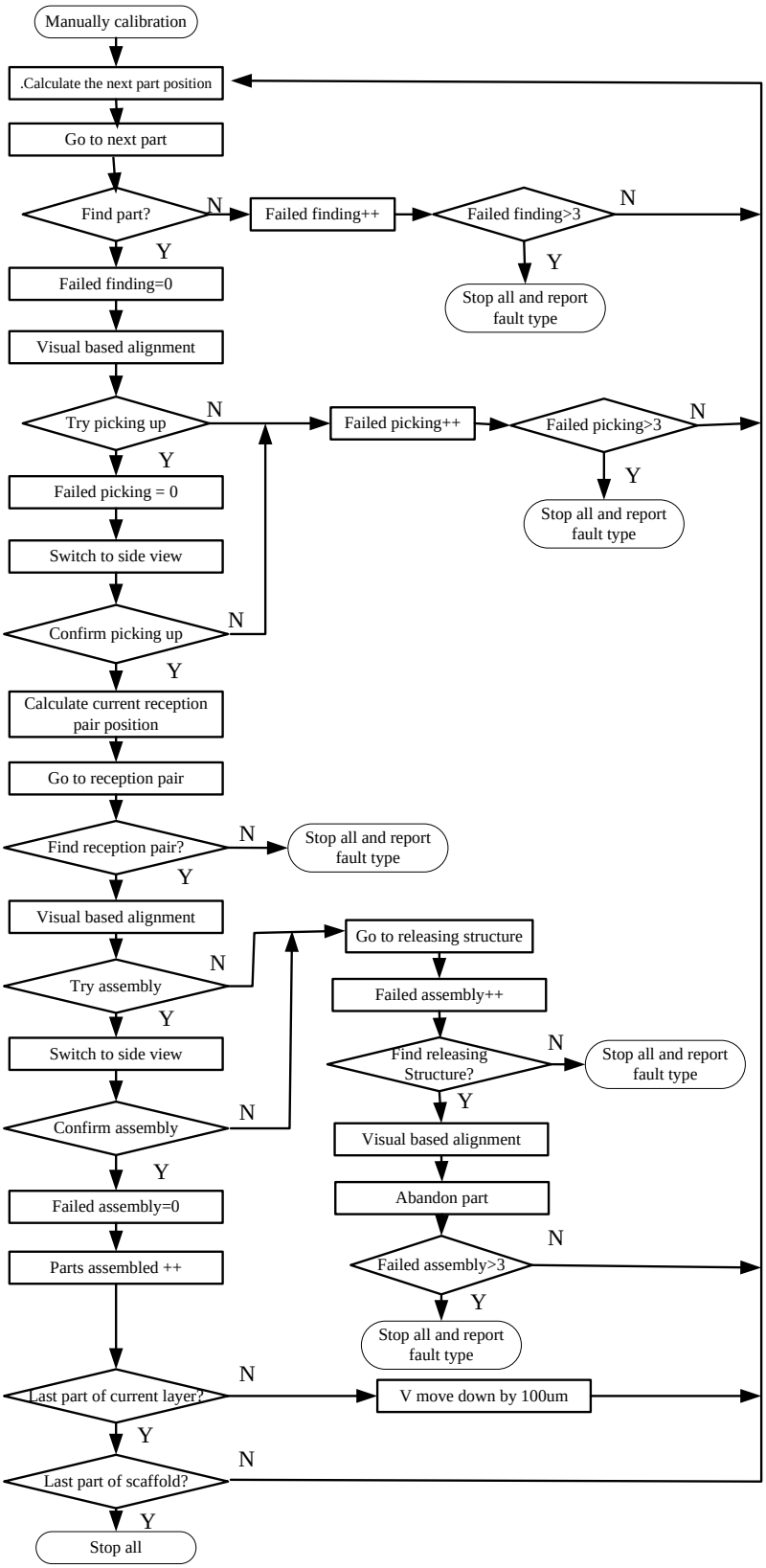

Figure 7.8: Flow chart of the whole automated microassembly process.

7.6 Image Processing for Inferring the Assembly Status

After the pick-up and assembly actions, the supervisory unit will switch its image source from the top-view microscope to side-view or front-view microscope, and then take a picture for processing to determine whether a part had been picked up or assembled successfully, based on which further decisions will be made. The result of this process determined whether a gripper with a part or a naked gripper was in the image. If a naked gripper was detected after assembly action, it meant that the assembly was successful: the part remained on the scaffold. If a gripper with part was detected after the pick-up action, this meant that a part has been picked up successfully.

To detect whether an object of interest is in the image is a problem of automatic target/object recognition (ATR) which has been studied extensively [151, 152]. There are lots of issues in the area of ATR [153], while only the related aspects will be discussed here. The ATR algorithms used can be model-based techniques, statistics-based techniques, Hough transform, Morphological techniques etc. There four terms are typically used in ATR algorithms:

True Positive: The object is in the image and the processing gives positive results.

True Negative: The object is not in the image and the processing gives negative.

False Positive: The object is absent from the image but the processing gives positive.

False Negative: The object is in the image and the processing gives a negative result.

In this project two methods were tested: template matching and calculating of image sharpness.

7.6.1 Template Matching Method

Template matching is the simplest and most often applied method in the ATR application domain. First a typical image of the naked gripper and gripper with a part were taken as shown in Figure 7.9. Then the template image was searched in the whole source image. The searching algorithm is the same as described in Chapter 6. The acceptance level of template matching is set to 55%. If the template is found in the source image, a positive result will be given, and if not, a negative one.

A B C

Figure 7.9: Templates for automatic target recognition: (A) a naked gripper; (B) a gripper with part (front view); (C) a gripper with part (side view)

The logic of the supervisor system is as follows:

Case 1: The search for naked gripper was negative and gripper with part positive. This means that a part was picked up successfully and the part is in good condition. Then the supervisor will sent command to assemble this part.

Case 2: The search for naked gripper was positive and gripper with part negative: This means that the part was not picked up at all, and a command was sent to pick up the next part.

Case 3: The search for naked gripper was negative and gripper with part also negative: This means that a defected part was grasped, and then the supervisor will command to execute abandon-part action.

Case 4: The search for naked gripper was positive and gripper with part also positive: this situation should not happen, but if it did, the whole system will be stopped and "FAULT" displayed on the notice board.

The advantage of this method is that it is simple and straightforward, and contributes to determine whether the part has quality problems. The disadvantage is that it is sensitive to many factors: the illumination condition, the magnification of the microscope, the intensity of the background. Before assembly, all these factors should be adjusted to the condition when the template was made. And even though all the above conditions are the same, the template matching method is still negatively affected by the fact that different parts have different textures which may cause false negative results when searching for gripper with part. And hence qualified part may also be rejected.

7.6.2 Image Sharpness Method

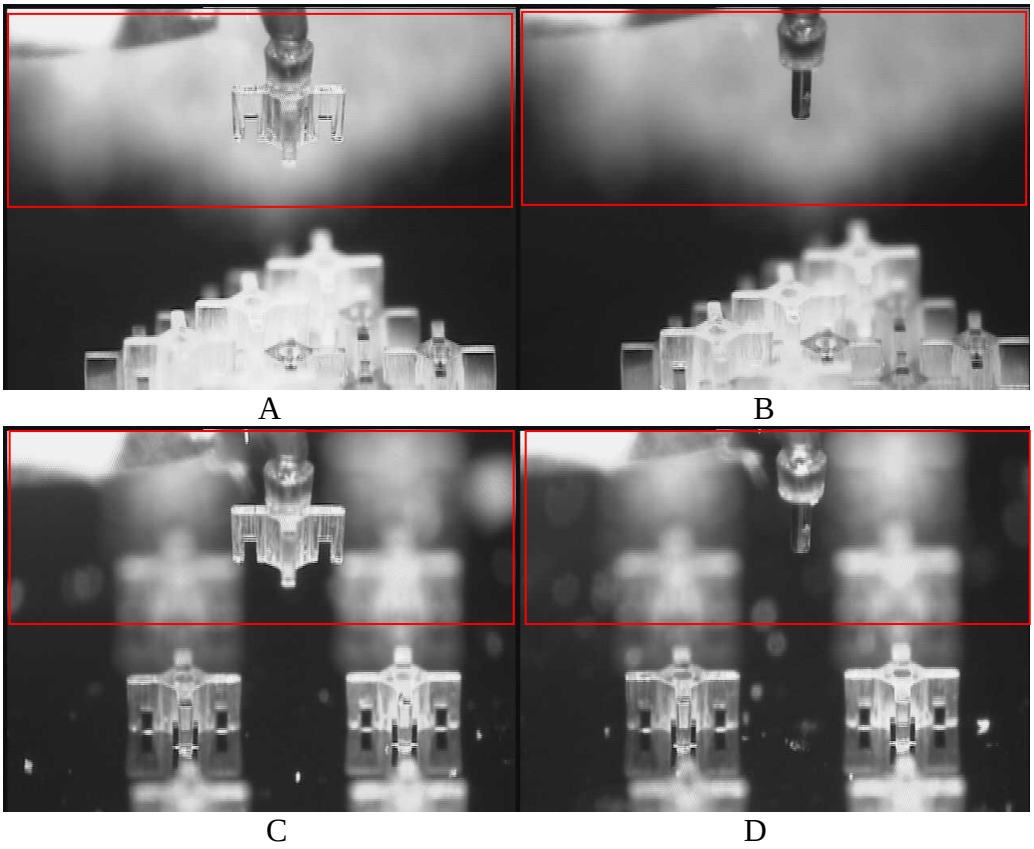

Figure 7.10: (A) A typical image of the gripper with part and with scaffold as background; (B) image of a naked gripper with scaffold as background; (C) image of gripper with part and part wafer as background; (D) image of naked gripper with part wafer as background. (The area inside the red rectangle is computed.)

The second method for determining whether an object is present in an image took advantage of the fact that an object appears sharp when it is in the focal plane. As we discussed before, the depth of field of the optics use in micromanipulation was in the range of tens of microns. From Figure 7.10 we can see that only the in-focus objects look clear and those that are out of focus appear quite blurred and an in-focus part take larger area than an in-focus naked gripper. And the value of

sharpness might indicate the area of an in focus object accounts for the whole image and hence let us know whether it is a gripper with part or a naked gripper.

The sharpness function can be implemented by a variety of measures such as frequency domain functions, image power measures, gray level variance measures, gradient function, information content functions etc. [154, 155]. The sharpness function used in this project is introduced by Brenner [156]. This function measured the difference between a pixel and its neighbors two pixel away and summed it over the entire image. To reduce the computation and to make it more robust, in this project only half of the image was calculated: the half inside the rectangle (Figure 7.10). The Brenner focus function f_s is given by

$$f_s = \sum_x \sum_{y/2} \left[I(x+2,y) - I(x,y) \right]^2 , \tag{7.3}$$

where $I(x, y)$ represents the gray level of a pixel at coordinates x and y.

The sharpness function was computed over 40 sample images: 10 images were of the gripper with part and background was part wafer; 10 images were of the naked gripper and background was part wafer; 10 images were of the gripper with part and with the scaffold base as the background; 10 images were of the naked gripper with the scaffold base as the background. The images were taken with slight changes of illumination, magnification and position above the wafers, while keeping the gripper or the gripper with part in focus. The values of sharpness function are shown in Figures 7.11 and 7.12. There is an evident difference between images of gripper with a part and naked gripper.

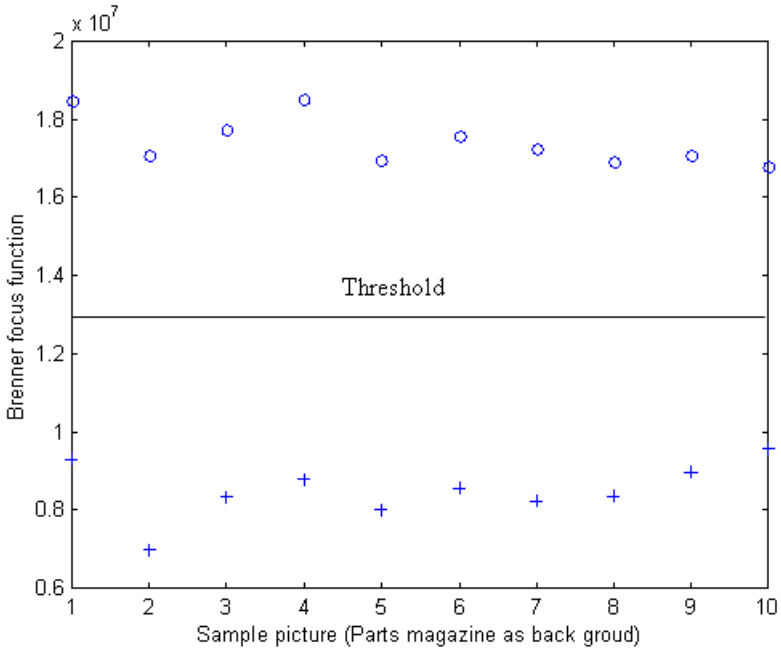

Figure 7.11: Sharpness of 20 images (backgrounds are part wafer): image of gripper with part (circle); image of naked gripper (cross)

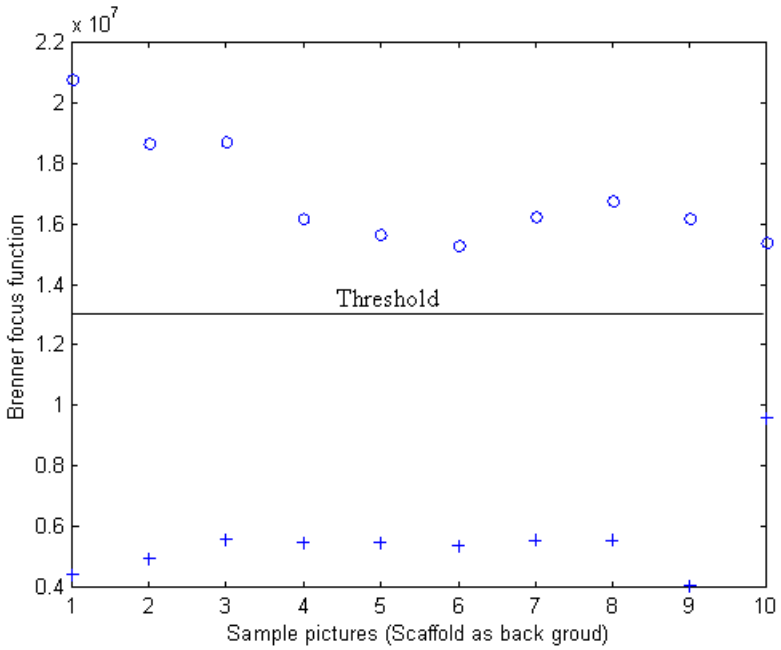

Figure 7.12: Sharpness of 20 images (backgrounds are part wafer): image of gripper with part (circle); image of naked gripper (cross)

In the experiment, the threshold was set to 1.3×10^7. Those images whose sharpness functions were smaller than the threshold were deemed to be the naked gripper. Otherwise, they were taken to be that of the gripper with a part.

In the experiment, to determine whether a part was picked up or assembled this way reduced a lot of preparation time, and the false negative rate was also reduced. The shortcoming of this method was that it cannot detect a defective part since a defect does not make much difference on the sharpness function. In the automated assembly experiment discussed later, the image-sharpness-calculation method was used.

7.7 Experiment Results

Automated microassembly of pyramid scaffold was carried out. Figure 7.13 shows such a scaffold composed of 50 microparts. If there was no multiple trials during inserting action, both the picking up and assembly a micropart took about 10 seconds and conveying and alignment of a part also took around 10 seconds. The assembly of each micropart took about 30 seconds. On the other hand, if the visual alignment error is larger than $5\mu m$, trials and errors of insertion will increase the pick-up and assembly to about 15 seconds so that it will take more than 40 seconds for a part to be assembled. The successful picking up rate was consistent with previous experiment, as discussed in Section 3.4. Only two parts failed to be released after assembly action, which corresponding to a successful assembling rate of 96%.

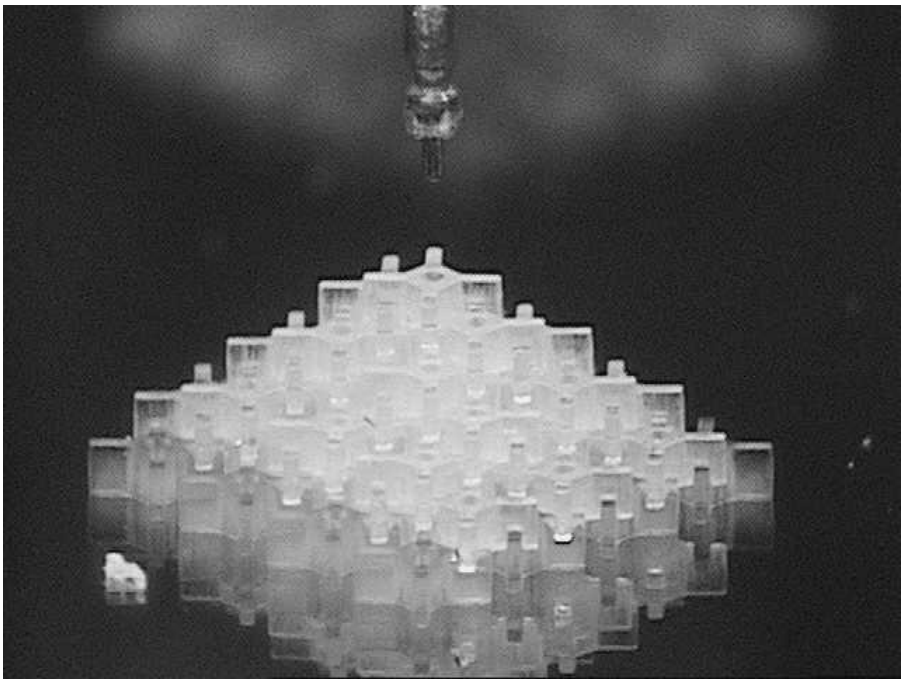

Figure 7.13: A small piece of automated assembly scaffold.

Fault situation occurred three times during this automated assembly process which has to be solved manually by an operator. All faults were induced by the defects of micropart which the image process algorithm failed to recognize. The first fault occurred when finding a single part by template matching from the top-view images. One part had fallen off the wafer, but because it left an imprint on the wafer, the image processing algorithm gave a false positive signal and the system began the picking up action on the vacant area. The acceptance level of the template match process was then increased to 70%. No more such phenomenon was observed. The other two faults occurred when using the side-view image to infer assembly status. In these two cases, the assembly action was actually a failed one: the part was still with the gripper after assembly. The image process gave false positive signal, and the system began to pick up the next part instead of abandoning the part.

7.8 Conclusion

This chapter presented the design, calibration and control software of a dedicated automated microassembly system. Automatic microassembly of TE scaffold has been carried out successfully.

The robotic workstation has four precision stages and three microscopes, which have been carefully calibrated to obtain a good relative directionality between them. The height and levelness of the working platform and the direction of the wafers have also been calibrated before assembly process. The microgripper fixed on a clamper was mounted on the *Z* stage to accomplish picking up and assembly action. The fixation mechanism has three rotation degrees of freedom that allows adjustment of spatial orientation of the microgripper. The control software coordinating all the hardware has a friendly GUI to make the initialization process easier. The automated assembly tasks were conducted under the control the supervisory unit of the software. To infer the status of the assembly process, two kinds of image processing algorithms are used to process side-view and front-view images.

The automated microassembly experiment was carried out and a piece of scaffold with 50 microparts was fabricated which proved the feasibility of realizing automated microassembly task by using both visual servoing and closed-loop force control.

Chapter 8

Conclusions and Recommendations for Future Work

This thesis presented an automatic microassembly system for fabrication of tissue engineering (TE) scaffolds. Customized TE scaffolds are fabricated by assembling Lego®-like micro building blocks together to form a 3D porous structure. An advantage of this scaffold fabrication technique is that seeding and culturing of cells and biological agents can be done prior to scaffold fabrication. Each micropart can first be coated with desired cells and growth factors (proteins, peptides, etc.) and then assembled on the scaffold. Through this process, the distribution of the cells and agents can be controlled in 3D so as to form different structures and cater to different patients. No thermal, electrical effect, pressure or toxic chemical reaction was involved during the whole assembly process.

While the feasibility of this TE scaffold fabrication process had been shown by using tele-operated assembly [9], the whole process was extremely tedious and time consuming. This thesis developed automated 3D assembly of these TE scaffolds.

A desktop workstation was first built. The working station has four degree of freedom and each axis has sub-micron positioning resolution. Three sets of microscope systems were used to provide top-, side- and front-view of the working space. A passive microgripper was designed and fabricated to handle the micro-parts. The design of the micropart was also modified to interface with the microgripper. The support of the microgripper was embedded with a dedicated micro force sensor measuring the interacting forces between the gripper and micropart or between microparts. High positioning accuracy was achieved by using visual servoing for which a modified Hough transform image processing algorithm was developed.

To safely and efficiently handle the micropart, closed-loop force control was implemented in the picking up and assembly actions. A program with friendly GUI was developed to coordinate all hardware as well as to supervise the whole automated assembly process. A calibration scheme was developed and automated assembly experiment was carried out. The 50-micropart scaffold assembled automatically demonstrated the effectiveness of the whole system.

With this system, the human operator is needed only during the calibration and fault situation. Compared with manually assembly process, the assembly speed was improved dramatically. The automation of the whole assembly process makes a big step towards the application of this kind of customized TE scaffolds. Some of the techniques developed in this project can also be applied to other microassembly tasks.

Although automated assembly of the customized TE scaffold has been achieved, several segments may be improved in further work. First, the successful rate of picking up and assembly, about 70% and 90% respectively, needs to be improved. Unsuccessful assembly will take some extra time as the micropart that has already been picked up has to be abandoned. To make the picking up and assembly more reliable, an actuator may be implemented on the microgripper to help release a micropart. This will enable using larger friction to hold a part so that not only the assembly but also the pick up will be improved. An idea consists of pushing the micropart out by using a tungsten sharp tip. The tungsten tip can be fabricated using the electrolyte etching technique and a piezoelectric actuator may be used.

Second, the efficiency still needs to be improved. So far, the maximum assembly speed is about 1/30*Hz* or 30 seconds to assemble one micropart. At this speed, to fabricated a 1*mm* cubic scaffold will take about 12 hours. This speed is not satisfactory for mass production. Using a parallel microgripper may enable the pick up and assembly of multiple microparts simultaneously. However the alignment may then be difficult. Alternatively, for uniformed parts of the scaffold, a larger piece may be used corresponding to several microparts. This will reduce the assembly time significantly.

Third, the dimensional accuracy of the micropart also needs to be improved. The relative dimension error of microparts used in this project is larger than 5%. Dimension errors accounts for almost all the faults that occurred during automatic assembly. Fabrication of large TE scaffolds also depends on the qualities of

microparts. So micropart fabrication technique is the key factor for the mass production of the customized TE scaffold.

Finally, the micropart used in this thesis is made of SU8 which is not biodegradable. To fabricate micropart with PCL (a kind of biodegradable material with similar mechanical properties), other micro machining methods can be used. Micro-molding is the most promising method. The challenge with micro molding may lies in the injection process and demolding. Injection may be difficult due to the high viscosity of PCL and demolding may cause damage to the thin legs of the microparts. Also, the parts will be needed to be correctly oriented before insertion. This can be done actively, by using a manipulator, or passively, by using a 3D structure with guiding notches and pushing the part against the guiding notches.

To circumvent all the rotation problems discussed above, an alternative way is to fabricate arrays of micropart; microparts are placed regularly by constraints of tethers. In the micro molding process, tethers can be designed which also formed the same way as the microparts and be of the same material. The tethers will break easily when picking up a single micropart. The CAD drawing of a symmetrical design of the micropart used for micro molding has been given at the end of Chapter 3.

Bibliography

[1] R. Langer and J. Vacanti. Tissue Engineering. *Science*, 260: 920-926, 1993.

[2] http://en.wikipedia.org/wiki/Tissue engineering

[3] J.P. Vacanti, M.A. Morse, W.M. Saltzman, A.J. Domb, A. Peter-Atayde, and R. Langer. Selective cell transplantation using bioabsorbable artificial polymers as matrices. *J Pediatr Surg*, 23(1):3-9, 1988.

[4] A.G. Mikos, G. Sarakinos, M.D Lyman, D.E Ingber, J.P. Vacanti, and R. Langer. Prevascularization of porous biodegradable polymers. *Biotechnol Bioeng.*, 42:7 16- 23, 1993.

[5] B. Robinson, J.O. Hollinger, E. Szachowicz, and J. Brekke. Calvarial bone repair with porous D, L-polylactide. *Otolaryng Head Neck*, 112(6):707-13, 1995.

[6] I.V. Yannas, E. Lee, D.P. Orgill, E.M. Skrabut, and G.F. Murphy. Synthesis and characterization of a model extracellular matrix that induces partial regeneration of adult mammalian skin. *Proc Natl. Acad. Sci.* USA, 86:933, 1989.

[7] S.S. Kim, H. Utsunomiya, J.A Koski., B.M. Wu, M.J. Cima, J. Sohn, K. Mukai, L.G. Griffith, and J.P. Vacanti. Survival and function of hepatocytes on a novel three-dimensional synthetic biodegradable polymer scaffold with an intrinsic network of channels. *Ann Surg*, 228(1):8-13, 1998.

[8] K.F. Leong, C.M. Cheah, and C.K. Chua. Solid freeform fabrication of three-dimensional scaffolds for engineering replacement tissues and organs. *Biomaterials*, 24:2363–2378, 2003.

[9] H. Zhang, E. Burdet, A. N. Poo, and D. W. Hutmacher. Microassembly fabrication of tissue engineering scaffolds with customized design. *IEEE*

Transactions on Automation Science and Engineering, 5(3): 446-456, 2008.

[10] J. Alex, B. Vkramaditya, and B. J. Nelson. Teleoperated micromanipulation within a VRML environment using java. *Conference on intelligent Robots and systems* 1998

[11] M.B. Cohn, K.F. Bohringer, J.M. Noworolski, A. Singh, Ch.G. Keller, K.Y.Goldberg, and R.T. Howe. Microassembly technologies for MEMS. *Proceedings of SPIE - The International Society for Optical Engineering,* 515:2-16, 1998.

[12] G. Skidmore, M. Ellis, A. Geisberger, K. Tsui, R. Saini, T. Huang, and J. Randall.Parallel assembly of microsystems using Si micro electro mechanical systems. *Microelectronic Engineering,* 67-68: 445-452, 2003.

[13] H. Matsumura, M. Ishikawa, K. Kida, K. Maenaka, T. Kuno, K Nitta, M. Terano, and S. Minami. Development of micro-assembling technology for fabrication of large size liquid crystal displays. *Japanese Journal of Applied Physics, Part 1.Regular Papers and Short Notes and Review Papers,* 45(5 B): 4413-4418, 2006.

[14] W. Ehrfeld, M. Begemann, U. Berg, A. Lohf, F. Michel, and M. Nienhaus. Highly parallel mass fabrication and assembly of microdevices. *Microsystem Technologies,* 7(4): 145-50, 2001.

[15] K. F. Bohringer, R. S. Fearing, and K. Y. Goldberg. *The handbook of robotics,* 2nd edition, Shimon Nof, Wiley & Sons, 1998.

[16] Z. Ye, P. Han, C. Zhao, H. Wang, L. Wu,Y. Quan, X. Lu, and X. Hu. Micro-mould method for self-assembling three-dimensional opal photonic crystals *Journal of Physics D. Applied Physics,* 39(10): 2100-2104, 2006.

[17] K. Suzuki, H. Yamada, H. Miura, and H. Takanobu. Self-assembly of three dimensional micro mechanisms using thermal shrinkage of polyimide *ASMEISPS/JSME-IIP Joint conference on Micromechatronics for Information and Precision Equipment,* pages 1047-1053, 2006.

[18] B. R. Donald, C. G. Levey, and I. Paprotny. Planar microassembly by parallel actuation of MEMS microrobots. *Journal of Microelectro-mechanical Systems,* 17(4): 789-808, 2008.

[19] J. Zou, J. Chen, and C. Liu. Plastic deformation magnetic assembly (PDMA)

of 3D microstructures: technology development and application. *11th International Conference on Solid-State Sensors andActuators,* 2: 1582-1585, 2001.

[20] F. Arai, D. Ando, and T. Fukuda. Micro manipulation based on micro physics-strategy based on attractive force reduction and stress measurement. *Tnt. Conf on Intelligent Robots and Sys.,* 2:236-241, 1995.

[21] R.S. Fearing. Survey of sticking effects for micro parts handling. *Int. Conf on Intelligent Robots and Sys.,* 2:212-217, 1995.

[22] A.H. Slocum. *Precision Machine Design.* Prentice Hall, 1992.

[23] S. J. Ralis, B. Vikramaditya, and B. J. Nelson. Micropositioning of a weakly calibrated microassembly system using coarse-to-fine visual servoing strategies. *IEEE Transactions on Electronics Packaging Manufacturing,* 23(2): 123-13 1, 2000.

[24] G.Yang and B.J.Nelson. Automated microassembly in MEMS Packaging.ser.Electronics. *Materials Information Service (EMIS) Processing*, chapter 5, 2003.

[25] M. Tichem, D. Lang, and B. Karpuschewski. A classification scheme for quantitative analysis of micro-grip principles. *Assembly Automation,* 24(1): 88-93,2004.

[26] F.F.C. Duval, S. A. Wilson, G. Ensell, N.M.P Evanno, M. G. Cain, and R.W.Whatmore. Characterization of PZT thin film micro-actuators using a silicon micro-force sensor. *Sensors and Actuators, A: Physical*, 133(1): 35-44, 2007.

[27] I. Karjalainen, T. Sandelin, R. Heikkila, and R. Tuokko. Using piezoelectric technology to improve servo gripper performance in mini- and microassembly. *Assembly Automation,* 25(2): 117-123, 2005.

[28] T. Tanikawa, and T. Arai. Development of a micro-manipulation system having a two-fingered micro-hand. *IEEE Transactions on Robotics and Automation,* 15(1): 152-162, 1999.

[29] Y. Haddab, N. Chaillet, and A. Bourjault. A microgripper using smart piezoelectric actuators. *International Conference on Intelligent Robots and Systems*, 1: 659-64, 2000.

[30] R.R. Panepucci, and J.A. Martinez. Waveguide microgripper with optical feedback for microassembly. *17th Biennial University/Government/ Industry Micro/Nano Symposium,* pages 132-32, 2008.

[31] R.J. Chang, and C.C. Chen. Using microgripper for adhesive bonding in automatic microassembly system. *Proceedings of IEEE International Conference on Mechatronics and Automation,* pages 440-5, 2007.

[32] M. Goldfarb, and N. Celanovic. A flexure-based gripper for small-scale manipulation. *Robotica,* 17(2): 181-7, 1999.

[33] R. Perez, N. Chaillet, K. Domanski, P. Janus, and P. Grabiec. Fabrication, modeling and integration of a silicon technology force sensor in a piezoelectric micro-manipulator. *Sensors and Actuators, A: Physical,* 128(2): 3 67-375, 2006.

[34] M.C. Carrozza, A. Eisinberg, A. Menciassi, D. Campolo, S. Micera, and P. Dario.Towards a force-controlled microgripper for assembling biomedical microdevices. *Journal of Micromechanics and Microengineering,* 10(2): 271-276, 2000.

[35] M.C. Carrozza,. P. Dario, A. Menciassi, and A. Fenu. Manipulating biological and mechanical micro-objects using LIGA-microfabricated end-effectors. Proceedings. *IEEE International Conference on Robotics and Automation,* 2: 1811-1816, 1998.

[36] R.M. Voyles, and S. Hulst. Micro/macro force-servoed gripper for precision photonics assembly and analysis. *Robotica,* 23(4): 401-408, 2005.

[37] J.D. Grade, H. Jerman, and T.W. Kenny. Design of large deflection electrostatic actuators *Journal of Microelectromechanical Systems,* 12(3): 335-343, 2003.

[38] W. Ye, S. Mukherjee, and N.C. MacDonald. Optimal shape design of an electrostatic comb drive in microelectromechanical systems. *Journal of Microelectromechanical Systems,* 7(1): 16-26, 1998.

[39] B.E. Volland, H. Heerlein, and I.W. Rangelow. Electrostatically driven microgripper. *Microelectronic Engineering,* 61-62: 1015-1023, 2002.

[40] C.J. Kim, A.P. Pisano, and R.S. Muller. Silicon-processed overhanging microgripper. *Journal of Microelectromechanical Systems,* 1(1): 31-36,

1992.

[41] H. Zhang, E. Burdet, D.W. Hutmacher, A.N. Poo, Y. Bellouard, R. Clavel, and T. Sidler. Robotic micro-assembly of scaffold/cell constructs with a shape memory alloy gripper. *IEEE International Conference on Robotics and Automation,* 2:1483-1488, 2002.

[42] H. Zhang, Y. Bellouard, E. Burdet, R. Clavel, A.N. Poo, and D.W. Hutamacher. Shape memory alloy microgripper for robotic microassembly of tissue engineering scaffolds. *IEEE International Conference on Robotics andAutomation*, 5: 4918-4924, 2004.

[43] H. Zhang, Y. Bellouard, T. Sidler, E. Burdet, A.N. Poo, and R. Clavel. A monolithic shape memory alloy microgripper for 3-D assembly of tissue engineering. *Proceedings of The International Society for Optical Engineering*, 4568: 50-60, 2001.

[44] Y. Bellouard, T. Lehnert, J.E. Bidaux, T. Sidler, R. Clavel, and R. Gotthardt. Local annealing of complex mechanical devices: a new approach for developing monolithic micro-devices. *Materials Science & Engineering*, A273 -275: 795-798, 1999.

[45] K. Kuribayashi, and T. Fujii. A new micro SMA thin film actuator prestrained by polyimide. *International Symposium on Micromechatronics and Human Science,* pages 165-170, 1998.

[46] P. Krulevitch, A.P. Lee, P.B. Ramsey, J. Trevino, and M.A. Northrup. Thin film shape memory alloy microactuators. *Micro-Electro-Mechanical Systems (MEMS). 1996 International Mechanical Engineering Congress and Exposition* , pages 301- 306, 1996.

[47] D.O. Popa, H.K. Byoung, J.T. Wen, H.E. Stephanou, G. Skidmore, and A. Geisberger. Dynamic modeling and input shaping of thermal bimorph MEMS actuators. *IEEE International Conference on Robotics and Automation,* 1: 1470- 1475, 2003.

[48] P. Lerch, C.K. Slimane, B. Romanowicz, and P. Renaud. Modelization and characterization of asymmetrical thermal micro-actuators. *Journal of Micromechanics and Microengineering*, 6(1): 134-137, 1996.

[49] B.E. Volland, K. Ivanova, T. Ivanov, A. Badar, I.W. Rangelow, D.

Andrijasevic, F. Sumecz, S. Fischer, M. Spitzbart, W. Brenner, and I. Kostic. Thermally driven microgripper as a tool for micro assembly. *Microelectronic Engineering*, 83: 1393- 1395, 2006.

[50] A. Codourey, M. Rodriguez, and I. Pappas. A task-oriented teleoperation system for assembly in the microworld. *International Conference on Advanced Robotics. Proceedings*, pages 235-240, 1997.

[51] W. Zesch, M. Brunner, and A. Weber. Vacuum tool for handling micro-objects with a NanoRobot. *IEEE International Conference on Robotics and Automation*, 2: 1761-1766, 1997.

[52] X. Huang, X. Lv, and M. Wang. Development of a robotic microassembly system with multi-manipulator cooperation. *IEEE International Conference on Mechatronics and Automation*, pages 1197-1201, 2006.

[53] G. Yang, J.A. Gaines, and B.J. Nelson. A flexible experimental workcell for efficient and reliable wafer-level 3D microassembly. *IEEE International Conference on Robotics and Automation*, 1: 133-138, 2001.

[54] H.L. Woo, H.K. Byoung, S.O. Young, H. Stephanou, A.C. Sanderson, G. Skidmore, and M. Ellis. Micropeg manipulation with a compliant microgripper. *IEEE International Conference on Robotics and Automation*, 3: 3213-3218, 2003.

[55] S. Kota, J. Hetrick, Z. Li, and L. Saggere. Tailoring unconventional actuators using compliant transmissions: design methods and applications. *IEEE/ASME Transactions on Mechatronics*, 4(4): 396-408, 1999.

[56] S. Ballandras, S. Basrour, L. Robert, S. Megtert, P. Blind, M. Rouillay, P. Bernede, and W. Daniau. Microgrippers fabricated by the LIGA technique. *Sensors and Actuators*, 58(3): 265-272, 1997.

[57] H.K Byoung and J.T. Wen. Design of compliant MEMS grippers for micro-assembly tasks. *IEEE/RSJ International Conference on Intelligent Robots and Systems*, pages 760-775, 2006.

[58] D. Nikolai, L.C.William and K. M. James. Microassembly of 3-D micro-structures using a compliant, passive microgripper. *Journal of Micro-electromechanical systems*, 13(2): 176-189, 2004.

[59] Y. Lu, and C.J. Kim. Micro-finger articulation by pneumatic parylene balloons. *International Conference on Solid-State Sensors, Actuators and Microsystems,* 1: 276-279, 2003.

[60] J. Park, S, Kim, D.H. Kim, B. Kim, S. Kwon, J.O. Park, and K. Lee. Advanced controller design and implementation of a sensorized microgripper for micromanipulation. *IEEE International Conference on Robotics and Automation,* pages 5025-5032, 2004.

[61] C. Liu, and Y.W. Yi. Micromachined magnetic actuators using electroplated Permalloy. *IEEE Transactions on Magnetics,* 35(3): 1976-1985, 1999.

[62] A.M. Hoover, and R.S. Fearing. Rapidly prototyped orthotweezers for automated microassembly. *IEEE International Conference on Robotics and Auto- mation,* pages 812-819, 2007.

[63] B. Lopez-Walle, M. Gauthier, and N. Chaillet. Principle of a submerged freezegripper for microassembly. *IEEE Transactions on Robotics,* 24(4): 897-902, 2008.

[64] A.N. Das, P. Zhang, W.H Lee, D. Popa, and H. Stephanou. μ^3: Multiscale, deterministic micro-nano assembly system for construction of on-wafer microrobots. *IEEE International Conference on Robotics and Automation,* pages 461-466, 2007.

[65] E.D. Kunt, and K. Cakir, A. Sabanovic. A workstation for microassembly. *15th Mediterranean Conference on Control and Automation,* pages 1737-1742, 2007.

[66] H. Xie, W. Rong, L. Sun, and L. Chen. A flexible microassembly system for automated fabrication of MEMS sensors. *International Conference on Control,* p 4150061, 2006

[67] L. Chen, T. Chen, L. Sun, and W. Rong. Automatic microassembly system for die level fabrication of MEMS pressure sensor. *IEEE Conference on Industrial Electronics and Applications,* pages 1079-1083, 2007.

[68] M. Sun, J. Yu, G. Zong, S. Bi, and R. Liu A microscopic multi-view based workcell for wafer-level microassembling. *IEEE International Conference on Robotics and Biomimetics,* pages 1582-1587, 2006.

[69] H. Pongrac, A. Reiter, B. Faerber, and M.F. Zaeh. Evaluation ofjoystick sensitivity in telemanipulative microassembly. *IEEE International Workshop on Haptic Audio Visual Environments and Games,* pages 71-75, 2007.

[70] M.F. Zaeh, and A.Reiter. Precise positioning in a telepresent microassembly system. *IEEE International Workshop on Haptic Audio Visual Environments and Their Applications,* 2006.

[71] L. Bruzzone, and R.M. Molfino. A novel parallel robot for current microassembly applications. *Assembly Automation,* 26(4): 299-306, 2006.

[72] F. Schmoeckel, and H. Worn. Remotely controllable mobile microrobots acting as nano positioners and intelligent tweezers in scanning electron microscopes (SEMs). *IEEE International Conference on Robotics andAutomation,* 4: 3909-3913, 2001.

[73] S. Fatikow, J. Seyried, S. Fahlbusch, A. Buerkle, and F. Schmoeckel. A flexible microrobot-based microassembly station. *Journal of Intelligent and Robotic Systems: Theory and Applications,* 27: 135-69, 2000.

[74] H. Woern, J. Seyfried, S. Fahlbusch, A. Buerkle, and F. Schmoeckel. Flexible microrobots for micro assembly tasks. *Proceedings of the International Symposium on Micro Machine and Human Science,* pages 135-143, 2000.

[75] S. Fatikow, and U. Rembold. Automated microrobot-based desktop station for micro assembly and handling of microobjects. *IEEE Symposium on Emerging Technologies & Factory Automation,* 2: 586-592, 1996.

[76] A. Burkle, F. Schmoeckel, H. Worn, B.P. Amavasai, F. Caparrelli, and J.R. Travis. A versatile vision system for micromanipulation tasks. *EEE International Conference on Multisensor Fusion and Integration for Intelligent Systems,* pages 271-276, 2001.

[77] A. Eisinberg, A. Menciassi, P. Dario, J. Seyfried, R. Estana, and H. Woern. Eleoperated assembly of a micro-lens system by means of a micro-manipulation workstation. *Assembly Automation,* 27(2): 123-133, 2007.

[78] M.A. Greminger, and J.F. Jones. Real-time three-dimensional visualization of standard light microscope image sequences for

microassembly. *IEEE International Symposium on Assembly and Task Planning,* pages 194-199, 2005.

[79] J. Bert, S. Dernbele, and L.P. Nadine. Virtual camera synthesis for micro-manipulation and microassembly. *IEEE International Conference on Intelligent Robots and Systems,* pages 1390-1395, 2006.

[80] S.J. Lee, G.T. Park, K. Kim, D.H. Kim, and J.O. Park. Multiple vision based micro manipulation system for 3D-shaped micro parts assembly. *International Conference on Control, Automation and Systems,* pages 789-790, 2001.

[81] Y. Ge, J.A. Gaines, and B.J. Nelson. Optomechatronic design of micro-assembly systems for manufacturing hybrid Microsystems. *IEEE Transactions on Industrial Electronics,* 52(4): 1013-1023, 2005.

[82] K.Kaneko, H. Tokashiki, K. Tanie, and K. Komoriya. A development of experimental system for macro-micro teleoperation. *IEEE International Workshop on Robot and Human Communication*, pages 30-35, 1995.

[83] K. Tsui, A.A. Gersberger, M. Ellis, and G.D. Skimore. Micromachined end- effector and techniques for diected MEMS assembly. *Journal of Micromech. Microeng*. 14: 542-549, 2004.

[84] Y. Ansel, F. Schmitz, S. Kunz, H.P. Gruber, and G. Popovic. Development of tools for handling and assembling microcomponents. *Journal of Micromechanics and Microengineering,* 12(4): 430-437, 2002.

[85] S. Fatikow, J. Seyfried, S. Fahlbusch, A. Buerkle, and F. Schmoeckel. Flexible microrobot-based microassembly station. *IEEE Symposium on Emerging Technologies and Factory Automation,* 1: 397-406, 1999.

[86] A. Buerkle, and S. Fatikow. Laser measuring system for a flexible microrobotbased micromanipulation station. *IEEE International Conference on Intelligent Robots and Systems,* 1: 799-804, 2000.

[87] Y. Ge, J.A. Gaines, and B.J. Nelson. A supervisory wafer-level 3D microassembly system for hybrid MEMS fabrication. *Journal of Intelligent and Robotic Systems: Theory and Applications,* 37(1): 43-68, 2003.

[88] K.B. Yesin, and B.J. Nelson. A CAD model based tracking system for

visually guided microassembly. *Robotica,* 23(4): 409-418, 2005.

[89] N. Sarkar, D. Yan, E. Horne, H. Lu, M. Ellis, J.B. Lee, R. Mansour, A Nallani, and G. Skidmore. Microassembled tunable MEMS inductor. *IEEE International Conference on Micro Electro Mechanical Systems,* pages 183-186, 2005.

[90] D.H. Kim, B. Kim, and H.Kang. Development of a piezoelectric polymer-based sensorized microgripper for microassembly and micromanipulation. *Microsystem Technologies*, 10(4): 275-280, 2004.

[91] C.K.M. Fung, W.J. Li, I. Elhajj, and X. Ning. Internet-based remote sensing and manipulation in micro environment. *IEEE/ASME International Conference on Advanced Intelligent Mechatronics*, 2: 695-700, 2001.

[92] Y. Shen, X. Ning, W.C. King, and W.J. Li. Internet-based remote assembly of micro-electro-mechanical systems (MEMS). *Assembly Automation,* 24(3): 289- 296, 2004.

[93] M. Probst, C. Hurzeler, R. Borer, and B.J. Nelson. Virtual reality for micro- assembly. *Proceedings of SPIE - The International Society for Optical Engineering,* 2007.

[94] J. Cecil, D. Powell, and D. Vasquez. Assembly and manipulation of micro devices-a state of the art survey, *Robotics and computer-integrated manufacturing,* 23: 580- 588, 2007.

[95] C. Cassier, A. Ferreira, and S. Hirai. Combination of vision servoing techniques and VR-based simulation for semi-autonomous microassembly workstation. *IEEE International Conference on Robotics and Automation,* 2: 1501-1506, 2002.

[96] A. Ferreira, C. Cassier, and S. Hirai. Automatic microassembly system assisted by vision servoing and virtual reality. *IEEE/ASME Transactions on Mechatronics,* 9(2): 321-333, 2004.

[97] N. Gobinath, J. Cecil, and D. Powell. Micro devices assembly using virtual environments. *Journal of Intelligent Manufacturing,* 8(3): 361-369, 2007.

[98] J. Cecil, N. Gobinath, J.P. Deshmukh, and D. Vasquez. VIRAM: A Virtual Reality environment for the Assembly of Micro devices.

Proceedings of the ASME Design Engineering Technical Conference, 4: 671-682, 2004.

[99] J. Cecil, and N. Gobinath. Development of a virtual and physical work cell to assemble micro-devices. *International Conference on Flexible Automation and Intelligent Manufacturing,* 21: 431-441, 2005.

[100] Y.H. Anis, J.K. Mills, and W.L. Cleghorn. Visual measurement of MEMS microassembly forces using template matching. *Conference on International Robotics and Automation*, pages 275-280, 2006.

[101] J.F. Jones, D.M. Kozlowski, and J.C. Trinkle. Micro-scale force-fit insertion. *Journal of Micromechatronics,* 2: 185-200, 2004.

[102] R. Lu, L. Wang, J.K. Mills, and S. Dong. 3-D automatic microassembly by vision-based control. *IEEE/RSJ International Conference on Intelligent Robots and Systems*, pages 297-302, 2007.

[103] L. Wang, J.K. Mills, and W.L. Cleghorn. Automatic microassembly using visual servo control. *IEEE Transactions on Electronics Packaging Manufacturing,* 3 1(4): 3 16-325, 2008.

[104] Y.H. Anis, J.K .Mills, and W.L. Cleghorn. Visual-servoing of a six-degree-of-freedom robotic manipulator for automated microassembly task execution. *Journal of Microlithography, Microfabrication, and Microsystems,* 7(3): 33017- 33026, 2008.

[105] Y.H. Anis, J.K. Mills, and W.L. Cleghorn. Automated microassembly task execution using vision-based feedback control. *IEEE International Conference on Information Acquisition,* pages 476-48 1, 2007.

[106] N. Dechev, R. Lu, W. Liu, L.Cleghorn, and J.K. Mills. Development of a 6 degree of freedom robotic micromanipulator for use in 3D MEMS microassembly. *Conference on International Robotics and Automation,* page 281-288, 2006.

[107] H.K. Chu, J.K. Mills, and W.L. Cleghorn. MEMS capacitive force sensor for use in microassembly. *IEEE/A SME International Conference on Advanced Intelligent Mechatronics,* pages 797-802, 2008.

[108] L. Wang, R. Lu, J.K. Mills, and W.L. Cleghorn. Automatic 3D

joining in microassembly. *IEEE International Conference on Information Acquisition,* page 292-297, 2007.

[109] Y.H. Anis, J.K. Mills, and W.L. Cleghorn. Vision-based measurement of microassembly forces. *Journal of Micromechanics and Microengineering,* 16(8): 1639-1652, 2006.

[110] I.B. Bahadur, and J.K. Mills. Towards development of a one-port resonant sensor for robotic-based microassembly force measurement. *IEEE International Conference on Mechatronics and Automation,* pages 469-474, 2006.

[111] D. Popa, H.K Byoung, S. Jeongsik, and J. Zou. Reconfigurable micro-assembly system for photonics applications. *IEEE International Conference on Robotics and Automation,* 2: 1495-1500, 2002.

[112] B. Kim, H. Kang, D.H. Kim, G.T. Park, and J.O. Park. Flexible microassembly system based on hybrid manipulation scheme. *IEEE International Conference on Intelligent Robots and Systems,* 2: 2061-2066, 2003.

[113] K.B. Yesin, and B.J. Nelson. Robust CAD model based visual tracking for 3D microassembly using image space potentials. *IEEE International Conference on Robotics and Automation,* 2: 1868-1873, 2004.

[114] E.T. Enikov, L.L. Minkov, and S. Clark. Microassembly experiments with transparent electrostatic gripper under optical and vision-based control. *IEEE Transactions on Industrial Electronics,* 52(4): 1005-10 12, 2005.

[115] R. Schmitt, S. Driessen, and B. Engelmann. Controlling the assembly of micro systems by image processing. *Microsystem Technologies,* 12(7): 640-645, 2006.

[116] T. Baidyk, and E. Kussul. A neural classifier for handwritten digit recognition and visual controlled microassembly. *Neurocomputing,* 69: 2227-2235, 2006.

[117] T. Baidyk, E. Kussul, O. Makeyev, A. Caballero, L. Ruiz, G. Carrera, and G. Velasco. Flat image recognition in the process of microdevice assembly. *Pattern Recognition Letters,* 25(1): 107-118, 2004.

[118] J. Wang, A. Liu, X. Tao, and H. Cho. Microassembly of micropeg and -

hole using uncalibrated visual servoing method. *Precision Engineering,* 32(3): 173-18 1, 2008.

[119] Z. Lu, P.C.Y. Chen, and W. Lin. Force sensing and control in micro-manipulation. *IEEE Transactions on Systems, Man and Cybernetics,* 36(6): 7 13-724, 2006.

[120] A. Eisinberg, A. Menciassi, S. Micera, D. Campolo, M.C. Carrozza, and P. Dario. PI force control of a microgripper for assembling biomedical microdevices. *IEEE Proceedings: Circuits, Devices and Systems,* 148(6): 348-3 52, 2001.

[121] J. Park, S. Kim, D.H. Kim, B. Kim, S.J. Kwon, J.O. Park, and K.I. Lee. Identification and control of a sensorized microgripper for micromanipulation. *IEEE/ASME Transactions on Mechatronics,* 10(5): 601-606, 2005.

[122] J.A. Thompson, and R.S. Fearing. Automating microassembly with ortho-tweezers and force sensing. *IEEE/RSJ International Conference on Intelligent Robots and Systems,* 3: 1327-1334, 2001.

[123] A. Tafazzoli, C. Pawashe, and M. Sitti. Force-controlled microcontact printing using microassembled particle templates. *Conference on International Robotics and Automation,* page 263-268, 2006.

[124] Y. Shen, E. Winder, X. Ning, C.A. Pomeroy, and U.C. Wejinya. Closed-loop optimal control-enabled piezoelectric microforce sensors. *IEEE/ ASME Transactions on Mechatronics,* 11(4): 420-427, 2006.

[125] Y. Yin, C. Zhou, S. Chen, H. Hu, and Z. Lin. Optimal design of micro-force sensor for wire bonding with high acceleration and frequent movement. *Sensors and Actuators A (Physical),* 127(1): 104-118, 2006.

[126] U.C. Wejinya, Y. Shen, X. Ning, and F. Salem. Force measurement of embryonic system using in situ PVDF piezoelectric sensor. *Midwest Symposium on Circuits and Systems,* 1: 108-112, 2006.

[127] Z. Lu, P.C.Y. Chen, J. Nam, R. Ge, and W. Lin. A micromanipulation system with dynamic force-feedback for automatic batch microinjection. *Journal of Micromechanics and Microengineering,* 17(2): 314-321, 2007.

[128] H. Zhang, F. Chollet, E. Burdet, A.N. Poo, and D. W. Hutmacher. Fabrication of 3D micro-parts for the assembly of scaffold/cell constructs in tissue engineering. *ICMAT*, 2003.

[129] J. Laura, A. Suggs, and G. Mikos. Synthetic Biodegradable Polymers for Medical Applications. *Physical properties of polymers handbook*, Ed James E.Mark, American Institute of Physics Press, 1996.

[130] http://www.geocities.com/guerinlj/.

[131] http://memscyclopedia.org/su8.html.

[132] http://www.edmundoptics.com/US/.

[133] H. Zhang. *Robotic Microassembly of Tissue Engineering Scaffold*. National University of Singapore, 2004.

[134] J.A.J. Steen, J. Hayakawa, T. Harada, K. Lee, F. Calame, G. Boero, A.J. Kulik, and J. Brugger. Electrically conducting probes with full tungsten cantilever and tip for scanning probe applications. *Nanotechnology*, 17(5): 1464-1469, 2006.

[135] A.J. Melmed. The art and science and other aspects of making sharp tips. *Journal of Vacuum Science & Technology*, 9(2): 601-608, 1991.

[136] A.D. Davydov, A.P. Grigin, V.S. Shaldaev, and A.N. Malofeeva. Limiting current of Tungsten electrochemical dissolution under conditions of natural convection: Vertical plane electrode. *Journal of the Electrochemical Society,* 149(1): E6-E1 1, 2002.

[137] A.I. Oliva, G.A Romero. J.L. Pena, E. Anguiano, and M. Aguilar. Electrochemical preparation of tungsten tips for a scanning tunneling microscope. *Review of Scientific Instruments*, 67(5): 1917-1921, 1996.

[138] S. Kerfriden, A.H. Nahle, S.A. Campbell, F. C. Walsh, and J.R. Smith. Electrochemical etching of tungsten STM tips. *Electrochimica Acta*, 43: 1939- 1944, 1998.

[139] J. Park, and W. Moon. A hybrid-type micro-gripper with an integrated force sensor. *Microsystem Technologies*, 9(8): 511-519, 2003.

[140] F. Arai, , D. Andou, Y. Nonoda, T. Fukuda, H. Iwata, and K. Itoigawa. Integrated Microendeffector for Micromanipulation. *IEEE/ASME Transactions on Mechatronics*, 3(1): 17-23, 1998.

[141] Z. Lu, P.C.Y. Chen, A. Ganapathy, G. Zhao, J. Nam, G. Yang, E. Burdet, C.L. Teo, Q. Meng, and W. Lin. A forcefeedback control system for micro- assembly, *Journal of Micromechanics and Microengineering,* 16: 1861- 1868, 2006.

[142] N. Hogan and S.P. Buerger. Impedance and interaction control. *Robotics and Automation Handbook,* by Thomas R. Kurfess, CRC Press, Chapter 19, 2005.

[143] J. Stavnitzky, and D. Capson Multiple camera model-based 3-D visual servo. *IEEE Transactions on Robotics and Automation,* 16(6): 732-739, 2000.

[144] P. Corke. System issues in visual servo control. Proc. *IEEE int. Conf. Robotics and Automation,* 1996

[145] A.C. Sanderson, and L.E. Weiss. Image-based visual servo control using relational graph error signals. *Proceedings of the International Conference on Cybernetics and Society,* pages 1074-1077, 1980.

[146] S. Hutchinson, G.D. Hager, and P.I. Corke. A tutorial on visual servo control. *IEEE Transactions on Robotics and Automation,* 12(5): 65 1-670, 1996.

[147] W. Sun, and T.C. Chin. Vision based micromanipulation using features: a multiple view approach. *IEEE Conference on Robotics, Automation and Mechatronics,* 1:77 – 82, 2004.

[148] S. Allegro, C. Chanel, and J. Jacot. Autofocus for automated microassembly under a microscope. *IEEE International Conference on Image Processing,* 2: 677-680, 1996.

[149] R. Duda, and P.E. Hart. Use of the Hough transformation to detect lines and curves in pictures. *Commun. ACM* ,15(1): ll-15, 1972.

[150] H.K. Yuen, J. Princen, J. Illingworth, and J. Kittler. Comparative study of Hough Transform methods for circle finding. *Image and Vision Computing,* 8(1): 7 1-77, 1990.

[151] B. Bhanu. Automatic Target Recognition: State of the Art Survey. *IEEE Transactions on Aerospace and Electronic Systems,* 22(4), 364-379, 1986.

[152] B. Bhanu and T. Jones. Image Understanding Research for Automatic Target Recognition. *IEEE Aerospace and Electronics Systems Magazine,* 8(10), 1993.

[153] E. S. Wesley and H. Qi. *Machine Vision,* Cambridge University Press, 2004.

[154] L. Firestone. Comparison of Autofocus Methods for Automated Microscopy. *Cytometry*, 12: 195-206, 1991.

[155] T. Yeo. Autofocus for Tissue Microscopy. *Image and vision computing,* 11(10): 629-639, 1993.

[156] J. Brenner. An Automated Microscope for Cytologic Research – A preliminary evaluation. *Journal of Histochemistry and Cytochemistry,* 24(1): 100-111, 1976.

[157] http://sensorone.com/AE801_Spec.asp

[158] http://www.mark10.com/instruments/sensor/series-sjr.html

[159] G. Zhao, C. L. Teo, D. W. Hutmacher and E. Burdet. Force controlled, automatic microassembly of tissue engineering scaffolds. *Journal of Micromechanics and Microengineering,* 20(3): 035001-12, 2010

Appendix A

Acceleration and Velocity Limits

A.1 Acceleration Limit

The acceleration limit of the *Z* stage has to be set to avoid part falling off the gripper by inertia forces when gripper begin to moving up or stop to moving down. When withdrawing the gripper at an acceleration of *a* (Figure A.1), the force between the gripper and parts is

$$F = m(a+g), \tag{A.1}$$

where *m* is the mass of the part, which can be estimated as

$$m = V\rho \approx 500\times 500\times 200\times 10^{-18}\times 1200 = 6\times 10^{-10} m^3 . \tag{A.2}$$

The maximum acceleration of the stage is $3750000 \mathrm{con ts}/\mathrm{s}^2$, which is equal to $0.375 m/\mathrm{s}^2$, so the force between the gripper and micropart when withdraw gripper at the maximum acceleration is

$$F \approx 6\times 10^{-10}(0.375+9.8) = 6.105\times 10^{-9} N = 6.105\times 10^{-6} mN . \tag{A.3}$$

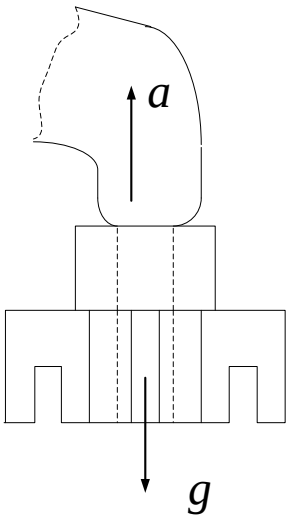

Figure A.1: Force analysis when gripper moving up with an accelerated velocity.

This value is orders of magnitude smaller than the friction (in the range of a few *mN*s to tens of *mN*s), so in the assembly process the mass of the part and inertia force it caused can be ignored totally.

A.2 Velocity Limit

During the picking up and assembly process, the host PC will read data from the force sensor via a ServoToGo card and based on the force information, command will be sent to the *Z* stages to realize admittance force control.

The maximum speed for the host PC to handle the information is 66.67*Hz*. That is 0.015 second for each command being calculated and sent out. If the velocity of the stage is too large, the stage will move a large distance before a new command coming. And the large distance may cause a large force overshot. To prevent damaging caused by the force overshot, the velocity has to be confined to a certain range.

Based on the experiment and experience, a force overshot of $50mN$ is acceptable, which corresponds to a deflection about $8\mu m$ at the tip end. So the maximum safe velocity of the stages when assemble or picking up part has to satisfy

$$V_{safe} \times 0.015 \le 8\mu m \ . \tag{A.4}$$

So we have

$$V_{safe} \le 8/0.015 = 533.36\mu m/s \ . \tag{A.5}$$

In the experiment, the velocity limit of the Z stage was set to $200\mu m$/s.